Title

Probing Quark-Gluon Plasma and Chiral Effects in Heavy-Ion Collisions: Measurements of Strangeness (Ω and ϕ) Production and Identified Particle Correlation in Au+Au Collisions at STAR/RHIC

Author

Wen, Liwen

Publication Date

2019

Peer reviewed|Thesis/dissertation

UNIVERSITY OF CALIFORNIA
Los Angeles

Probing Quark-Gluon Plasma and Chiral Effects in Heavy-Ion Collisions: Measurements of Strangeness (Ω and ϕ) Production and Identified Particle Correlation in Au+Au Collisions at STAR/RHIC

A dissertation submitted in partial satisfaction
of the requirements for the degree
Doctor of Philosophy in Physics

by

Liwen Wen

2019

ABSTRACT OF THE DISSERTATION

Probing Quark-Gluon Plasma and Chiral Effects in Heavy-Ion Collisions: Measurements of Strangeness (Ω and ϕ) Production and Identified Particle Correlation in Au+Au Collisions at STAR/RHIC

by

Liwen Wen
Doctor of Philosophy in Physics
University of California, Los Angeles, 2019
Professor Huan Z. Huang, Chair

Ultra-relativistic heavy-ion collision produces an extremely hot and dense medium of deconfined quarks and gluons, which is called Quark-Gluon Plasma (QGP). The STAR detector at Relativistic Heavy Ion Collider (RHIC) provides powerful experimental capabilities to probe the properties of this new form of matter, as well as novel quantum effects induced by the restoration of fundamental symmetry in qauntum-chromdynamics (QCD). Towards these goals, two research projects have been carried out at STAR/RHIC and will be presented in this thesis: 1) Measurement of mid-rapidity ($|y| < 0.5$) multi-strangenss particle (Ω and ϕ) production in Au+Au collisions at $\sqrt{s_{NN}} = 14.5$ GeV; 2) A systematic search for chiral effects using identified particle correlation.

Production mechanism for strange hadrons could be dramatically different in the presence of QGP compared to regular pp collisions. Thus strangeness signal is used extensively in Beam Energy Scan I (BES-I) program at RHIC to map out the phase diagram of QCD matter. As a part of BES-I, gold nuclei are collided at $\sqrt{s_{NN}} = 14.5$ GeV and the productions of mid-rapidity $\Omega(sss)$ and $\phi(\bar{s}s)$ are measured for the collisions. The ratio of anti-omega ($\bar{\Omega}$) over omega (Ω^-) is calculated and used to extract thermodynamics parameters (μ_B/T and μ_S/T) of collision system via statistical model. Additionally, the transverse momentum (p_T) dependence of nuclear modification factor (R_{cp}) is measured for ϕ meson and the result

shows similar feature to energies lower than 19.6 GeV. As a test of coalescence formation mechanism for strange hadrons, $N(\Omega^- + \bar{\Omega}^+)/2(N(\phi))$ as a function of p_T is studied and the data from central collision is found to deviate from model calculation and higher energy ($\sqrt{s_{NN}} > 19.6$ GeV) results in p_T range from $2.0 - 3.0$ GeV/c, which may imply a transition of created medium whose underlying dominant degrees of freedom change from quarks/gluons to hadrons as collision energy goes below 19.6 GeV. With excellent particle identification capability of STAR, a systematic search for the Chiral Magnetic Effect (CME) via measurements of γ_{112} correlation and κ_K parameter for identified particle pairs ($\pi\pi$, pK, πK, pp, $p\pi$) in Au+Au collisions has been conducted. The κ_K results are compared to expectations from the *A Multi-Phase Transport Model* (AMPT) simulations. Except $\pi\pi$ and pp correlations, the CME signals from other particle pairs are consistent with background model. κ_K from $\pi\pi$ shows higher values than background expectation, while the result for pp is even lower than the background, which requires further investigation. To search for Chiral Vortical Effect (CVE), a measurement of γ_{112} and δ correlations for Λp pairs in Au+Au collisions at $\sqrt{s_{NN}} = 27$ GeV was carried out and the results show that the CVE induced baryon number separation may exist in mid-central and mid-peripheral collisions with little contamination from flowing resonance decay background.

Future development of searches for the chirality effect in heavy ion collisions will also be discussed.

The dissertation of Liwen Wen is approved.

Micheal Gutperle

Kang L. Wang

Huan Z. Huang, Committee Chair

University of California, Los Angeles

2019

To my parents

TABLE OF CONTENTS

1 Introduction **1**

1.1 Motivations behind Heavy-ion Collisions 1

1.1.1 Space-time Evolution of Heavy-ion Collision 1

1.2 Experimental Signals of QGP 2

1.2.1 Jet-quenching 3

1.2.2 Elliptic Flow and Number of Constituent Quarks Scaling 6

1.2.3 Strangeness Enhancement 8

1.3 Beam Energy Scan at RHIC 9

1.4 Chiral Effects in High Energy Heavy Ion Collisions 10

1.4.1 QCD Vacuum and Axial Anomaly 10

1.4.2 Chiral Magnetic Effect (CME) 13

1.4.3 Chiral Vortical Effect (CVE) 14

2 STAR Experiment **18**

2.1 The Relativistic Heavy Ion Collider (RHIC) 18

2.2 The Solenoidal Tracker At RHIC (STAR) 19

2.2.1 The Time Projection Chamber (TPC) 23

2.2.2 The Time of Flight (TOF) Detector 24

3 Strange Particle Reconstruction **31**

3.1 Data 31

3.2 Centrality Bin Determination 31

3.3 $\Omega^{-}(\bar{\Omega}^{+})$ Baryon Reconstruction 37

3.3.1 Reconstruction Cuts 37

3.3.2 Signal Extraction . . . 39
3.3.3 Raw Transverse Momentum Spectra of $\Omega^-(\bar{\Omega}^+)$ . . . 43
3.3.4 Systematic uncertainty estimation . . . 46
3.4 ϕ Meson Reconstruction . . . 55
3.4.1 Reconstruction Cuts . . . 55
3.4.2 Mixed-Event Technique . . . 56
3.4.3 Signal Extraction . . . 57
3.4.4 Reconstruction Efficiencty and Raw Transverse Momentum Spectra of ϕ 57

4 Identified Particle Correlation . . . 64
4.1 Data Analysis Strategy . . . 64
4.1.1 Event Plane Orientation Estimation . . . 66
4.1.2 Event Plane Resolution . . . 68
4.1.3 Correlation Measurement . . . 70
4.1.4 Flow Normalized "γ_{112}", κ_{112} Correlator . . . 71
4.2 Data Set and Cuts . . . 73
4.2.1 Search for CME using Identified Particles . . . 73
4.2.2 Search for CVE using AuAu 27 GeV Collisions . . . 75

5 Results and Discussions . . . 78
5.1 $\Omega^-(\bar{\Omega}^+)$ Hyperon and ϕ meson production in AuAu 14.5 GeV Collisions . . . 78
5.1.1 Transverse Momentum Spectra and Mid-Rapidity Yields . . . 78
5.1.2 Antibaryon-Baryon ratio . . . 78
5.1.3 Nuclear Modification Factor R_{cp} . . . 82
5.1.4 Ω/ϕ Ratio . . . 84
5.2 Search for CME Using Identified Particle Correlation . . . 86

5.2.1 γ_{112} Correlation for $\pi\pi$, πp, pp, and pK Pairs 88
5.2.2 Comparison with the CME Background Model 90
5.3 Search for CVE using γ_{112} Correlation for Λp 92

6 Outlook:Towards Background-Free Measurements of Chiral Effects in Heavy-Ion Collisions 102
6.1 The Background Coupling to Reaction Plane: Elliptic Flow 102
6.1.1 Local Charge Conservation 102
6.1.2 Transverse Momentum Conservation 103
6.1.3 Particle Cluster Decay 104
6.2 Three Approaches to Disentangle Flow-related Background and the CME signal 104
6.2.1 Vary the Background: U+U collisions 104
6.2.2 Vary the Signal: Isobar Collisions 106
6.2.3 Event-shape Selection Analysis 109

A $\Omega^-(\bar{\Omega}^+)$ and ϕ yield data 117

References 123

LIST OF FIGURES

1.1 Heavy-ion collision evolution 2

1.2 Jet quenching at STAR 4

1.3 Jet quenching at PHENIX 5

1.4 v_2 for identified particles 6

1.5 NCQ scaling at RHIC 7

1.6 Strangeness Enhancement 8

1.7 QCD phase diagram 11

1.8 Energy (action) of the gluonic field as a function of winding number (taken from Ref. [Dia03]). Blue and red arrows represent instanton and sphaleron transitions (processes). 13

1.9 The CME illustration 15

1.10 The Wu experiment 16

1.11 The CVE illustration 17

2.1 RHIC Complex 20

2.2 Layout of the RHIC collider and locations of the four experiments 21

2.3 STAR sub-systems 22

2.4 TPC schematic diagram 24

2.5 TPC anode plane with one full sector 25

2.6 The energy loss ($\langle dE/dx \rangle$) for charged particles in the STAR TPC as a function of the momentum per charge 25

2.7 The location of the TOFp detectors 29

2.8 Two side views of the structure of an MRPC module 29

2.9 The PID performance of the first five final TOF trays 30

2.10 The total time resolution for the three-quarters installed STAR TOF system . . 30

3.1 xy Distribution of Events in Au+Au Collisions at $\sqrt{s_{NN}} = 14.5$ GeV 32

3.2 v_z Distribution of Events in Au+Au Collisions at $\sqrt{s_{NN}} = 14.5$ GeV 33

3.3 Glauber Monte Carlo event illustration 34

3.4 Correspondence between charged particle multiplicity and impact parameter . . 36

3.5 Reference multiplicity distribution in Au+Au collisions at $\sqrt{s_{NN}} = 14.5$ GeV . . 37

3.6 Distribution of centrality bins in Au+Au collisions at $\sqrt{s_{NN}} = 14.5$ GeV 38

3.7 Ω decay topology 40

3.8 Forward decay cut 41

3.9 $\sin\theta$ cut 41

3.10 Rotation background reconstruction illustration 44

3.11 Invariant mass distribution of reconstructed Ω^- in Au+Au $0-10\%$ central collisions at $\sqrt{s_{NN}} = 14.5$ GeV 48

3.12 Invariant mass distribution of reconstructed Ω^- in Au+Au $10-60\%$ central collisions at $\sqrt{s_{NN}} = 14.5$ GeV 49

3.13 Invariant mass distribution of reconstructed $\bar{\Omega}^+$ in Au+Au $0-10\%$ central collisions at $\sqrt{s_{NN}} = 14.5$ GeV 50

3.14 Invariant mass distribution of reconstructed $\bar{\Omega}^+$ in Au+Au $10-60\%$ central collisions at $\sqrt{s_{NN}} = 14.5$ GeV 51

3.15 Raw spectra for Ω^- 52

3.16 Raw spectra for $\bar{\Omega}+$ 52

3.17 Efficiency comparison for Ω^- in Au+Au collisions at $\sqrt{s_{NN}} = 14.5$ GeV 53

3.18 Efficiency for Ω^- in Au+Au collisions at $\sqrt{s_{NN}} = 14.5$ GeV 53

3.19 Efficiency comparison for $\bar{\Omega}^+$ in Au+Au collisions at $\sqrt{s_{NN}} = 14.5$ GeV 54

3.20 Efficiency for $\bar{\Omega}^+$ in Au+Au collisions at $\sqrt{s_{NN}} = 14.5$ GeV 54

3.21 Dip angle cut for ϕ meson reconstruction 56
3.22 Mixed event buffer 58
3.23 Invariant mass distribution of reconstructed ϕ mesons for $0-5\%$ central Au+Au collisions at $\sqrt{s_{NN}} = 14.5$ GeV 59
3.24 Invariant mass distribution of ϕ meson after background subtraction in central Au+Au collisions at $\sqrt{s_{NN}} = 14.5$ GeV 60
3.25 Efficiency error for ϕ mesons reconstruction 61
3.26 Reconstruction efficiency for ϕ mesons 62
3.27 Raw spectra of ϕ mesons in Au+Au collisions at $\sqrt{s_{NN}} = 14.5$ GeV 63

4.1 Preferential emission direction of pions in non-central Au+Au collisions 65
4.2 Event plane correction 68
4.3 Event plane resolution as a function of χ_m 69
4.4 γ_{112} analysis procedures 72
4.5 Advantages of H correlator 74
4.6 Invariant mass of $\Lambda(\bar{\Lambda})$ 76

5.1 Corrected spectra of Ω^- in Au+Au collisions at $\sqrt{s_{NN}} = 14.5$ GeV 79
5.2 Corrected spectra of $\bar{\Omega}^+$ in Au+Au collisions at $\sqrt{s_{NN}} = 14.5$ GeV 79
5.3 Corrected spectra of ϕ mesons in Au+Au collisions at $\sqrt{s_{NN}} = 14.5$ GeV 80
5.4 Energy dependence of ϕ meson yields in central heavy-ion collisions 81
5.5 Energy dependence of anti-baryon/baryon ratio at STAR 82
5.6 A test for thermal model 83
5.7 μ_B/T and μ_S/T extraction from thermal model 84
5.8 Energy dependence of μ_B/T and μ_S/T in the most central Au+Au collisions . . 85
5.9 p_T dependence of $R_{\rm cp}$ for ϕ mesons in Au+Au collisions 86

5.10 Transverse momentum dependence of $R_{\rm cp}$ for ϕ in Au+Au collisions at BES-I energies 87
5.11 Ω/ϕ ratio as a function of p_T in Au+Au collisions at BES-I energies 88
5.12 $\Delta\gamma_{112}$ for $\pi\pi$ correlation in Au+Au 200 GeV 89
5.13 $\Delta\gamma_{112}$ for $\pi\pi$ and hh correlation [A$^+$14b] in Au+Au 39 GeV collisions 90
5.14 $\Delta\gamma_{112}$ for πK pairs in Au+Au 200 and 39 GeV 91
5.15 $\Delta\gamma_{112}$ for $p\pi$ pairs in Au+Au 200 and 39 GeV 92
5.16 $\Delta\gamma_{112}$ for pp and pK correlation in Au+Au collisions at $\sqrt{s_{NN}} = 39$, 200 GeV . 93
5.17 Distribution of γ_{112} of mis-identified Λ daughters 93
5.18 Invariant mass spectrum of $p\pi^-$ pairs in γ_{112} 94
5.19 κ_K for charged hadron in Au+Au collisions at various energies 94
5.20 κ_K for $\pi\pi$ and hh in Au+Au collisions at 200 GeV 95
5.21 κ_K for $\pi\pi$ in Au+Au 39 GeV 96
5.22 κ_K for πK in Au+Au collisions at 39 and 200 GeV 97
5.23 κ_K for $p\pi$ in Au+Au collisions at 39 and 200 GeV 98
5.24 κ_K for pp and pK in Au+Au collisions at 200 GeV 99
5.25 $\Delta\gamma_{112}$ for Λp correlation in Au+Au 200 GeV 99
5.26 Hyperon polarization in Au+Au Collisions 100
5.27 $\Delta\gamma_{112}$ for Λp in Au+Au collisions at $\sqrt{s_{NN}} = 27$ GeV 101
5.28 $\Delta\delta$ for Λp in Au+Au collisions at $\sqrt{s_{NN}} = 27$ GeV at STAR. 101

6.1 Comparison between STAR measured γ_{112} and LCC induced signal 103
6.2 Uranium-Uranium collision geometry 105
6.3 $\Delta\gamma_{112}$ v.s. v_2 comparison between Au+Au and U+U collisions 106
6.4 The CME in UU collisions 107
6.5 Magnetic fields and eccentricities in Ru+Ru and Zr+Zr collisions 109

6.6 Magnitude and significance of the relative difference in the CME signal between Ru+Ru and Zr+Zr collisions 110

6.7 Centrality dependence of charge separation signal in Ru+Ru and Zr+Zr collisions 111

6.8 N_{part} dependence of elliptic flow of Ru+Ru and Zr+Zr in AMPT simulation . . 112

6.9 Search for the CME using event-shape engineering at ALICE 114

6.10 q^2 distribution and v_2 vs. q^2 115

6.11 AMPT simulation of q^2 dependence of $N_{\mathrm{part}} \times \gamma$ and $N_{\mathrm{part}}(\Delta\gamma)$ 116

LIST OF TABLES

2.1 RHIC Performance Specification 19

2.2 STAR TPC technical parameters 26

3.1 Minimal Bias Triggers 32

3.2 Event cuts for Au+Au 14.5 GeV 32

3.3 Npart for centrality bins in Au+Au 14.5 GeV at STAR 37

3.4 Ncoll for centrality bins in Au+Au 14.5 GeV at STAR 38

3.5 Reconstruction cuts for Ω 42

3.6 Reconstruction cuts for systematic uncertainties estimation 46

3.7 Reconstruction cuts combinations for ϕ mesons 47

3.8 Reconstruction cuts for ϕ meson. 55

4.1 Used Triggers in Run11 Au+Au Collisions at $\sqrt{s_{NN}} = 200$ GeV 74

4.2 Used Triggers in Run10 Au+Au Collisions at $\sqrt{s_{NN}} = 39$ GeV 75

4.3 Event Cuts in Analyses for Au+Au Collisions at $\sqrt{s_{NN}} = 39, 200$ GeV 75

4.4 Track Cuts in Analyses for Au+Au Collisions at $\sqrt{s_{NN}} = 39, 200$ GeV 75

4.5 Particle Identification Cuts in Analyses for Au+Au Collisions at $\sqrt{s_{NN}} = 39, 200$ GeV 76

4.6 $\Lambda(\bar{\Lambda})$ Reconstruction Cuts 77

A.1 Ω^- spectra in Au+Au collisions at $\sqrt{s_{\rm NN}}$ =14.5 GeV $(0-10\%)$ 117

A.2 Ω^- spectra in Au+Au collisions at $\sqrt{s_{\rm NN}}$ =14.5 GeV $(10-60\%)$ 117

A.3 $\bar{\Omega}^+$ spectra in Au+Au collisions at $\sqrt{s_{\rm NN}}$ =14.5 GeV $(0-10\%)$ 118

A.4 $\bar{\Omega}^+$ spectra in Au+Au collisions at $\sqrt{s_{\rm NN}}$ =14.5 GeV $(10-60\%)$ 118

A.5 ϕ spectra in Au+Au collisions at $\sqrt{s_{\rm NN}}$ =14.5 GeV $(0-10\%)$ 118

A.6 ϕ spectra in Au+Au collisions at $\sqrt{s_{\rm NN}}$ =14.5 GeV $(10-20\%)$ 119

A.7 ϕ spectra in Au+Au collisions at $\sqrt{s_{\rm NN}}$ =14.5 GeV $(20-30\%)$ 119

A.8 ϕ spectra in Au+Au collisions at $\sqrt{s_{\rm NN}}$ =14.5 GeV $(30-40\%)$ 120

A.9 ϕ spectra in Au+Au collisions at $\sqrt{s_{\rm NN}}$ =14.5 GeV $(40-60\%)$ 120

A.10 ϕ spectra in Au+Au collisions at $\sqrt{s_{\rm NN}}$ =14.5 GeV $(60-80\%)$ 121

A.11 Ω^- Yield in Au+Au 14.5 GeV ($|y| < 0.5$) 121

A.12 $\bar{\Omega}^+$ Yield in Au+Au 14.5 GeV ($|y| < 0.5$) 121

A.13 ϕ Yield in Au+Au 14.5 GeV ($|y| < 0.5$) 122

ACKNOWLEDGMENTS

I feel extremely privileged to spend six wonderful years studying physics under the guidance of Prof. Huang . Every time when I got stuck in my research, he is always there for insightful advice which just "magically" works in many ways. I am also very grateful for the academic freedom given by Prof. Huang, which allows me to explore the knowledge, the technologies, and future careers that truly interest me. In addition, his care and suggestions on my life make me feel warm and supported, especially in those hard times.

It has been a great pleasure to work with so many smart and nice people in the nuclear physics group at UCLA. In particular, I would like to say a big "Thank you!" to Dr. Gang Wang for his help throughout the years. We had countless conversations on physics, programming, politics, cultures, and almost anything else! Luckily, a few papers and research projects get fruited out of those seemingly casual discussions. Also, I am always impressed by his knowledge about the STAR experiment and the history and progress of the research field we are working in. His patience for my stupid, sometime recurring, questions really takes my understanding of some difficult concepts and ideas to the next level.

Although never directly working on any hardware project in my Ph.D. career, I absorbed a lot of knowledge about the detectors at STAR from Oleg and Stephen, which makes me understand my physics analysis more deeply. Thank you, Oleg and Stephen!

My gratitude also goes to our post-docs and other students. They are Neha Shah, Md Nasim, Feng Zhao, Yuxi Pan, Roli Esha, Maria Sergeeva, and Krystal Alfonso. Without them, this journey would be undoubtedly more difficult. Meanwhile, I am grateful to Prof. Nu Xu, Prof. Bill Llope, Prof. Xianglei Zhu, and Prof. Jinhui Chen for all of the useful and enlightening discussions.

And finally, I can't find enough words to express my thankfulness to my dear parents for their unconditional love and support. Their optimism and resilience are always my encouragement along the way and of course none of my achievements, if any, would be possible without them.

VITA

2005–2008	Wenzhou Middle School, Wenzhou, Zhejiang, P. R. China.
2012	B.S. in Physics, University of Science and Technology of China, Hefei, Anhui, P. R. China.
2013	M.S. in Physics, UCLA.
2013–2017	Teaching Assistant, Department of Physics and Astronomy, UCLA
Jun.2018-Aug. 2018	Quantitative Developer Intern, Tower Research Capital, New York
2013–2018	Graduate Research Assistant, Department of Physics and Astronomy, UCLA.

PUBLICATIONS

Probing parton dynamics of QCD matter with Ω and ϕ production, L. Adamczyk *et al.* [STAR Collaboration], Phys. Rev. C **93**, no. 2, 021903 (2016)

Systematic Searches for the Chiral Magnetic Effect and the Chiral Vortical Effect Using Identified Particles at RHIC/STAR, L. Wen (for the STAR Collaboration), J. Phys. Conf. Ser. **779**, no. 1, 012067 (2017).

Towards Measurements of Chiral Effects Using Identified Particles from STAR, L. Wen (for the STAR Collaboration), Nucl. Phys. A **967**, 756 (2017).

Experimental Results on Chiral Magnetic and Vortical Effects, G. Wang, L. Wen,, Adv. High Energy Phys. **2017**, 9240170 (2017)

Event-Shape-Engineering Study of Charge Separation in Heavy-ion Collisions, F. Wen, J. Bryon, L. Wen, G. Wang, Chin. Phys. C **42**, no. 1, 014001 (2018)

Searches for Chiral Effects and Prospects for Isobaric Collisions at STAR/RHIC, L. Wen (for the STAR Collaboration), PoS CPOD **2017**, 007 (2018).

On the Clustering Properties of Mini-Jet and Mini-Dijet in High-Energy pp Collisions, C. Y. Wong, L. Wen, G. Wang and H. Zhong Huang, arXiv:1801.00759 [hep-ph].

CHAPTER 1

Introduction

1.1 Motivations behind Heavy-ion Collisions

Relativistic heavy-ion collisions was initially proposed to distribute high energy or high nuclear matter over a relatively large volume and finally to create a new form of matter with partonic degrees of freedom, Quark-Gluon Plasma (QGP) [McL06]. With QGP created in laboratory, windows are open to explore and understand the properties of the extremely hot and dense matter that QCD governs, and hopefully careful examination of this new matter form can lead us to not only the answer to the puzzling problems about quark confinement, but also insights into the workings of QCD, as well as discoveries of fundamentally new phenomena.

1.1.1 Space-time Evolution of Heavy-ion Collision

Before jumping into detailed analysis, it is helpful to qualitatively break down the evolution of a typical heavy-ion collision so that we can have a concrete big picture in mind as discussion goes deeper. As seen from Figure 1.1a, in a head-on heavy-ion collision both colliding nuclei are extremely thin disc (with diameter ~ 14 fm for Au or Pb) due to Lorentz contraction. Later, when two discs overlap or collide into each, a complex system with very high energy density will be created. Rough estimation shows when 1 fm/c after the collision, the energy density of the created system from $\sqrt{s_{NN}} = 200$ GeV Au+Au collisions at the Relativistic Heavy Ion Collider is around 10 GeV/fm^3, which is far larger than the typical energy density of a hadron that is 500 MeV/fm^3. Similar results (~ 12GeV/fm^3) can also be obtained for Pb+Pb collisions at $\sqrt{s_{NN}} = 2.76$ TeV at the Large Hadron Collider.

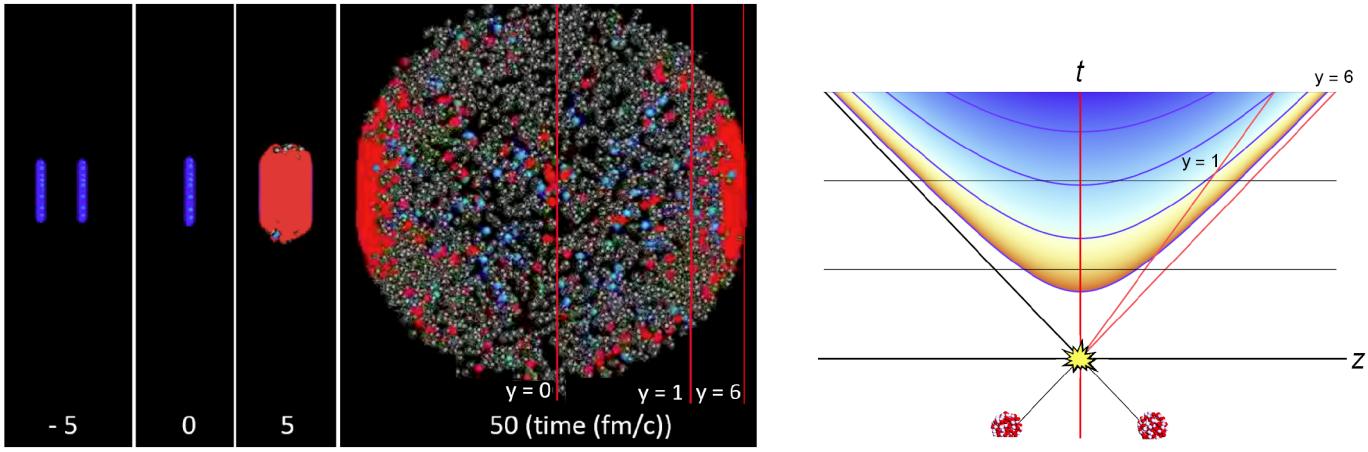

(a) (b)

Figure 1.1: (Taken from Ref. [YJLB] and Ref. [vdS14])(a) An A+A central collisions at different stages (from 5 fm/c before the collision to 50 fm/c after the collision). Blue and grey balls are hadrons and red area is QGP, which is created later at high rapidity. (b) Space-time evolution of a heavy-ion collisions. Color (orange to blue) marks the temperature (high to low) of the plasma. Evolution of the plasma is a function of proper time labeled by blue lines.

Therefore, hadrons are not existing anymore at this stage and a hot medium of quarks and gluons, named QGP, will be formed instead. After the production, QGP flows and expands hydrodynamically [HS13] [RR17] and finally hadrons are formed and fly away freely as the temperature cools down. Fig. 1.1b summarizes the space-time evolution of a HIC in a concise way. It can be observed that after collision, the medium evolves from hot (orange) to cold (blue), as a function of proper time (blue curves) and due to time dilation, QGP, which corresponds to the red space volume in Figure 1.1a, will be created later as rapidity goes up.

1.2 Experimental Signals of QGP

To experimentally detect the high energy density state of matter that is expected to be created in heavy-ion collisions, a wide range of experimental probes have been proposed and

examined during the past few decades on experiments at RHIC/LHC. A few typical and relevant examples will be listed below and of course the list is not comprehensive by any means.

1.2.1 Jet-quenching

In high energy proton-proton (pp) collisions, a struck quark after parton-parton hard-scatterings will fragment into a narrowly collimated "spray" of hadrons, which is called jet. Though this kind of hard-scattering processes also takes place in heavy-ion collisions, yet the scattered quarks will fly through a dramatically different environment, i.e., the newly formed hot and dense medium, before fragmentation. Thus, slowing-down or quenching jets that are emerging from those quarks are expected to be observed if QGP is truly created during the collision. Usually, nuclear modification factor, R_{AB}, is used to detect this effect in nucleus-nucleus collisions and its definition is as below:

$$R_{AB}(p_T) = \frac{d^2N/dp_t d\eta}{T_{AB} d^2\sigma^{pp}/dp_T d\eta} \tag{1.1}$$

where $d^2N/dp_T d\eta$ represents the differential yield per event in the $A+B$ collision, $T_{AB} = \langle N_{\rm bin} \rangle / \sigma^{pp}_{inel}$ describes the nuclear geometry, and $d^2\sigma^{pp}/dp_T d\eta$ is the $p+p$ inelastic cross section. Basically, this quantity is the ratio of scaled yield of measured particle in $A+B$ collisions over the yield in pp collisions at the same transverse momenta. If there is no medium effect, it should be unity.

The STAR and PHENIX experiments at RHIC both measured R_{AB} in Au+Au and $d+$Au (deuteron-gold) collisions at $\sqrt{s_{NN}} = 200$ GeV. The results from both experiments (see Figure 1.3 and Figure 1.2) show for charged hadrons with $2 < p_T < 7$ GeV/c, the production is largely suppressed in Au+Au collisions, while the pattern is missing in $d+$Au collisions. This sharp contrast strongly suggests the creation of dense medium in Au+Au collisions, while alternative interpretations, e.g., gluon saturation, are less favored given the absence of suppression in $d+$Au collisions.

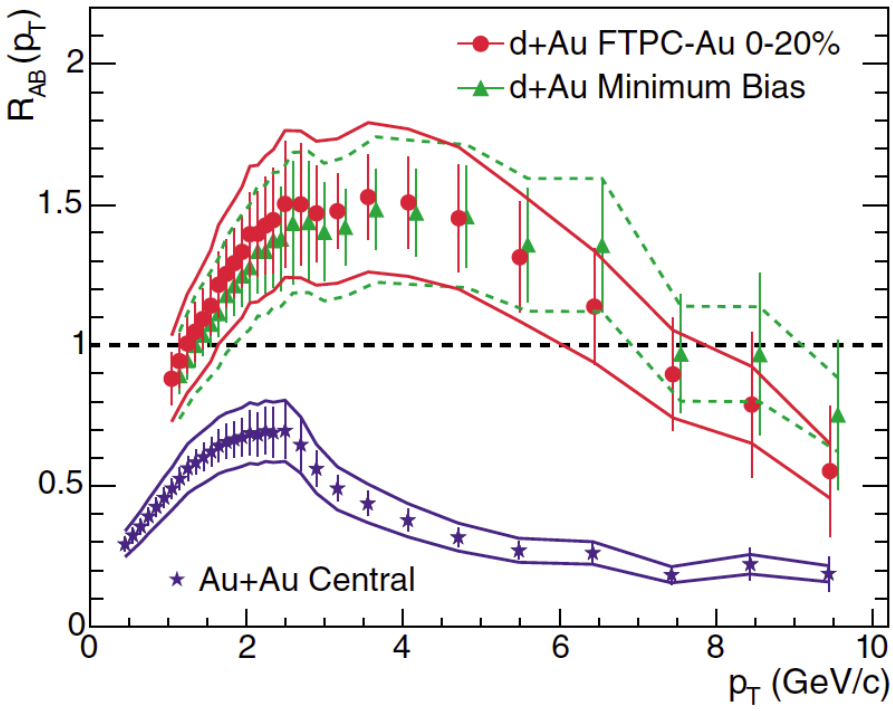

Figure 1.2: Comparison of $R_{AA}(R_{dA})$ for minimum bias central d+Au collisions and central Au+Au collisions. Taken from Ref. [A$^+$03b]

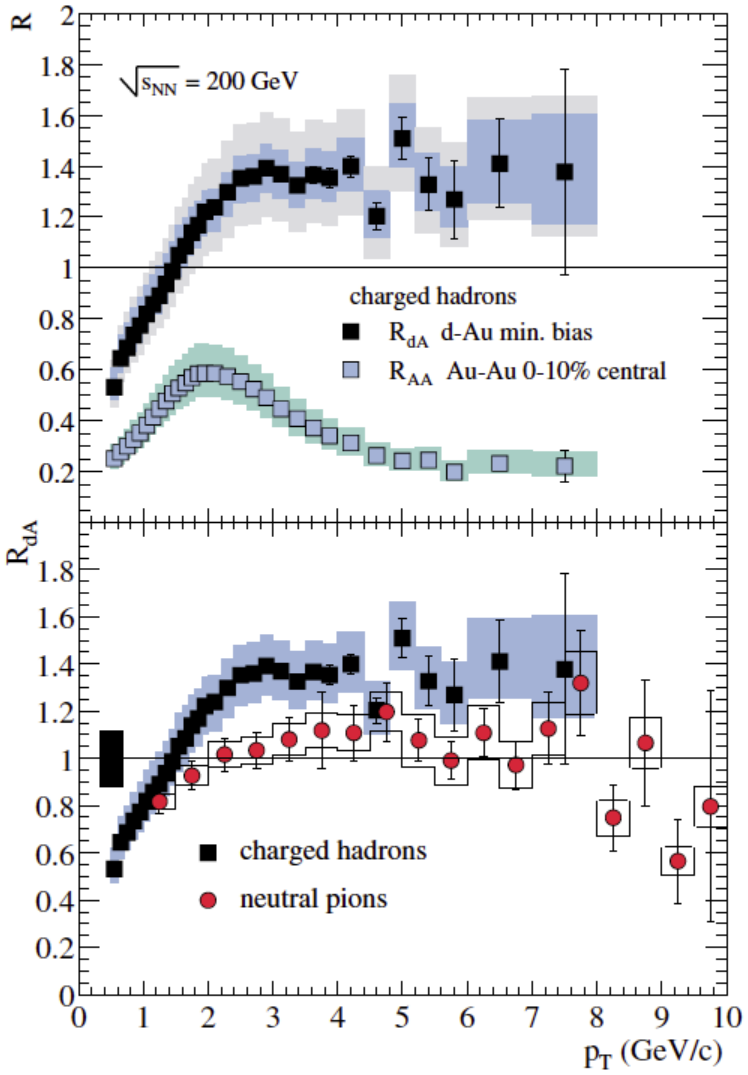

Figure 1.3: Top: Comparison of R_{dA} for $(h^+ + h^-)/2$ in minimum bias d+Au and R_{AA} in the most 10% central Au+Au collisions. Bottom: R_{dA} for $(h^+ + h^-)/2$ and neutral pions in d+Au collisions. Taken from Ref. [A$^+$03c]

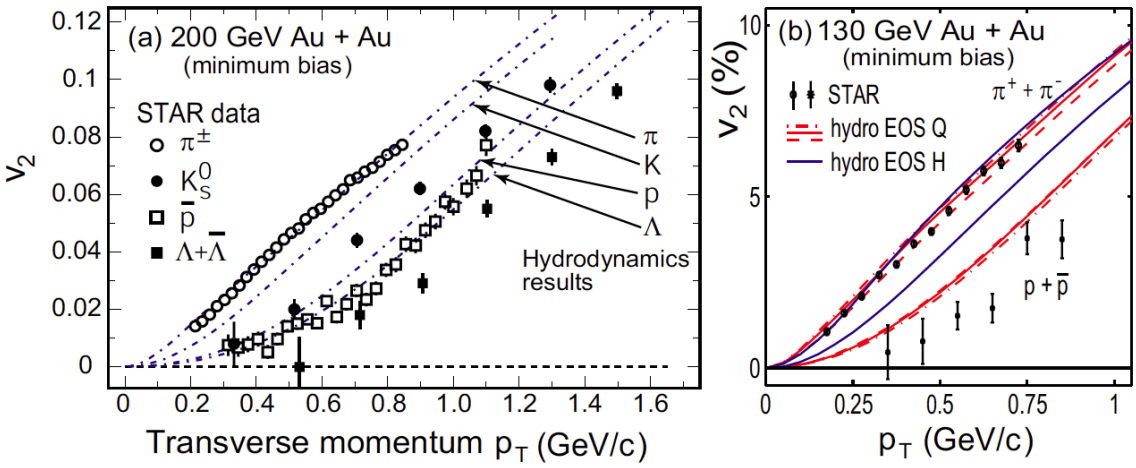

Figure 1.4: STAR results of the transverse momentum dependence of v_2 for identified particles in Au+Au collisions at 200 GeV and 130 GeV. Hydrodynamics calculations are also shown with lines for comparison. Taken from Ref. [A+05b].

1.2.2 Elliptic Flow and Number of Constituent Quarks Scaling

The anisotropy of particle yield w.r.t event plane is believed to be carrying information from early collision dynamics [Oll92] [Sor99] and can be described by the harmonic coefficients from its Fourier decomposition of the azimuthal angle distribution. The second order harmonic coefficient, also referred to as the elliptic flow or v_2, is expected to be the most pronounced. In Figure 1.4, the experimental results of elliptic flow for identified particles in Au+Au collisions at 200 GeV and 130 GeV are shown, along with the hydrodynamics calculations. The great agreement between experimental results and hydrodynamics calculations with assumption of ideal relativistic fluid flow at relatively low p_T range is a strong argument for the QGP claims. On the right panel, the calculation using equation of state (EOS) for QGP (marked by "EOS Q") and assuming early thermalization matches data very well, but if the expanding matter is a pure hadron gas (marked by "EOS H"), the mass dependence of v_2 is significantly under-predicted. This contrast suggests a strongly interacting matter created in early stage after collision is essentially a droplet of "perfect liquid" with small viscosity over entropy ratio.

At intermediate transverse momenta, hadron elliptic flow shows a clear and intriguing

dependence on the number of constituent quarks (NCQ) in the hadron (3 for baryons, 2 for mesons), as depicted in the upper panels of Figure 1.5 [A$^+$05b]. If both of p_T and v_2 are divided by NCQ, the discrepancy between baryons and mesons are gone, which supports the picture that hadrons are formed via coalescence of constituent quarks. This coalescence interpretation leads to a conclusion that is essential for the QGP discovery: hadronization takes place via an intermediate constituent quark stage, in other words, quarks have to be de-confiend before getting recombined into hadrons.

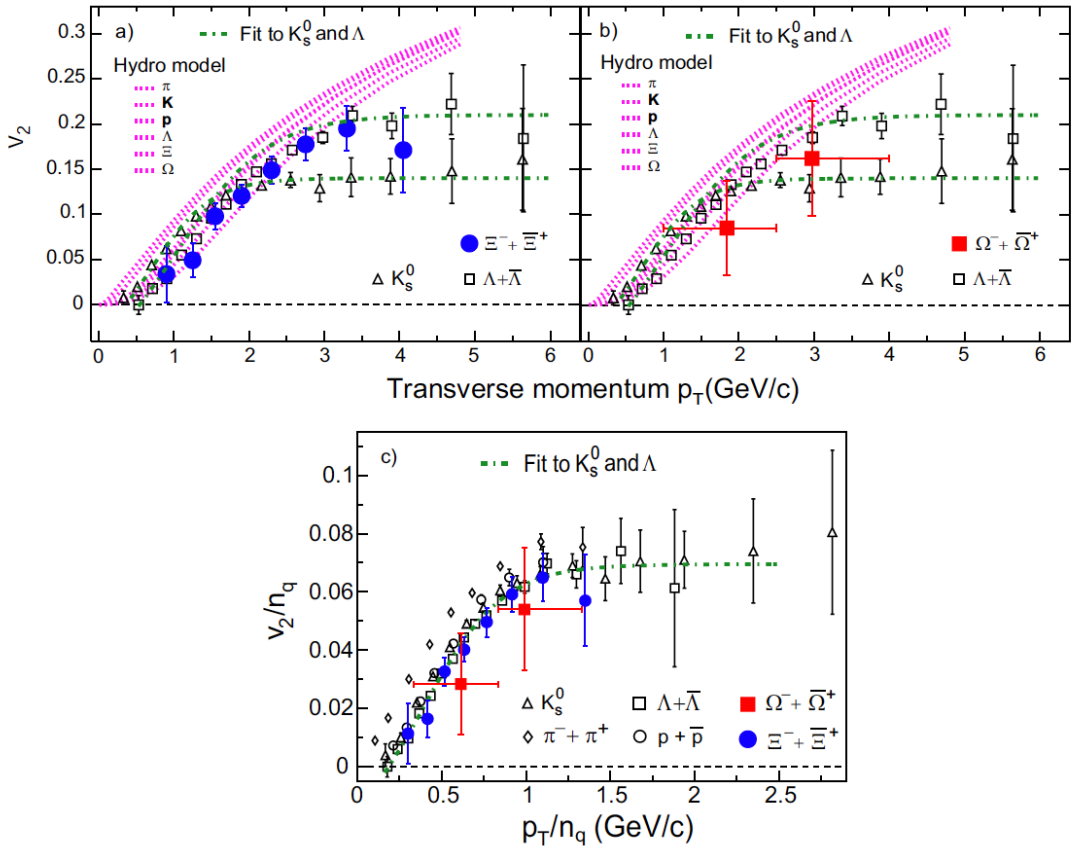

Figure 1.5: Transverse momentum dependence of elliptic flow for various particle species in Au+Au 200 GeV collisions at RHIC. K^0_S, Ξ, Ω, and $\Lambda + \bar{\Lambda}$ results are from STAR. PHENIX results for π and $p + \bar{p}$ are shown in bottom panel. Top: Elliptic flow, as a function of p_T for baryons and mesons. The dotted purple lines indicate the hydrodynamic calculations. Bottom: Number of constituent quarks scaled p_T dependence of elliptic flow for various particle specieies.

1.2.3 Strangeness Enhancement

It has been argued that enhanced strangeness particles yield could signal the formation of QGP in heavy-ion collisions. That is because compared to hadronic system, the production of strangeness via gluon fusion is more efficient due to the high gluon density and low energy threshold for strange and anti-strange quark pair production in QGP.

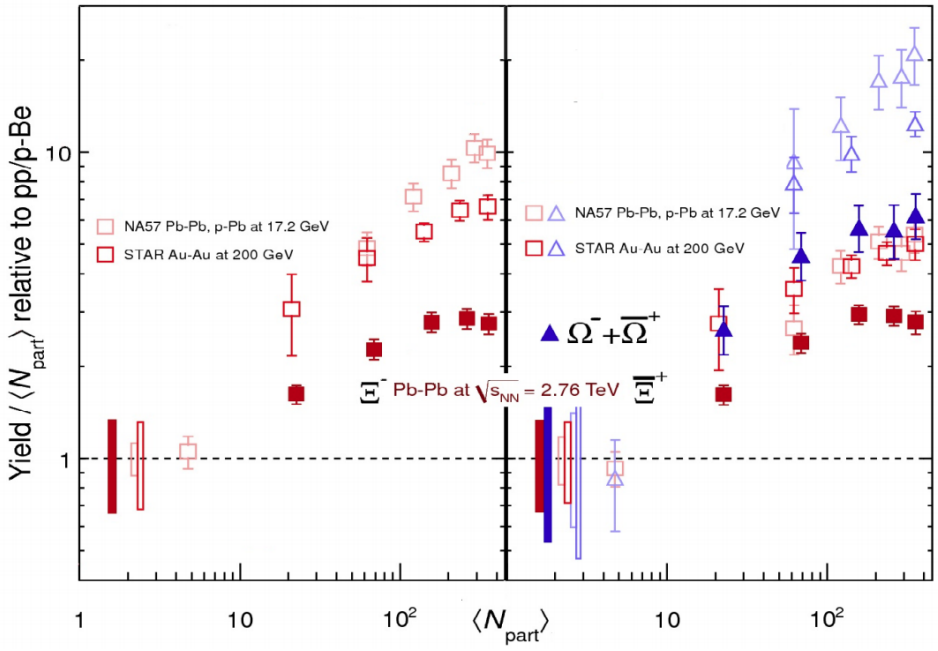

Figure 1.6: Number of participants (N_{part}) dependence of hyperon (left) and antihyperon (right) yields from ALICE, STAR and NA57.

From the summary plot in Figure 1.6 [A$^+$14a], we can observe significant enhancement for all multi-strange particles in heavy-ion collisions compared to p-Be collisions at RHIC and LHC. They are all larger than unity and these results are consistent with the picture of enhanced strangeness production in partonic matter under extreme conditions of high temperature and density. Especially for anti-hyperon production, the medium effect induced enhancement can reach as high as 20 in Pb+Pb collisions at 17.2 GeV (equivalently 158 A GeV), which is hardly seen in other measurements.

The three examples mentioned above is not aimed to cover the entire spectrum of powerful probes to detect QGP. The measurements of other physical observables such as ρ-meson

melting, J/Ψ suppression and so on also provide a consistent picture that a new form of matter—hot, dense and thermalized medium of de-confined quarks and gluons—is created in high energy Au+Au and Pb+Pb collisions at RHIC and LHC, respectively.

1.3 Beam Energy Scan at RHIC

In condensed matter physics, mapping out the full phase diagram is considered a crucial step towards a deep understanding of the properties of any complex material, this is also the case for the study of QCD matter. Given the convincing evidence of QGP created at RHIC and LHC, relativistic heavy-ion collision is proven a great "laboratory" to explore the rich structure in the phase diagram of hot and thermalized QCD matter. Temperature T and baryon number chemical potential μ_B (to quantify the excess of quarks over antiquarks density) are used to parameterize the QCD matter as shown in Figure 1.7. From the same figure, we can see in Au+Au collisions at top energy at RHIC or Pb+Pb collisions at LHC, μ_B is close to zero and hadron gas are formed from QGP via smooth cross-over. However, by lowering the collision energy, more significant baryon chemical potential range can be reached and therefore more parameter space on the phase diagram becomes accessible experimentally. Taking this avenue, the phase I of Beam Energy Scan (BES) program at RHIC has been carried out to collide gold-gold nuclei at 7.7, 11.6, 14.5, 19.6, 27, and 39 GeV from 2010 to 2014 and the second phase is planed for 2019 to 2020. The major scientific goal of BES program is to search for three features on QCD phase diagram: 1. critical point; 2. first-order phase transition; 3. "turn-off" of QGP.

It has been predicted that the extremely long wavelength fluctuations in the susceptibilities of baryon number, electric charge, and strangeness could be sensitive probes for the critical point [C$^+$09]. By scanning the collision energies, non-monotonic behavior in fluctuation measurements is expected. Allowed for a sensitive search for the critical point than the previous data with the fixed target experiments, the BES measurements are believed to bring improved results compared to the previous attempts at SPS.

At lower energies, the evolution path of created quark matter could possibly cross the

first-order transition boundary (white line on Figure 1.7). Hydrodynamic and transport models predict dv_1/dy (v_1 is the first harmonic coefficient of Fourier decomposition of particle azimuthal anisotropy w.r.t. event plane, also called "directed flow") goes to negative, which is considered as a prominent signature of possible first-order phase transition between hardonic matter and QGP [BSD$^+$00] [Sto05] [CR99]. STAR has been able to observe such a phenomenon in its analysis of the BES-I data.

As energies decreases, the energy density after collision drops below the threshold to create QGP. Thus the turn-off of QGP signals is expected to be observed in experimental data. The measurement of strangeness particle production in $\sqrt{s_{NN}} = 14.5$ GeV Au+Au colisions, which is the first part of this thesis work, is closely related to this pursuit of BES-I program.

1.4 Chiral Effects in High Energy Heavy Ion Collisions

This section presents a short introduction to the theoretical background of the experimental endeavor carried out by this thesis work to search for two intriguing quantum effects in high energy heavy ion collisions at STAR/RHIC: the Chiral Magnetic Effect (CME) and the Chiral Vortical Effect (CVE).

1.4.1 QCD Vacuum and Axial Anomaly

In order to minimize the energy density of the classical vacuum of QCD, the possible gauge fields is required to be pure gauges, which implies $A_i(\mathbf{x}) = \frac{i}{g}U(\mathbf{x})\partial_\mu U^\dagger$ in the temporal gauge ($A_0 = 0$). The different vacua corresponding to these possible gauges can be characterized by a topological invariant, the "winding number" n_W that is given by [KMW08]:

$$n_W = \frac{1}{24}\int d^3x\epsilon^{ijk}tr[(U^\dagger\partial_i U)(U^\dagger\partial_j U)(U^\dagger\partial_k U)] \in \mathbb{Z} \tag{1.2}$$

where $U(\mathbf{x})$ is an element of the gauge group SU(3). One can show if a gauge field configuration becomes a pure gauge at infinity, a transition between vacua can induce nonzero

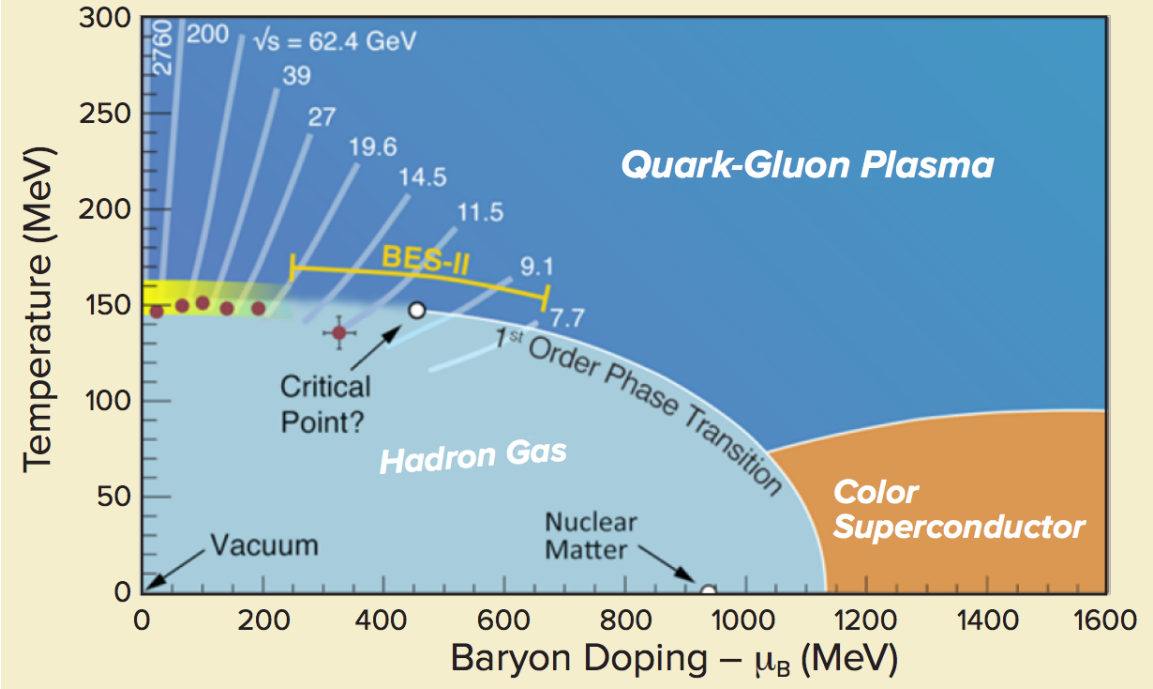

Figure 1.7: QCD phase diagram (taken from Ref. [A+15b]) parameterized by temperature and baryon chemical potential (μ_B). Lattice QCD calculations show near $\mu_B = 0$, phase transition from QGP to hadron gas is via continuous crossover. The Beam Energy Scan I (BES-I) program at RHIC (7.7-39 GeV, marked by white number) is to look for the critical point, the first-order phase transition, and turn-off of QGP. The BES-II is dedicated to search for the location of critical point. It is predicted that a color superconductor will be formed with higher μ_B and lower energy that can be found at the center of neutron star.

topological charge $Q_W \in \mathbb{Z}$:

$$Q_W = n_W(t = \infty) - n_W(t = -\infty) \tag{1.3}$$

It is found the instanton solution (tunneling event between vacua with different winding numbers) to the Euclidean Yang-Mills equation contributes significantly to this transition at zero temperature. More precisely, 't Hooft shows [tH76b] [tH76a] in the absence of fermions in QCD, the transition rate (between vacua different by unit of winding number) per unit volume is:

$$\frac{dN_t^{\pm}}{d^3x dt d\rho} = 0.0015(\frac{2\pi}{\alpha_S})^6 \exp(-\frac{2\pi}{\alpha_S})\frac{1}{\rho^5} \tag{1.4}$$

where ρ is the size of an instanton and $\alpha_S = g^2(\rho)/(4\pi)$ is the renormalization coupling constant. However, as the temperature rises, the transition rate due to instanton drops. A specific computation regarding the transition rate at finite temperature can be found in Ref. [PY80].

When the temperature rises higher, the instanton-driven transition becomes extremely difficult. However, there exists another class of QCD field configurations called "spharelons", which correspond to the peaks in Figure 1.8. The energy of the sphaleron configuration can be regarded as the height of the potential barrier between two vacuum states with different winding numbers. Therefore, if the temperature is high enough to overcome this energy barrier, the rate of transition between vacuum states of integer winding number due to sphalerons can increase dramatically. One such estimate (for SU(2) Yang-Mills theory, see Ref. [BMR00] [MHM98]) is:

$$\frac{dN_t^{\pm}}{dx^3 dt} \sim 25.4\alpha_W^5 T^4 \tag{1.5}$$

Given the non-zero transition rate between different vacuua and the topological charge induced in the process, the axial (chiral) anomaly can be "activated" in the presence of fermionic fields. The non-conserved axial (chiral) currents can be observed from the axial Ward-identity:

$$\partial^\mu j_\mu^5 = 2\sum_f m_f \left\langle \hat{\psi}_f i\gamma_5 \psi_f \right\rangle_A - \frac{N_f g^2}{16\pi^2} F_{\mu v}^a \tilde{F}_a^{\mu v} \tag{1.6}$$

here N_f represents the number of quark flavors, ψ_f is the quark field, and m_f is the mass of a quark. In the chiral limit ($m_f = 0$), the integration of Eq. 1.6 gives:

$$\Delta Q_5 = -2N_f\left(\frac{g^2}{32\pi^2}\int d^4x F_{\mu v}^a \tilde{F}_a^{\mu v}\right) \tag{1.7}$$

It is known that all field configurations with finite action can be characterized by the topological charge that is given by:

$$Q_W = \frac{g^2}{32\pi^2}\int d^4x F_{\mu v}^a \tilde{F}_a^{\mu v} \quad . \tag{1.8}$$

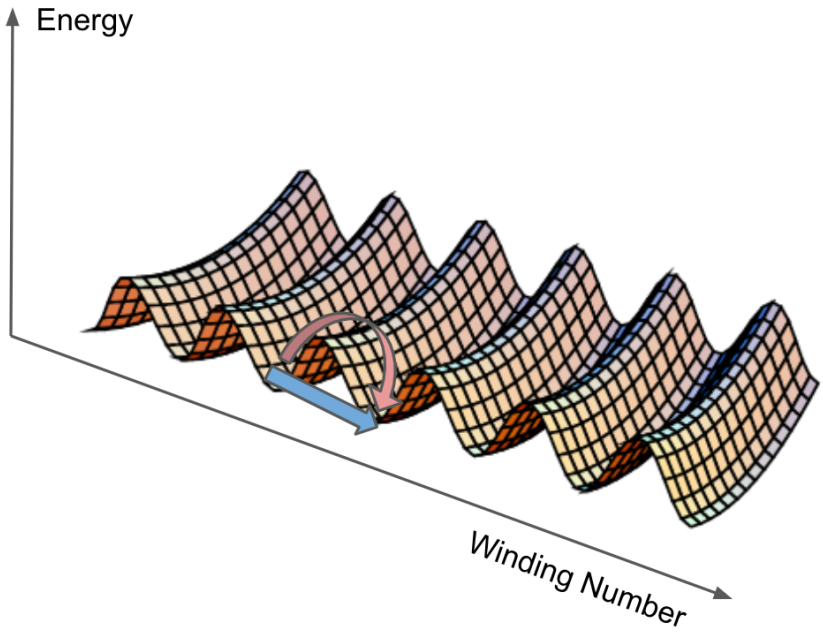

Figure 1.8: Energy (action) of the gluonic field as a function of winding number (taken from Ref. [Dia03]). Blue and red arrows represent instanton and sphaleron transitions (processes).

If we assume, at $t = -\infty$, the numbers of left-handed and right-handed quarks are the same, by plugging Eq. 1.8 into Eq. 1.7, we have:

$$\Delta Q_5 = (N_L - N_R)|_{t=\infty} = 2N_f Q_W \tag{1.9}$$

which is the number difference between left-handed and right-handed quarks in the final state.

1.4.2 Chiral Magnetic Effect (CME)

To "activate" the CME effect in the presence of the chirality imbalance introduced by gauge field configurations, a sufficiently strong magnetic field is usually assumed. Under an extremely strong magnetic field (a review of the magnetic fields created in heavy ion collisions can be found in Ref. [Tuc13]), in other words, $eB \gg p^2$ (p is the momentum of a particle), all particles will be on the lowest Landau level, with their spins aligned (positively charged particles) or anti-aligned (negatively charged particles) with the direction of the B field. As

mentioned in the last section, the sphaleron-like transitions-induced topological charge will "convert" the chirality of the quark by flipping its momentum direction (spin flipping is more suppressed by the strong field). An electric current resulting from the net handness of the quarks finally leads to charge separation along the magnetic field. Fig. 1.9 demonstrates the process by only considering one flavor of positively charged quarks in the chiral limit, and the topological charge (chemical potential) is positive. The equation [KMW08] [FKW08] below quantitatively describes the induced electric current.

$$\vec{J} = \frac{e^2 \mu_5}{2\pi^2} \vec{B} \tag{1.10}$$

The experimental detection of the charge separation caused by CME can also be viewed as an avenue to probe the $\mathcal{P}$ breaking in strong interactions. In the Wu experiment [WAH$^+$57] to detect parity violation in weak interactions (Fig. 1.10), the nuclear spins of a sample of cobalt-60 were aligned and the non-uniform emission direction of electrons with respect to the nuclear spin considered as evidence of parity violation in weak interactions. Since in heavy ion collisions, the magnetic field is playing a similar role to the cobalt-60 spin ($\mathcal{P}$-odd), the resulting electric current could be used to detect parity-breaking just as the asymmetric emission of electrons did in the Wu experiment.

1.4.3 Chiral Vortical Effect (CVE)

Non-central heavy ion collision not only produces a strong magnetic field that "drives" the CME, but also create a highly rotating fluid composed of gluons and quarks. In the presence of vorticity $\omega = \frac{1}{2}\vec{\nabla} \times \vec{v}$ ($\vec{v}$ is the flow velocity field) and chirality imbalance ($\mu_5 \neq 0$), a vector current $\vec{J}$ along the vorticity direction can be derived:

$$\vec{J} = \frac{1}{\pi^2} \mu_5 \mu \vec{\omega} \tag{1.11}$$

Here μ is the baryon chemical potential. In this specific case (only one kind of massless quark) shown in Fig. 1.11, the $\vec{\omega}$ is playing a role similar to B in the CME, by converting left-handed quarks to right-handed. Provided there are more quarks than anti-quarks ($\mu > 0$), more right-handed quarks will be moving upward, which leads to a final baryon number current

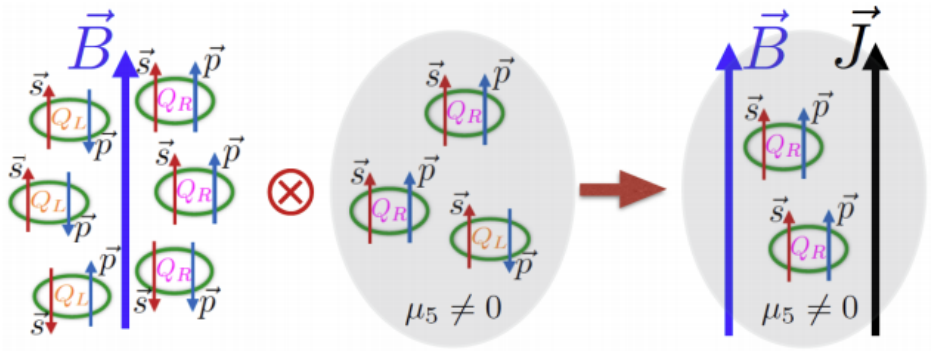

Figure 1.9: Cartoon illustration of the CME for one kind of quarks ($N_f = 1, m_f \to 0, Q > 0, \mu_5 > 0$). Left: in the presence of very strong magnetic field, equal numbers of left-handed (spin and momentum are anti-aligned) and right-handed (spin and momentum are aligned) positively charged quarks are mostly found on the lowest Landau levels. Mid: after interaction with field configuration with positive topological charge (chirality chemical potential, $\mu_5 > 0$), some left-handed quarks will be converted to right-handed ones by flipping their momentum directions. Right: the excessive right-handed quarks after this process results in a current along the magnetic field direction. Figure taken from Ref. [KLVW16].

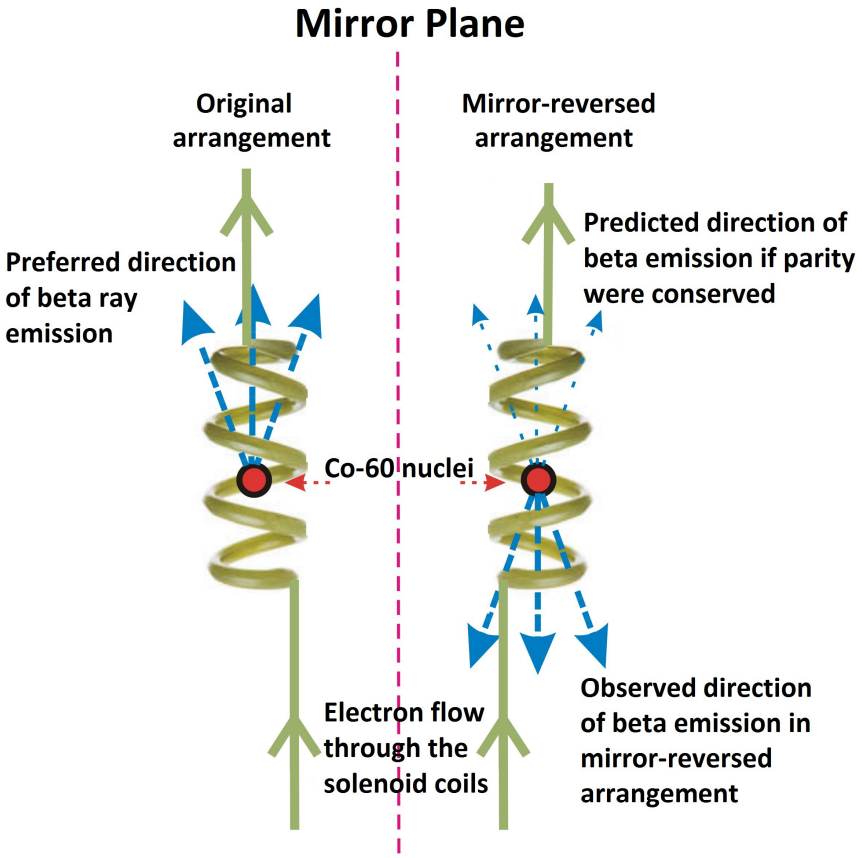

Figure 1.10: Principle of the Wu experiment measuring preferred electron emission direction in cobalt-60 beta-decay, which is used to detect parity-breaking in weak interactions. The CME in heavy ion collisions provides a very similar set-up to probe $\mathcal{P}$-breaking in strong interactions.

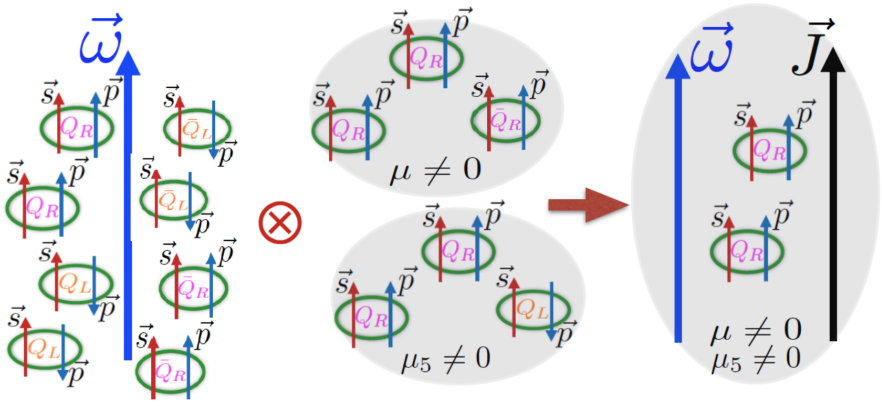

Figure 1.11: Cartoon illustration of the CVE for one kind of quarks/anti-quarks ($m_f \to 0, \mu_5 > 0, \mu > 0$).Figure taken from Ref. [KLVW16].

along the vorticity direction. Thus, a separation of baryons and anti-baryons is expected as a manifestation of the CVE in heavy ion collisions.

CHAPTER 2

STAR Experiment

2.1 The Relativistic Heavy Ion Collider (RHIC)

To investigate the formation of the QGP, the RHIC was constructed at Brookhaven National Lab (BNL) to collide heavy ions ranging from proton to gold nuclei, at collision energies up to 200 GeV/A. These collisions are expected to result in an energy density ten times larger than ordinary nuclear matter. In the sense of a quark matter phase transition, RHIC inverts the process that occurred a few microseconds after the Big Bang, from deconfined state of quark and gluons to ordinary nuclear matter.

The RHIC project rose from the ashes of Isabelle at BNL that was canceled by the Department of Energy (DOE) in 1983 in response to a recommendation made by the High-Energy Physics Advisory Panel (HEPAP). In July 1983, the Nuclear Science Advisory Committee (NSAC) met to decide the next major nuclear physics project and a heavy ion collider was finally prioritized the highest.

The Table 2.1, taken from [HLO03], shows the basic design parameters of the collider. The layout of the collider (Fig 2.2a) consists of two identical quasi-circular concentric rings (blue and yellow, 3.8 km in circumference), allowing for six beam intersections points. The STAR, PHENIX, PHOBOS and BRAHMS detectors are located at four of these points.

Taking gold ions as an example, we describe, below, the acceleration processes the beam goes through in the RHIC complex (see Fig. 2.1 [HLO03]):

1. Gold ions from external source get injected into the Electron Beam Ion Source (EBIS), which is capable of switching different ion beams (all ion species from deuteron to uranium) even pulse by pulse. After acceleration, the gold ions with charge +32 are selected at the

Table 2.1: RHIC Performance Specification

	For Au-Au	For p-p
Beam energy	100→ 30 GeV/nucleon	250→30 GeV
Luminosity	$2 \times 10^{26}\text{cm}^{-2}\text{s}^{-1}$	$1.4 \times 10^{31}\text{cm}^{-2}\text{s}^{-1}$
Number of bunches per ring	60 (→120)	60 (→120)
Luminosity lifetime	$\sim$ 10h	$\sim$ 10h
β^* at collision points	10m→2m (1m)	10m→2m(1m)

exit and carried over to the Booster;

2. Booster Synchrotron further accelerates the ions delivered from the Tandem to 95 MeV/nucleon. At the exit of the Booster, the electrons of the gold ions get stripped again and the charge state reaches +77;

3. The Alternating Gradient Synchrotron (AGS) picks up the ions and boosts the energy of the beam up to 10.8 GeV/nucleon for RHIC injection. The remaining electrons are completely stripped at the exit.

4. Four bunches of ions are stacked and injected sequentially into RHIC from the AGS. The stacking of the beam in the RHIC rings is done in boxcar fashion by repeating the acceleration cycles.

To detect a large range of particles and retain sensitivity to low energy particles emitting out of heavy ion collisions, sophisticated detectors are required for high energy heavy ion collisions. Historically, four major experiments/detectors have been commissioning at RHIC, however, STAR is the only one operating, as of 2018. w

2.2 The Solenoidal Tracker At RHIC (STAR)

Compared to the other detectors at RHIC, STAR was primarily designed to measure hadron production over a large solid angle, with sub-systems capable of precise tracking, momentum analysis and particle identification around the center of mass rapidity. The large acceptance

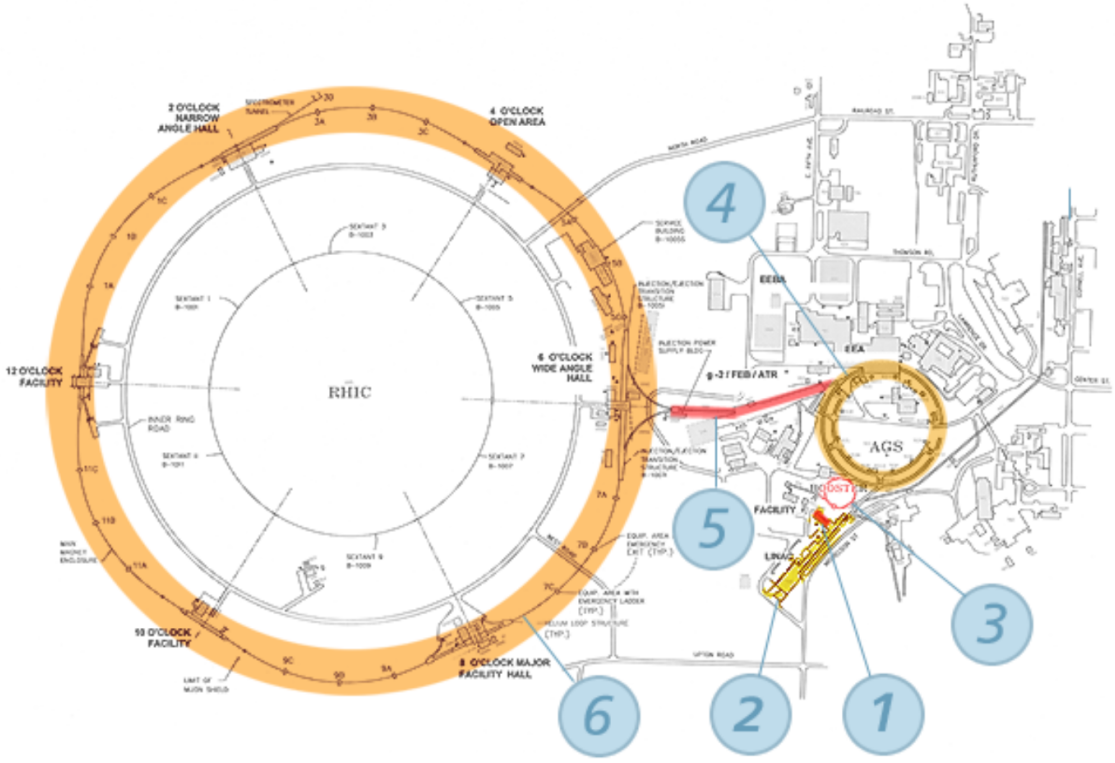

Figure 2.1: Overall configuration of accelerator complex for RHIC. 1. The Electron Beam Ion Source. 2. The Linac. 3. The Booster. 4. The Alternating Gradient Synchrotron. 5. The Relativistic Heavy-Ion Collider.

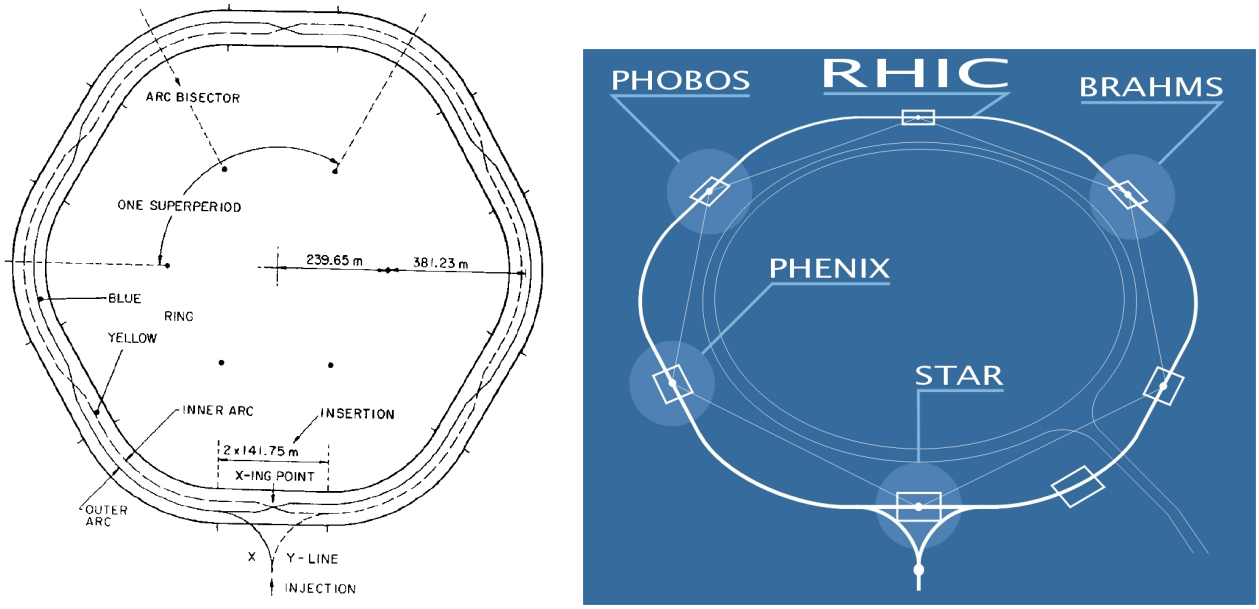

(a) (b)

Figure 2.2: Layout of the RHIC collider and locations of the four experiments.

of STAR makes it suitable for event-by-event characterization of collisions and for the detection of charged hadrons and jets [A$^+$03a].

The major sub-systems of STAR are labeled in Fig. 2.3. The solenoid magnet with normal, water-cooled coils and iron return yoke, provides a uniform magnetic field of maximum value 0.5 T. In the physics analysis (strangeness particle production in AuAu 14.5 GeV collisions and search for chiral effects) for this dissertation, particle tracking and identification information from the Time Projection Chamber (TPC) and Time-of-Flight (TOF) detector are used heavily. In Run 14, the Heavy Flavor Tracker (HFT) was installed for the first time, to extend the measurement capabilities of STAR to finer resolution tracks, closer to the interaction point. This capability especially pertains to physics goals in the heavy flavor domain. The electromagnetic calorimeters (BEMC and EEMC), with $-1 < \eta < 2$ and $\Delta\phi = 2\pi$ coverage, allow for measurements of high transverse momentum photons, electrons and electromagnetically decaying hadrons. Due to the important roles the TPC and TOF play in the physics analysis of this dissertation, their technical design and essential functionalities will be discussed in more detail below.

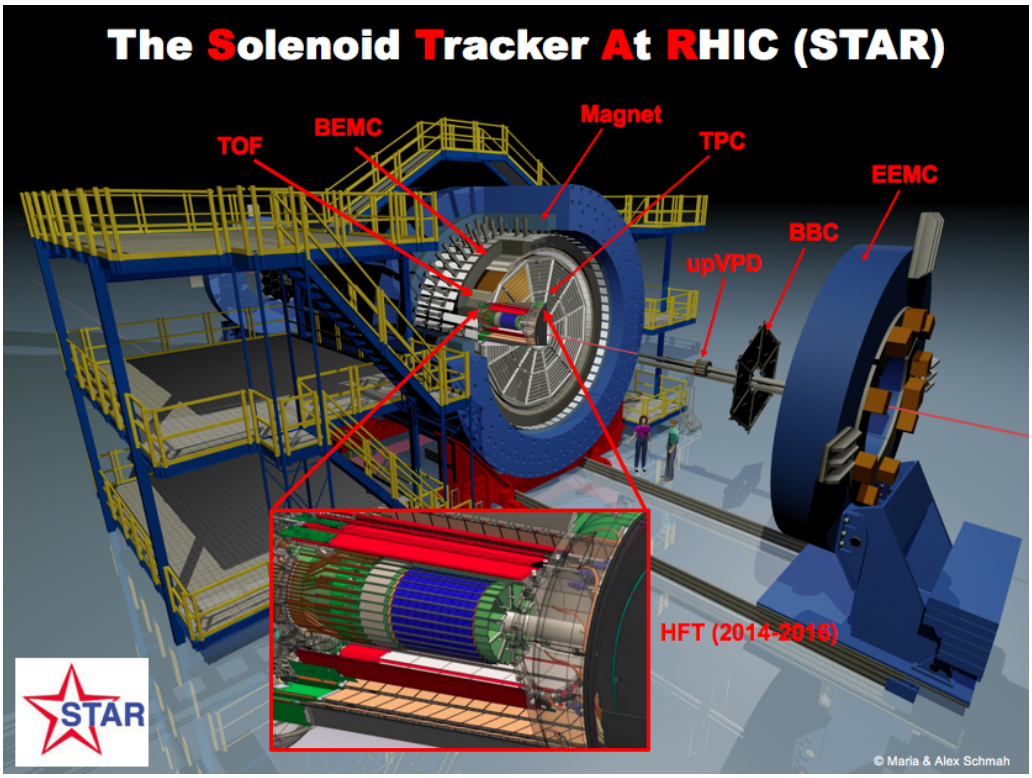

Figure 2.3: STAR sub-systems: Time-of-Flight detector (TOF), Barrel Electromagnetic Calorimeter (BEMC), Magnet, Time Projection Chamber (TPC), up-Vertex Position Detector (upVPD), Beam Beam Counter (BBC), Endcap Electromagnetic Calorimeter (EEMC), Heavy Flavor Tracker (HFT).

2.2.1 The Time Projection Chamber (TPC)

TPC is the major tracking detector in the multipurpose STAR experiment. It is designed to provide functionalities for:

- recording thousands of particle tracks per heavy ion collision/event;
- measurements of the momenta of the tracks;
- particle identification via charge sign and ionization energy loss rate measurement.

TPC provides full azimuthal angle coverage over $[-1.8, 1.8]$ units of pseudo-rapidity for the full range of multiplicities. The momenta of the particles are measureable in the range from 100 MeV/c up to 30 GeV/c and particle identification is reliable for tracks with momenta from 100 MeV/c to 1 GeV/c.

As shown in Fig. 2.4, the STAR TPC is 4.2 m long and 4 m in diameter, sitting in a large solenoidal magnet and surrounding the beam-beam interaction region at the 6 o'clock position in the RHIC ring. This detector is essentially an empty volume of gas in a well-defined, uniform electric field of $\sim 135 V/cm$. The electric field is defined by the thin conductive Central Membrane (CM) at the center of the TPC, together with the concentric field-cage cylinders and the readout end-caps. When the primary ionizing particles go through this volume, the released secondary electrons drift towards the readout end-caps and are detected by finely segmented readout pads. Software is used to precisely reconstruct the track path. The working gas in the TPC is P10 which consists of 10% methane and 90% argon operated at 2 mbar above atmospheric pressure. With this choice of gas composition and pressure, a fast drift velocity at a low electric field can be attained.

Multi-Wire Proportional Chambers (MWPC) and readout pads (Fig. 2.5) form the readout system of TPC on the end-caps. The pads measure the image charge induced by the drifting electron avalanche in the chamber and make precise reconstruction of original track possible. The configuration of readout pads, shown in Fig. 2.5, is designed to optimize the dE/dx measurements, momentum resolution and and two-track resolution.

The capability of measuring energy loss rate in the gas makes the TPC a powerful device to identify particles with relatively low momenta, as shown in Fig. 2.6 [CKM+18]. However, as energy goes up, the dE/dx becomes less mass-dependent and the separation of particle species becomes more difficult. In the relatively higher energy range, the weak point of TPC Particle Identification (PID) capability can be complemented by the Time-Of-Flight TOF system, which will be discussed in the next section.

The summary of important technical specifications of the STAR TPC can be found in the Table. 2.2[A+03d].

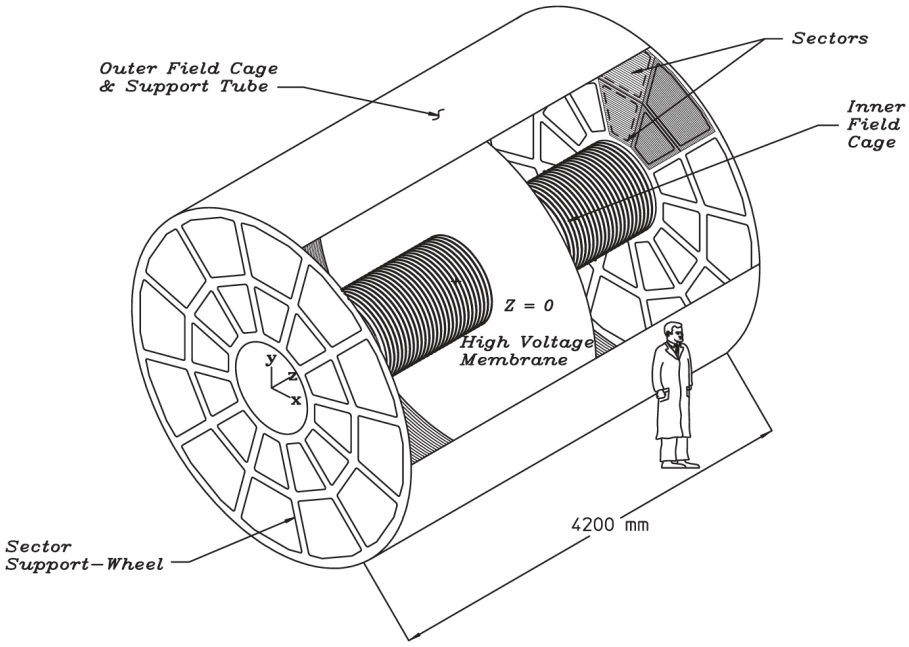

Figure 2.4: TPC schematic diagram.

2.2.2 The Time of Flight (TOF) Detector

As stated above, the TPC is a extremely powerful detector in terms of tracking efficiency, momentum resolution, and energy loss measurements. However, one shortcoming of the system is it can only provide Particle Identification (PID) for relatively low momentum particles emitted in the collisions. As shown in Fig. 2.6, the PID information for kaons (protons) only exists in the momentum p range $0.1 \lesssim p \lesssim 0.7$ GeV/c ($0.1 \lesssim p \lesssim 1.0$ GeV/c).

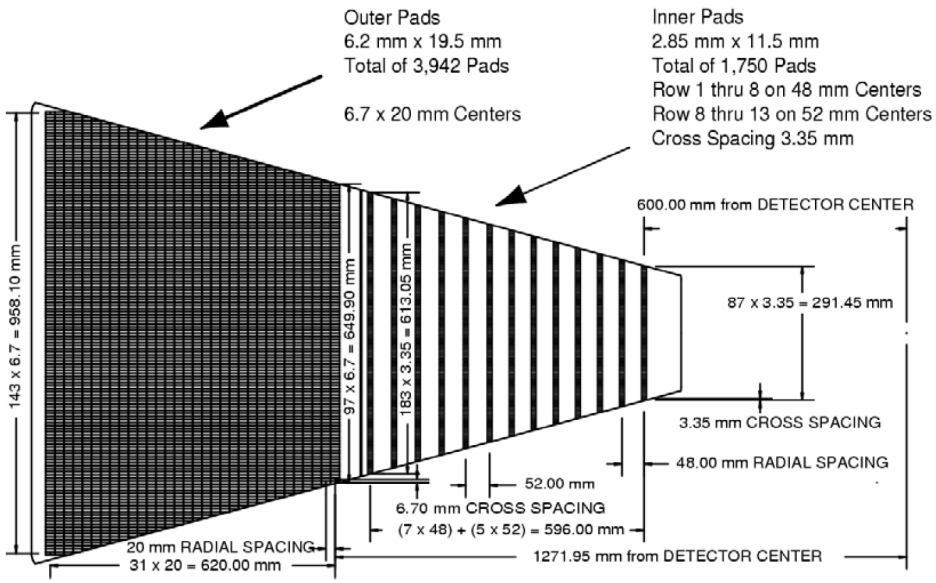

Figure 2.5: The TPC anode plane with one full sector.

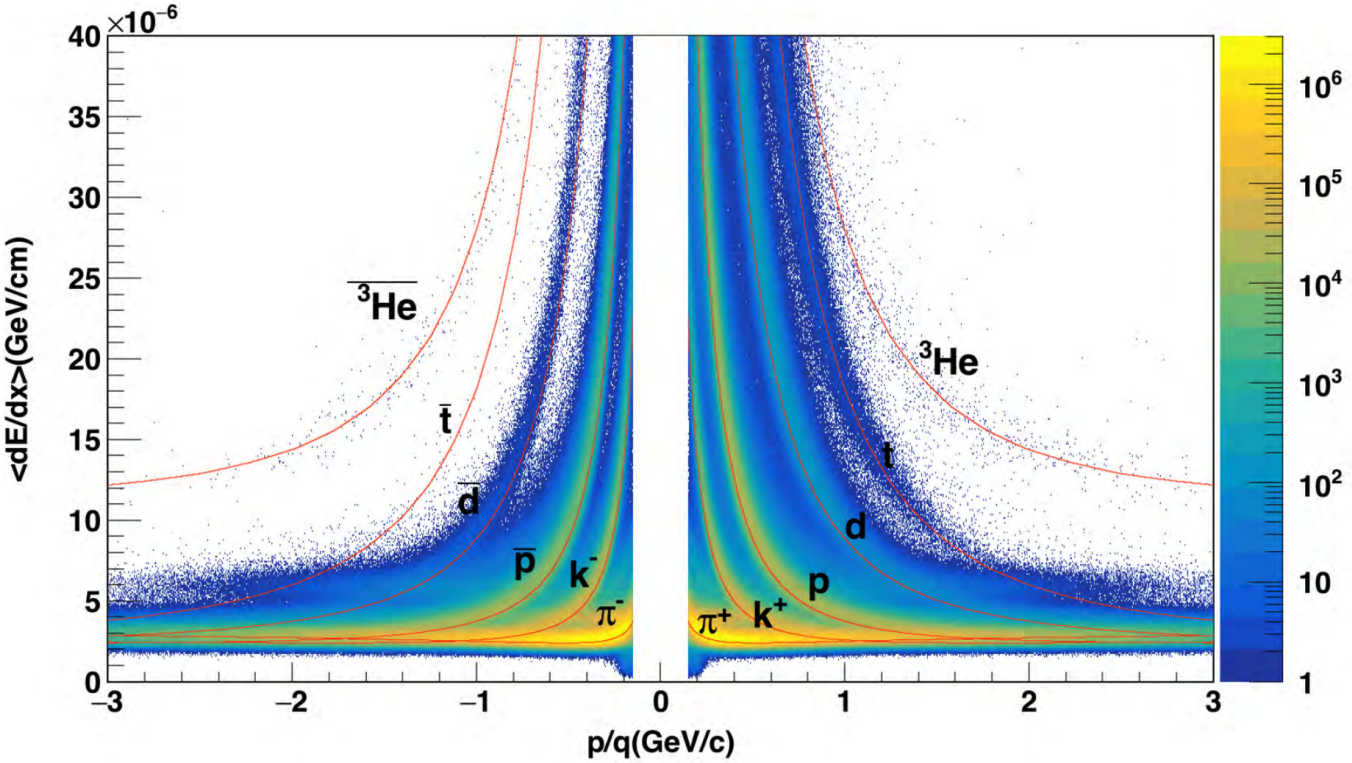

Figure 2.6: The energy loss ($\langle dE/dx \rangle$) for charged tracks at midrapidity ($|y| < 0.5$) as a function of the momentum per charge in Au+Au collisions at $\sqrt{s_{NN}} = 200$ GeV. The magnetic field is 0.5 T. The curves are based on the Bethe-Bloch formula.

Table 2.2: STAR TPC technical parameters

Item	Dimension	Comment
Length of the TPC	420 cm	Two halves, 210 cm long
Outer Diameter of the Drift Volume	400 cm	200 cm radius
Inner Diameter of the Drift Volume	100 cm	50 cm radius
Dist. between Cathode and Ground Plane	209.3 cm	Each side
Cathode	400cm diameter	At the center of the TPC
Cathode Potential	28 kV	Typical
Drift Gas	P10	10% methane, 90% argon
Pressure	Atm. + 2mbar	Regulated at 2mbar above Atm.
Drift Velocity	5.45 cm/μs	Typical
Transverse Diffusion (σ)	230 $\mu m/\sqrt{cm}$	140 V/cm & .5 T
Longitudinal Diffusion (σ)	360 $\mu m/\sqrt{cm}$	140 V/cm
Number of Anodes Sectors	24	12 per end
Number of Pads	136,608	
Signal to Noise Ratio	20 : 1	
Electronic Shaping Time	180ns	FWHM
Signal Dynamic Range	10 bits	
Sampling Rate	9.4 MHz	
Sampling Depth	512 time buckets	380 time buckets typical
Magnetic Field	0, $\pm$.25T, $\pm$.5T	Solenoidal

A critical question about the particle production mechanisms in Au+Au collisions at RHIC energies is the competition between soft, non-perturbative processes and hard processes at high transverse momentum. To better solve the puzzle of the collision dynamics, identified particle spectra covering a wider transverse momentum range becomes very useful. The need to add new systems for direct particle identification in the higher transverse momentum region becomes apparent and the Time-of-Flight (TOF) sub-detector was proposed and installed on STAR over the period 2004-2010 to further improve the PID capability of STAR.

2.2.2.1 Physics Benefits

Below lists a few examples of the physics benefits gained by the design of the TOF system:

1. In the search for a phase transition and possible critical phenomena near the QCD phase boundary, event-by-event fluctuation analysis of conserved quantum numbers (electric charge, baryon number, and strangeness) is considered to be a unique tool. The TOF upgrade may reduce the statistical error to 10-15% for the measurement of event-by-event kaon and proton yields in central Au+Au collisions.

2. Since resonances continue to decay, scatter and regenerate after their primary production, the precise measurement of the resonance yields provides a unique avenue to trace the system evolution between hadron formation and final decoupling of the system. The added TOF system may improve the STAR PID reach into the 1-2 GeV/c momentum range, and finally can effectively reduce decay daughter misidentification and combinatorial backgrounds, making resonance measurements for the $(\rho, \Delta, \Lambda(1520)...)$ at STAR a precision tool to study hadronic dynamics.

3. To study the early stages of the collision and to search for possible partonic collectivity, precise and definite measurements of elliptic flow for multi-strange baryons and heavy mesons (Ω, D mesons and possibly J/ψ) is highly desired and can be fulfilled with the additional PID capability provided by the barrel TOF.

In this thesis work, including the reconstruction of ϕ meson and identification of π, K, p for the charge separation signal study, heavy use is made of the information from the TOF.

2.2.2.2 Detector Design and Configuration

Around 2010, a large-area Time-of-Flight system has been fully installed in the STAR experiment at RHIC. The detectors are based on Multigap Resistive Plate Chambers (MRPCs) and are digitized using custom electronics based on "NINO" and "HPTDC" chips. The 120 trays of the full TOF system are arranged in two adjoining rings of 60 trays each immediately outside of the STAR TPC (see Fig. 2.7 for reference, the TOFp tray, which is gone now, is showing the location of one tray). The entire system covers full azimuth and $-0.9 \sim 0.9$ pseudo-rapidity. In each tray, there are 32 MRPCs arranged nearly projectively for collisions occuring at the center of STAR.

The multi-gap resistive plate chamber (MRPC) technology was invented by CERN [CZCH$^+$96]. Resistive Plate Chambers (RPC) have been developed in 1990's at CERN to meet the requirements of inexpensive detectors which have good timing and space resolution. However, conventional types (narrow/wide gap) of RPCs suffer from either low rate capability or poor timing resolution. The MRPC was developed to improve the timing resolution while maintaining the relatively high rate capabity by dividing up the wide gap RPC into a number of slices. It can be observed from Fig. 2.8 that an MRPC consists of a stack of resistive plates (usually glass) with a series of uniform gas gaps. By applying a high voltage across the electrodes that are on the outer surfaces of the outer plates, a strong electric field will be generated within each gas gap. When a charged particle goes through the chamber, electron avalanches will be generated. The glass plates are transparent to charge induction from avalanches in the gaps due to their high resistivity. The signals are produced up at copper pickup pads which are attached immediately on the outside of the electrodes.

2.2.2.3 Detector Performance

The TOF MRPC design was finalized in 2001, a few full-scale protypes were tested in STAR before the full installation for Run 10 [Llo12]. The first five final trays ran stably during the Run 8 p+p collisions and the particle identification capability is shown in Fig. 2.9. The total time resolution versus electronic board ID is shown in Fig. 2.10. Due to the incomplete

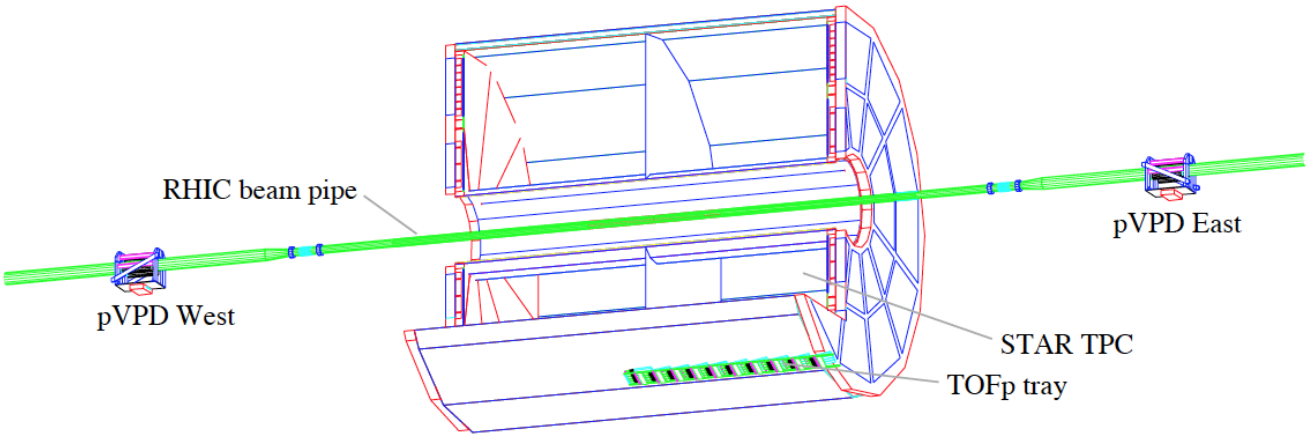

Figure 2.7: The location of the TOFp detectors in relation to the STAR TPC and the RHIC beam pipe.

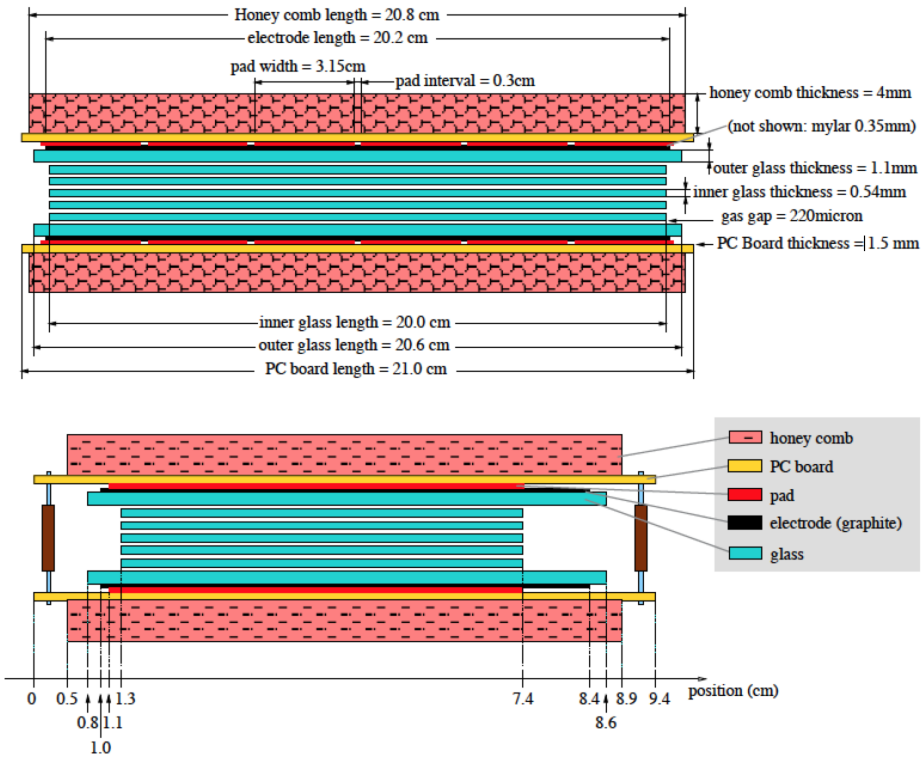

Figure 2.8: Two side views of the structure of an MRPC module. The upper (lower) view shows the long (short) edge.

TPC calibration, the data used to obtain the time resolution in Run9 was sub-optimal. The time resolution was further improved to sub-100 ps, which meets the requirements based on the physics goals in the full Run 10 run.

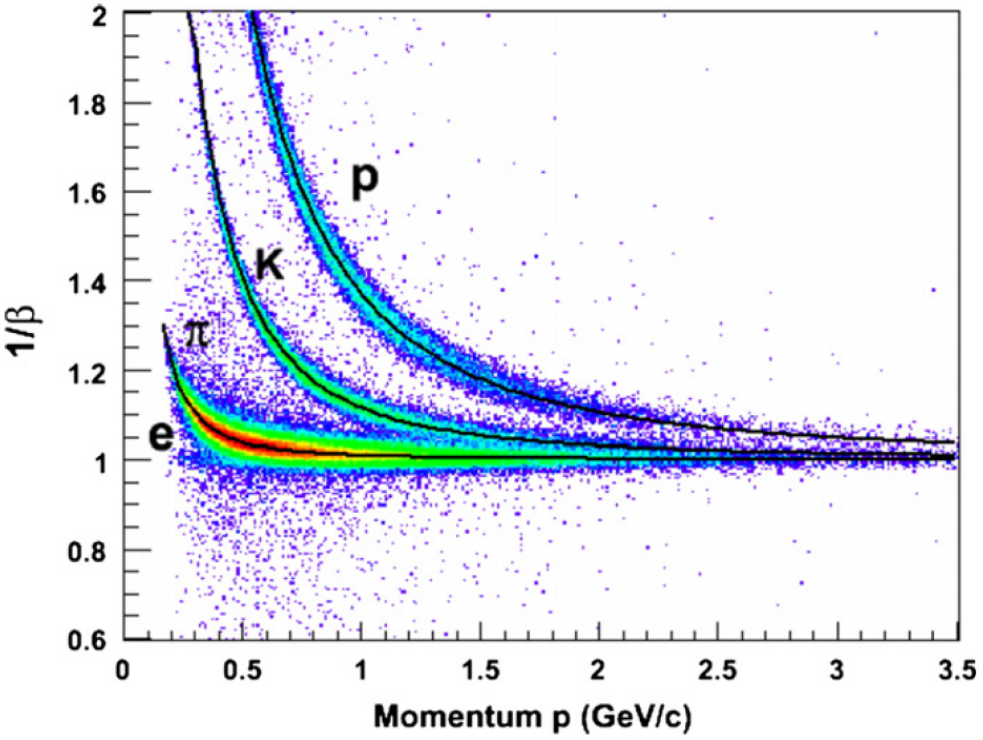

Figure 2.9: The PID performance of the first five final TOF trays that ran through RHIC Run 8.

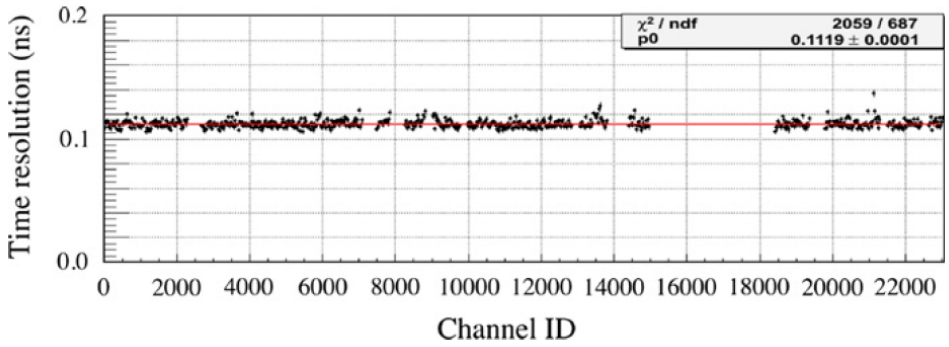

Figure 2.10: The total time resolution for the three-quarters installed STAR TOF system during RHIC Run 9.

CHAPTER 3

Strange Particle Reconstruction

This chapter is devoted to illustrating the techniques to reconstruct strange particles ($\Omega^-/\bar{\Omega}^+, \phi$), as well as the procedures applied to measure the production of these particles in Au+Au collisions at $\sqrt{s_{NN}} = 14.5$ GeV.

3.1 Data

The measurement of $\Omega^-(\bar{\Omega}^+)$ and ϕ production in Au+Au 14.5 GeV collisions was carried out using the minimum bias triggered data collected by STAR in year 2014. The analysis carried out in this thesis work requires the minimum bias (MB) trigger condition. The trigger ID set is listed in Table 3.1.

The v_r cut in the event selection criteria (Table 3.2) is used to include most of the collisions away from the beam pipe. From Figure 3.1, we find most of collisions are concentrated within a small area in the xy plane and by applying the v_r cut, we can effectively eliminate background from collisions between a projectile ion and the wall of the beam pipe or with the residual gas in the vacuum. The vertex z position cut (v_z cut, Fig. 3.2) can guarantee reasonably consistent detector acceptance for the events sample. After event cuts (see next section), the total number of the remaining events is close to 15 million.

3.2 Centrality Bin Determination

The nuclear matter created in central and peripheral heavy ion collisions may differ dramatically, thus, it is more meaningful to differentiate between measurements based on different

Table 3.1: Minimal Bias Triggers

Trigger Label	Offline Trigger ID
VPD_mb	440001
ZDC_mb	440004
BBC_mb	440005
BBC_mb	440015

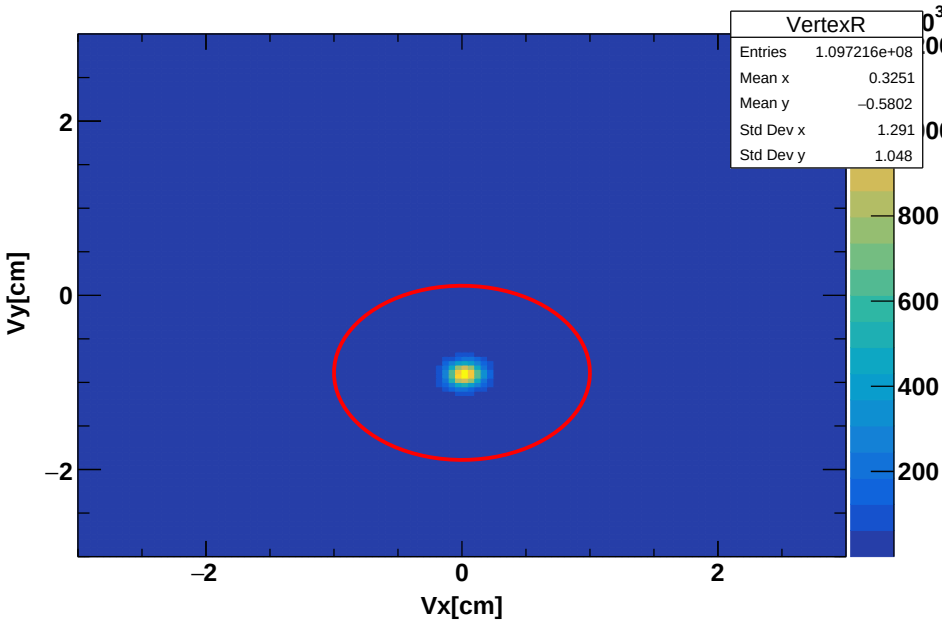

Figure 3.1: Distribution of vertex position in the xy plane. The red circle denotes the v_r cuts.

Table 3.2: Event selection criteria for Au+Au 14.5 GeV collisions

Cuts	Value
Vertex Z position (v_z)	-50.0 cm $\leq v_z \leq 50.0$ cm
Vertex R position ($v_r = \sqrt{v_x^2 + (v_y + 0.89)^2}$)	$v_r \leq 1.0$ cm

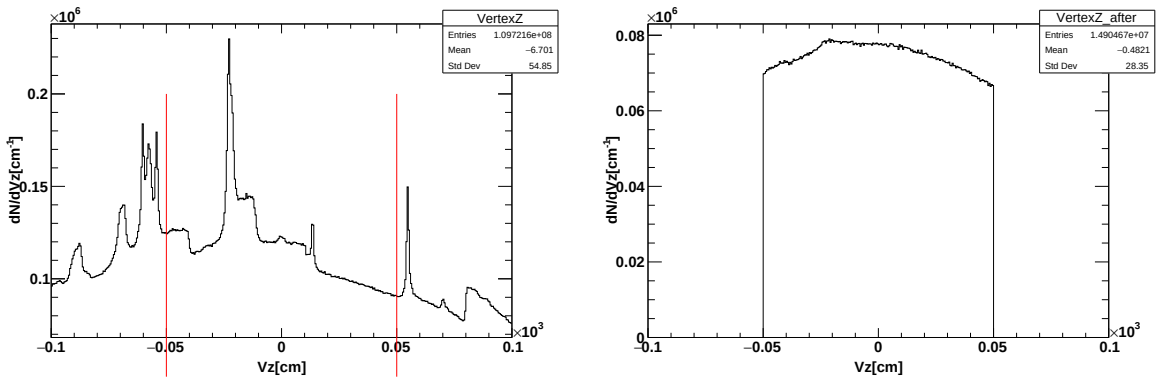

(a) (b)

Figure 3.2: a) Distribution of the z position of the primary vertex. b) Distribution of primary vertex z position after event selection.

collision configurations. Given the incapability of STAR detector to "see" the microscopic geometry of each collision event, a tool is required that can bridge the gap between the experimental observables and the underlying geometric quantities of the collisions. The Glauber model [MRSS07] was developed to address this problem and due to its simplicity of implementation using Monte Carlo simulation, it enjoys great popularity in the high energy particle and nuclear physics communities.

The Glauber Model is built on a hypothesis of independent linear trajectories of the constituent nucleons, which makes it possible to derive analytical expressions for the nucleus-nucleus interaction cross section, the number of interaction nucleons and the number of binary nucleon-nucleon collisions.

However, compared to theoretical calculations, the Monte Carlo approach is proven simpler to implement and easier to make direct comparison to experimental data. The detailed implementation of the Glauber Monte Carlo (GMC) varies, but the soul of the procedures is as follows (in an A+B collision scenario):

- A and B nucleons of nucleus A and B are populated in a three dimensional space based on the input nuclear density distributions.
- The impact parameter b is randomly drawn from $d\sigma/db = 2\pi b$.

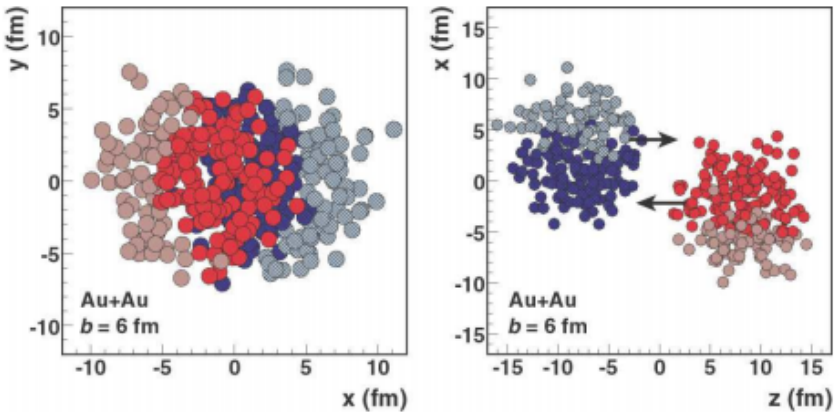

Figure 3.3: Glauber Monte Carlo event (Au+Au at $\sqrt{s_{NN}} = 200$ GeV with impact parameter $b = 6$ fm viewed in the transverse plane (left panel) and along the beam axis (right panel). The nuclei are drawn with a radius $\sqrt{\sigma_{\text{inel}}^{\text{NN}}}/2$. Disks with a darker color represent participating nucleons.

- The nucleus-nucleus collision is simulated by a sequence of nucleon-nucleon collisions (straight-line trajectories and constant inelastic nucleon-nucleon cross-section are assumed). In the simplest version of the GMC, it is assumed that the collision happens as long as the distance d between nucleons in the plane orthogonal to the beam axis has the following relationship with inelastic cross-section:

$$d \leq \sqrt{\sigma_{\text{inel}}^{\text{NN}}/\pi} \tag{3.1}$$

Fig. 3.3 shows an example Glauber event with impact parameter $b = 6$ fm.

To make theoretical calculation comparable to experimental results regarding different collision configurations, it is important to build mapping relationships between observable quantities (N_{ch}) and microscopic collision configurations (N_{part}, N_{coll}...). Before describing the procedure of producing the map, a few assumptions involved have to be introduced first.

An essential step to connect the Glauber simulation and experiment is to make the simulated reference multiplicity match the data. It is found the Negative Binomial Distribution (NBD) describes the $p+p$ collision multiplicity distribution fairly well, and this idea can generalized to heavy ion collisions by assuming the nucleus-nucleus collision is a superposition

of multiple $p+p$ processes

$$dN_{\rm ch}/d\eta = \Sigma_{i=0}^{\lceil m \rceil} X_i \tag{3.2}$$

where

$$m = [xN_{\rm coll} + (1-x)N_{\rm part}/2] \tag{3.3}$$

$$X \sim {\rm NB}(n_{pp}; \langle n_{pp} \rangle, k) \tag{3.4}$$

$${\rm NB}(n_{pp}; \langle n_{pp} \rangle, k) = \left(\begin{array}{c} n_{pp}+k-1 \\ k-1 \end{array} \right) \left[\frac{\langle n_{pp} \rangle / k}{1 + \langle n_{pp} \rangle / k} \right]^{n_{pp}} \frac{1}{[1 + \langle n_{pp} \rangle / k]^k} \tag{3.5}$$

However, the quantity $\lceil m \rceil$, denoting the effective number of $p+p$ collisions, is estimated from the GMC rather than using the sum of the mass numbers of colliding nuclei. In this expression, the hard processes contribution x, which scales with $N_{\rm coll}$ is extracted empirically from previous PHOBOS results ($x = 0.12 \pm 0.01 \pm 0.05$). The remaining term, $(1-x)N_{\rm part}/2$, corresponds to contribution from the $N_{\rm part}$-scaled soft interactions. In Eq. 3.5, n_{pp} represents the multiplicity of $p+p$ collisions of corresponding energy and k is related to the variance of the NBD.

Since STAR uses TPC tracks ($|\eta| < 0.5, -70$ cm $< v_z < 70$ cm for AuAu 14.5 GeV) for reference multiplicity counting, the reconstruction efficiency correction by using $\epsilon_{\rm reco} = 0.9(1 - N_{ch}/2520)$ (2520 is the number extracted empirically from previous studies) has to be applied to the raw distribution before the matching process between GMC and experiment takes place.

The matching process between GMC and data requires the determination of the optimal free parameter set in Eq. 3.5. Although this task sounds straight-forward, it is very computationally intensive and some specific algorithms (e.g., a hybrid of MC hill-climbing and simulated annealing) have been developed to speed it up. After the optimal set of parameters is attained, the binning of multiplicity can be carried out using the simulated distribution and the corresponding centrality cut can be used for experimental measurements. With all of these ready, for each centrality bin, the GMC events can be used to compute the mean

value of $N_{\rm coll}$ and $N_{\rm part}$. Table. 3.4 and Table. 3.3 tabulate these two quantities and their systematic uncertainties, respectively, for each 10% centrality bin in Au+Au collisions at $\sqrt{s_{\rm NN}} = 14.5$ GeV. Fig. 3.5 demonstrates the multiplicity binning and Figure 3.6 shows the distribution of events in each centrality bin.

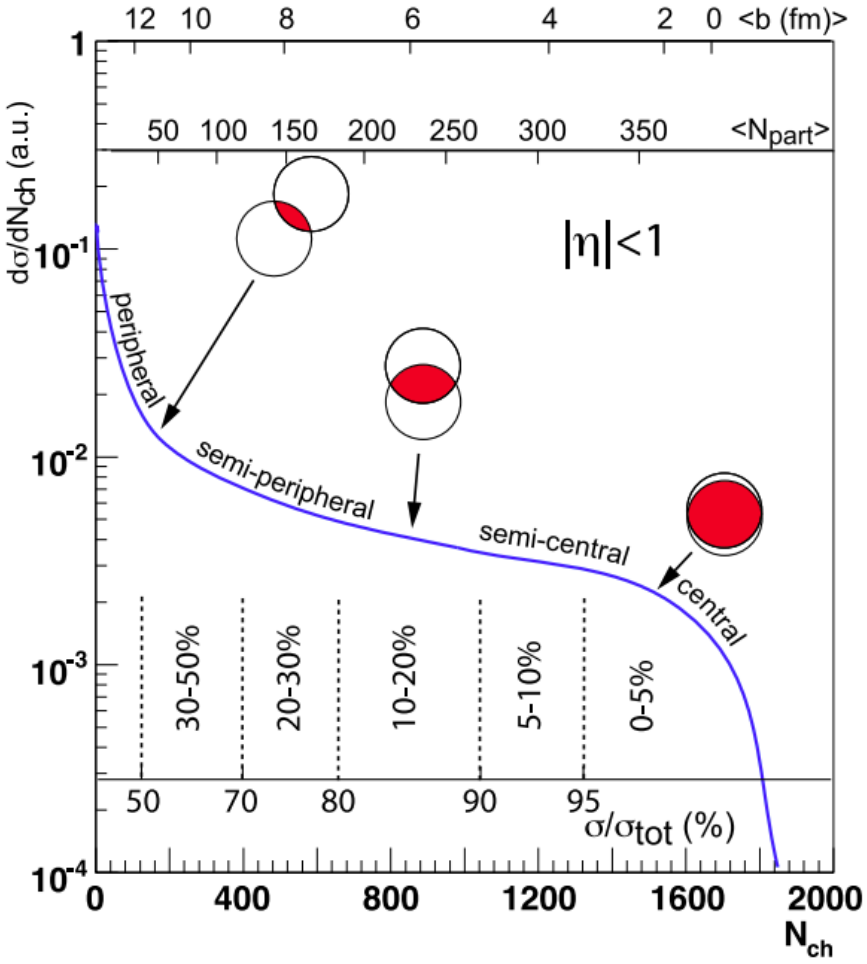

Figure 3.4: The correspondence between charged particle multiplicity and $N_{\rm part}$, impact parameter b. The numbers on the figure are not actual measurements.

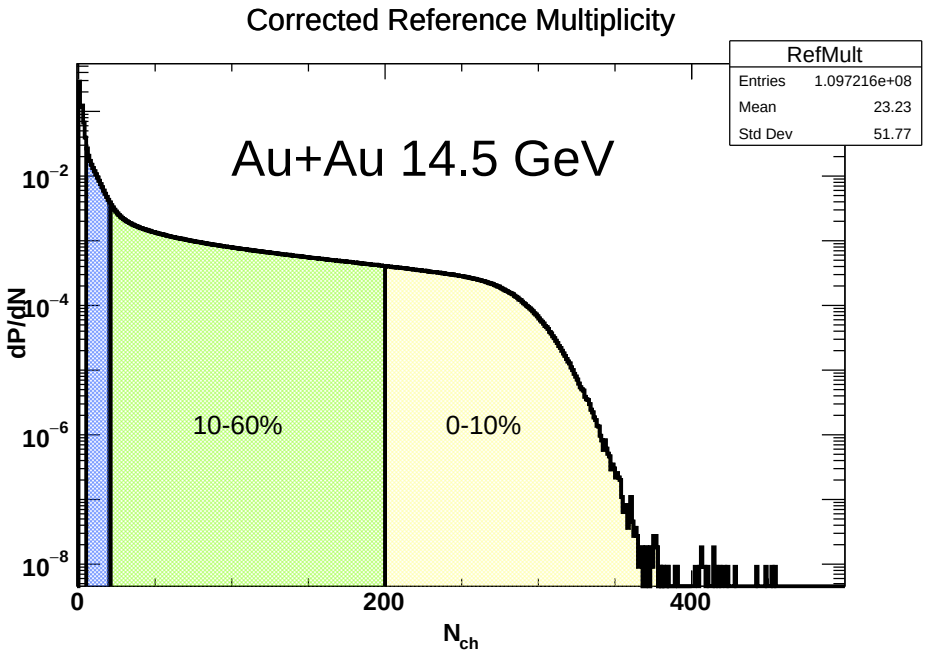

Figure 3.5: Normalized corrected reference multiplicity distribution for Au+Au 14.5 GeV at STAR. The colored area represents the labeled fraction of the most central collisions. The blue area corresponds to $60-80\%$ collisions.

Table 3.3: Npart for centrality bins in Au+Au 14.5 GeV at STAR

Centrality	Npart	syst. err
$0-10\%$	313.755	3.59404
$10-20\%$	225.593	8.48373
$20-30\%$	158.731	9.86
$30-40\%$	108.064	10.4546
$40-50\%$	70.4698	9.76026
$50-60\%$	43.5221	8.14685
$60-70\%$	25.5712	7.5898
$70-80\%$	14.0593	4.84536

3.3 $\Omega^-(\bar{\Omega}^+)$ Baryon Reconstruction

3.3.1 Reconstruction Cuts

The $\Omega^-/\bar{\Omega}^+$ baryon ($m = 1672.45 \pm 0.29$ MeV, $c\tau = 2.461$ cm [T$^+$18]) is hard to directly detect in STAR due to its short decay length. However, its charged decay daughters from

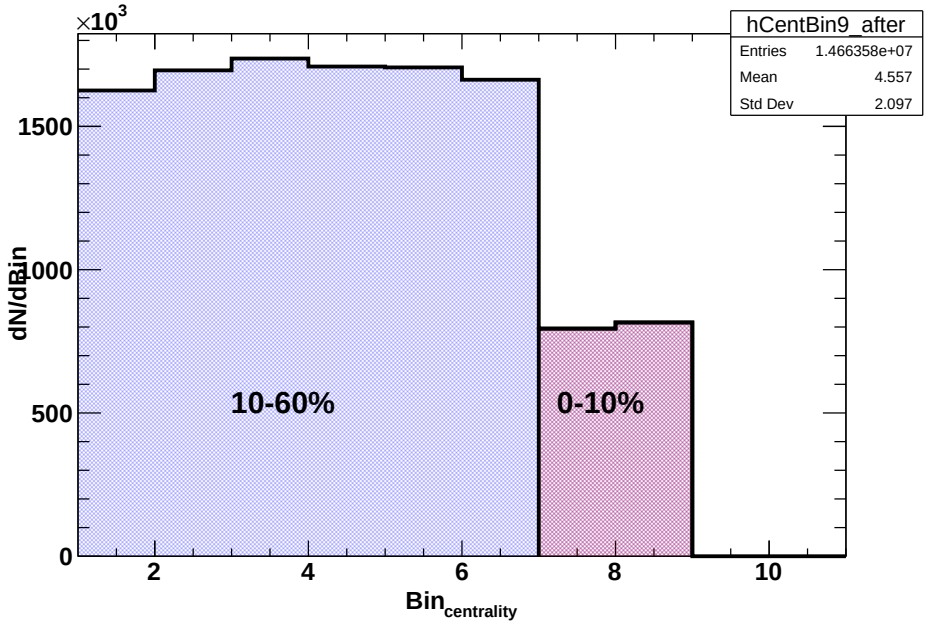

Figure 3.6: Distribution of centrality bins defined in Au+Au 14.5 GeV by the **StRefMultCorr** class of STAR computing library. In $\Omega^-(\bar{\Omega}^+)$ analysis, due to the very low yield, bins are combined for $0-10\%$ and $10-60\%$ central collisions.

Table 3.4: Ncoll for centrality bins in Au+Au 14.5 GeV at STAR

Centrality	Ncoll	syst. err
$0-10\%$	711.486	27.3585
$10-20\%$	454.215	23.5591
$20-30\%$	282.678	24.2263
$30-40\%$	167.971	22.1882
$40-50\%$	94.3089	17.6944
$50-60\%$	49.8735	12.3042
$60-70\%$	25.2342	8.78222
$70-80\%$	12.1316	5.08722

the channels we chose ($\Omega^- \to \Lambda^0 K^- \to p\pi^- K^-$, $\bar{\Omega}^+ \to p^-\pi^+ K^+$, with $BR = (67.8 \pm 0.7)\%$), can all be recorded by the TPC, thus making it possible to reconstruct the primary $\Omega^-(\bar{\Omega}^+)$ baryons emitted from collisions.

Taken from Ref. [Jia05], Fig. 3.7 schematically plots the decay topology of $\Xi^- \to \Lambda^0\pi^- \to p\pi^-\pi^-$. Due to the same topology that $\Omega^- \to \Lambda^0 K^- \to p\pi^- K^-$ shares with Ξ^-, this diagram can also be used to represent the decay chain we utilized to reconstruct primary Ω^-, by replacing the bachelor π^- in Ξ^- with K^- for Ω^-. Table. 3.5 summarizes all of the cuts (track cuts and topological cuts) for $\Omega^-(\bar{\Omega}^+)$ reconstruction. Fig. 3.8-Fig. 3.9 illustrate the items that are labeled for further explanation in the table. The diagrams are all, of course, exaggerated for demonstration purposes. The decay daughters that survive all of these cuts will be used to compute the invariant mass of the $\Omega^-(\bar{\Omega}^+)$. From the energy conservation law in the lab frame, we have (in natural units):

$$E^2_{\Omega^-} = E^2_{\Lambda} + E^2_{K^-} + 2E_{\Lambda}E_{K^-} \tag{3.6}$$

$$E^2_{\Omega^-} = \vec{p}^{\,2}_{\Omega^-} + m^2_{\Omega^-}, E^2_{\Lambda} = \vec{p}^{\,2}_{\Omega^-} + M^2_{\Lambda}, E^2_{K^-} = \vec{p}^{\,2}_{K^-} + M^2_{K^-} \tag{3.7}$$

The mass terms in the above equations are all the rest masses of the corresponding particles. Since we also have $\vec{p}_{\Omega^-} = \vec{p}_{\Lambda} + \vec{p}_{K^-}$ due to momentum conservation, the mass of the reconstructed Ω^- is:

$$m^2_{\Omega^-} = M^2_{\Lambda} + M^2_{K^-} + 2(E_{\Lambda}E_{K^-} - \vec{p}_{\Lambda^0}\vec{p}_{K^-}) \tag{3.8}$$

The Particle Data Group (PDG) mass, rather than measured mass, is used for the terms denoted by M in the calculation. Similar formula can be derived for Λ reconstruction, which is a prerequisite to reconstruct Ω^-.

For each candidate of $\Omega^-(\bar{\Omega}^+)$, we compute its invariant mass using Eq. 3.8 and fill a histogram with the value for further analysis.

3.3.2 Signal Extraction

Figure 3.11 to Figure 3.14 show the reconstructed $\Omega^-(\bar{\Omega}^+)$ invariant mass distributions for different centralities and transverse momentum (p_T) range. Although careful cuts have been applied to get rid of misidentified daughters and to veto unqualified decay topologies, a significant level of combinatorial background still exists. The purity of the signal increases as the p_T rises and collisions becomes more peripheral. Overall, the background level is

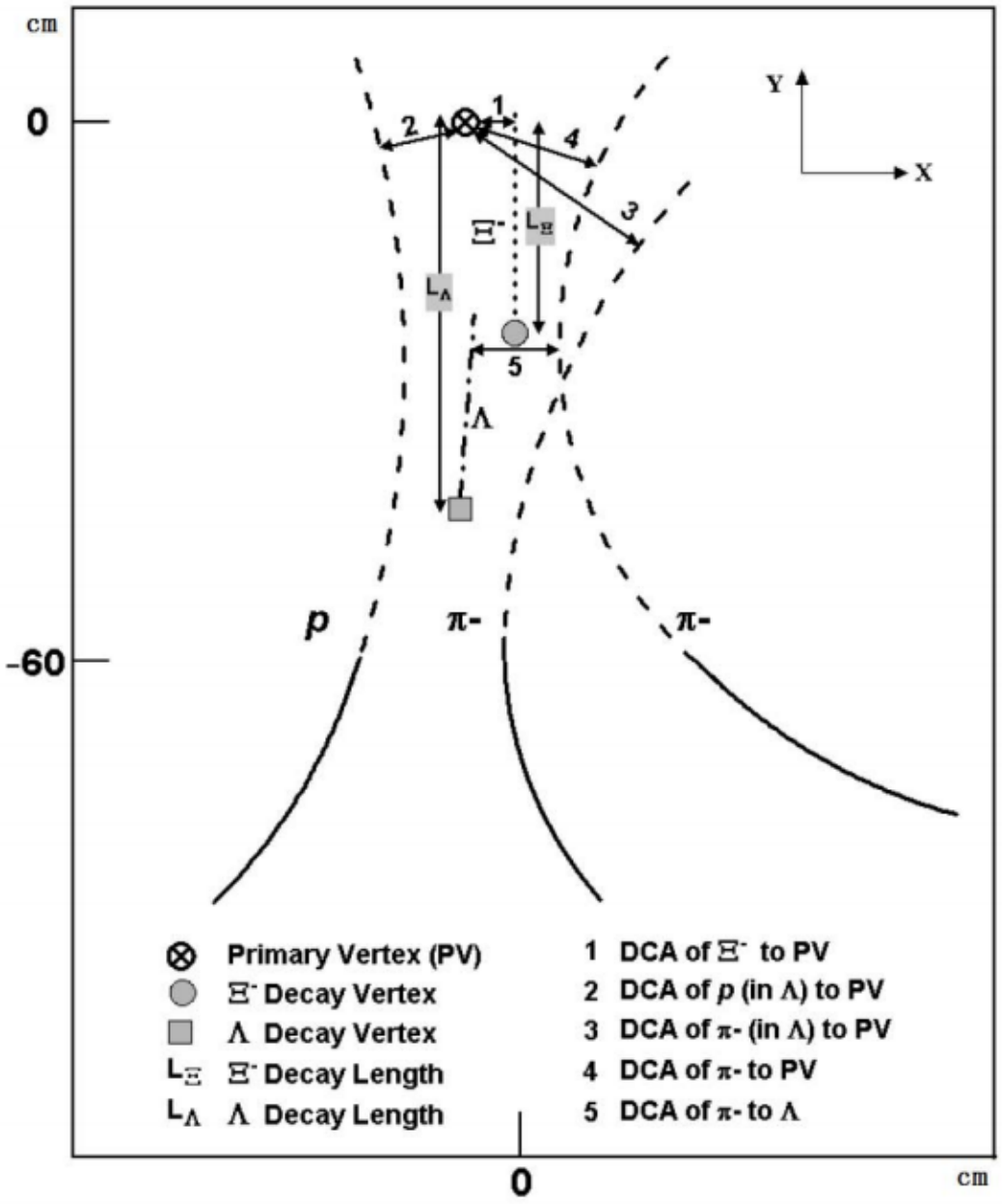

Figure 3.7: Ξ^- weak decay topology. Due to the same topology with $\Xi^- \to \Lambda^0\pi^- \to p\pi^-\pi^-$, this diagram can also be used to illustrate the decay chain of $\Omega^- \to \Lambda^0 K^- \to p\pi K^-$ by replacing the bachelor π^- with K^-. Here DCA stands for "Distance of Closest Approach", i.e., the closest possible distance between two track helices. Replace the decay daughters with their antiparticles for $\bar{\Omega}^+$ reconstruction.

higher than the data collected in previous years due to the additional material from newly installed Heavy Flavor Tracker (HFT) and its supporting structure, through which the low

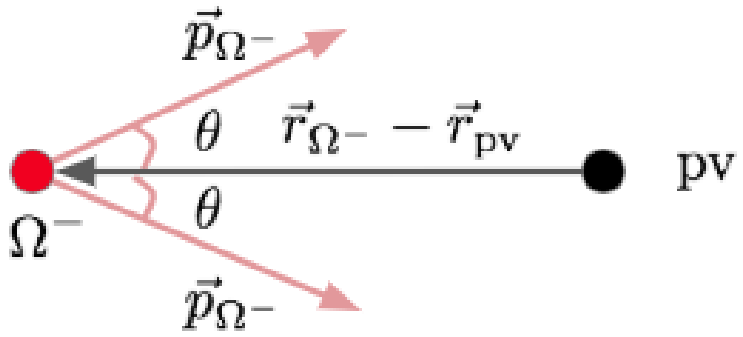

Figure 3.8: Forward decay cut. The decay topology shown above is not allowed in primary $\Omega^-(\bar{\Omega}^+)$ reconstruction and the same cuts apply to $\Lambda(\bar{\Lambda})$ decay from $\Omega^-(\bar{\Omega}^+)$ candidates.

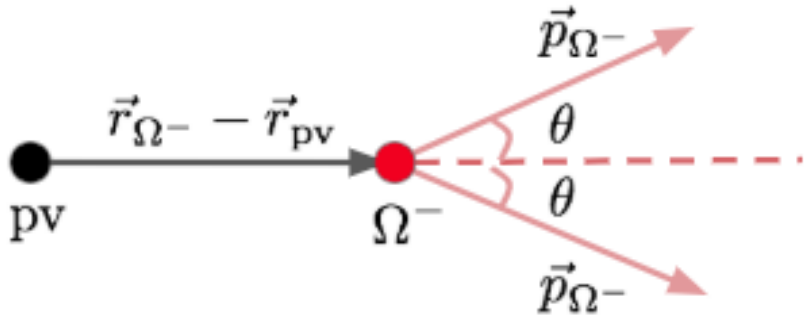

Figure 3.9: $\sin\theta$ cut for $\Omega^-(\bar{\Omega}^+)$. The analysis allows $\vec{p}_{\Omega^-}$ to deviate from the direction of the $\vec{r}_{\Omega^-} - \vec{r}_{\rm pv}$ (pv: primary vertex) only by a small angle.

transverse momentum particles has to transverse before hitting the TPC volume.

These techniques are usually employed to estimate the background in the invariant mass distributions:

- Side band estimation: use side band level to approximate the background level within the peak. This method is usually used when signal counts are very low and function fitting is difficult.
- Function fitting: fit the background shape with a polynomial function. This method requires relatively significant number of background counts.

Table 3.5: Reconstruction cuts for $\Omega^-(\Omega^- \to \Lambda^0 K^- \to p\pi^- K^-)$

Track Cuts	Values
$\lvert y \rvert$ of Ω^-	< 0.5
p_T of π^-, p, and K^-	$> .15$ GeV/c
# of TPC hits of π^-, p from Λ^0	> 15
# of TPC hits of K^- from Ω^-	> 15
$\lvert N\sigma \rvert$ for π^-	< 4.0
$\lvert N\sigma \rvert$ for p	< 3.0
$\lvert N\sigma \rvert$ for K^-	< 4.0
Topological Cuts	**Values (unit)**
DCA from p to primary vertex	> 0.6 cm
DCA from π^- to primary vertex	> 2.0 cm
DCA from K^- to primary vertex	> 1.0 cm
DCA from p to π^-	< 0.7 cm
DCA from Λ^0 to primary vertex	> 0.4 cm
Decay length ($L^{\Lambda^0}_{\rm decay}$) of Λ^0	> 5.0 cm
$\lvert M_{p\pi^-} - M^{\rm PDG}_{\Lambda^0} \rvert$	< 6 MeV/c^2
DCA from Λ^0 to K^-	< 0.7 cm
Decay Length ($L^{\Omega^-}_{\rm decay}$) of Ω^-	> 3.0 cm
$L^{\Omega^-}_{\rm decay}$ - $L^{\Lambda^0}_{\rm decay}$	> 0.0
DCA from Ω^- to primary vertex	< 0.4 cm
$(\vec{r}_{\Lambda^0} - \vec{r}_{\Omega^-}) \cdot \vec{p}_{\Lambda}$ (see Figure 3.8)	> 0
$(\vec{r}_{\Omega^-} - \vec{r}_{\rm PV}) \cdot \vec{p}_{\Omega^-}$ (see Figure 3.8)	> 0
$\sin\theta$ of Ω^-(see Figure 3.9)	< 0.15
$\lvert M_{\Lambda^0\pi^-} - M^{\rm PDG}_{\Xi^-} \rvert$	> 10 MeV/c^2

- Rotational background: rotate daughter tracks to obtain the invariant mass spectrum of combinatorial background.

In the $\Omega^-(\bar{\Omega}^+)$ production study, the rotation method is used (see Figure 3.10). The combinatorial background comes from mis-matched decay daughters and the rotation method mimics the mechanism by rotating the K^- track with a certain angle to manually create a mis-matched track, while maintaining the background correlation. After running the new candidate (with rotated daughter) through all of the topological cuts, if it still survives, its invariant mass will be computed and filled into a rotation background invariant mass histogram. The red markers in Figure 3.11 to Figure 3.14 are the rotation background reconstructed with angle $\theta = \pi$. The two-side band windows defined by two pairs of magenta vertical dashed lines ($[1.625\ \text{GeV}/c^2, 1.655\ \text{GeV}/c^2]$ and $[1.69\ \text{GeV}/c^2, 1.72\ \text{GeV}/c^2]$) are used to match the background and real data. We can see the rotation background reproduces the background shape fairly well, therefore it is used for background subtraction within the signal peak. To count the number of $\Omega^-(\bar{\Omega}^+)$ within the peak, several approaches are available. Bin-counting and function fitting are the most common ones. In this study, we used the bin-counting method and compared to the function fitting result to estimate the systematic uncertainty. The mass window for counting is $[1.66\ \text{GeV}/c^2, 1.685\ \text{GeV}/c^2]$.

3.3.3 Raw Transverse Momentum Spectra of $\Omega^-(\bar{\Omega}^+)$

Given the extracted number of $\Omega^-(\bar{\Omega}^+)$ within $|y| < 0.5$ from the detector data, we are ready to construct the raw transverse momentum spectra of Ω^- and Ω^+ for different centralities. The data points on the spectra are computed using the following equation (taking the Ω^- as the example):

$$y = \frac{\Delta N_{\Omega^-}}{2\pi N_{\text{events}} p_T \Delta p_T \Delta y \cdot \text{BR}} \tag{3.9}$$

where ΔN_{Ω^-} is the number of the Ω^- within the Δp_T and Δy range and BR is the branching ratio of the decay channel used to reconstruct Ω^- ($\text{BR}_{\Omega^- \to \Lambda K^- \to p\pi^- K^-} = \text{BR}_{\Omega^- \to \Lambda K^-} \cdot \text{BR}_{\Lambda \to p\pi^-} = 0.678 \times 0.639$).

However, due to the high multiplicity of high energy nucleus-nucleus collisions, STAR is not able to reconstruct tracks with 100% efficiency. Also, the reconstructed tracks could be smeared so that some candidates get lost during reconstruction. Detector acceptance,

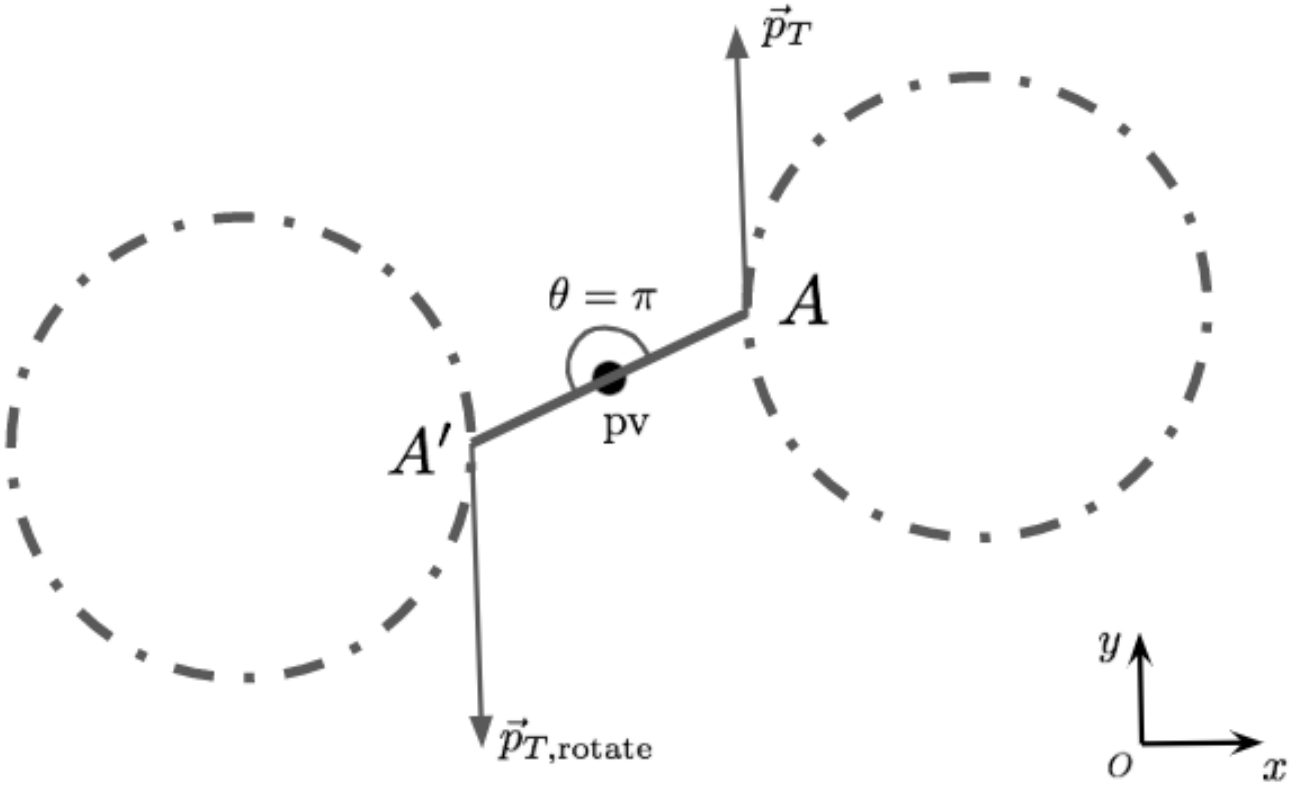

Figure 3.10: Diagram of track rotation. The broken line is the projection of the track helix onto the $x - y$ plane; pv is the primary vertex; $A(A')$ is the origin of the real track helix (rotated helix); θ is the rotation angle. In this analysis, we used $\theta = \pi$.

e.g., dead areas in the TPC, may also introduce inefficiencies when we compute the yield of $\Omega^-(\bar{\Omega}^+)$. To correct back all of these physical effects, we first embed some $\Omega^-(\bar{\Omega}^+)$ particles into real events and simulate the events through the reconstruction chain at STAR, and then apply the same track and topological cuts to the embedding data. Finally, the reconstruction efficiency can be computed by comparing the embedding yield to the input. When we do embedding at STAR, two p_T distributions (exponential and flat) are used for the input particles in order to generate efficiencies with small statistical error in both low and high transverse momentum range. Fig. 3.17 and Fig. 3.19 show the efficiency error as a function of p_T for both exponential and flat input distributions. It can be easily seen that the error from exponential samples is smaller than flat ones when $p_T < 1.5$ GeV/c. By contrast, the flat samples yield more precise results in other p_T ranges. Therefore, we combine these two distributions to get the final efficiency corrections, as shown in Figure 3.18 and Figure 3.20.

The corrected spectra of Ω^- and $\bar{\Omega}^+$ will be shown in Chapter 5. There is one thing that is worth pointing out here. It is not easy to measure $\Omega^-(\bar{\Omega}^+)$ production in the low p_T range due to the low reconstruction efficiency. A common approach to address this difficulty is fitting the corrected spectra with an analytical function and the total yield (dN/dy) of $\Omega^-(\bar{\Omega}^+)$ can be extracted by integrating the function over the entire transverse momentum range. There are a couple of choices regarding the fitting function:

- Levy function:

$$f(p_T) = \frac{dN}{dy} \cdot \frac{(a-1)(a-2)}{2\pi a(aT + m(a-2)} (1 + \frac{\sqrt{p_T^2 + m^2} - m}{aT})^a \tag{3.10}$$

- Boltzmann function:

$$f(p_T) = \frac{dN}{dy} \cdot \frac{\sqrt{p_T^2 + m^2}}{2\pi T(m^2 + 2mT + 2T^2)} \exp(-\frac{\sqrt{p_T^2 + m^2} - m}{T}) \tag{3.11}$$

- Exponential function:

$$f(p_T) = \frac{dN}{dy} \cdot \frac{m + T}{2\pi T} \exp(-\frac{\sqrt{p_T^2 + m^2} - m}{T}) \tag{3.12}$$

In this study, the Levy function is used to determine the yield dN/dy and the deviations from the other two functions are used to estimate the systematic error.

3.3.4 Systematic uncertainty estimation

Various aspects of analysis may contribute to the systematic uncertainties in the final result. For the study presented above, three sources of systematics are investigated: reconstruction cuts, signal extraction method and fitting functions for the corrected spectra.

If we vary the sets of reconstruction cuts for Ω, different invariant mass spectrum will be produced, which finally leads to different uncorrected raw transverse momentum spectra. However, embedding simulation is expected to correct all these artificial effects back and generate only one corrected spectrum. In reality, this cannot be achieved given the limited capability of embedding process to perfectly capture the detector response. Therefore, a specific set of reconstruction cuts may introduce bias into the final result and varying some crucial cuts in both embedding and real data and using them to compute the final result enable us to estimate how big the bias could be. For example, in this Ω production study, the cuts in Table 3.6 are varied and for each cut, the biggest deviation from the original measurement is counted as the uncertainty for that specific cut and the uncertainties due to each group of cuts are added in quadrature.

Table 3.6: Reconstruction cuts for systematic uncertainties estimation

# of TPC hits	≥ 15	≥ 20	≥ 25
DCA from Ω to primary vertex	< 0.5 cm	< 0.7 cm	
DCA between Λ and K	< 0.9 cm	< 1.1 cm	
Decay length of Ω	> 4.0 cm	> 5.0 cm	> 6.0 cm

To extract the raw counts of Ω from invariant mass histograms for each p_T and centrality bin, instead of bin-counting, Gaussian function can be used to fit the peak and the total counts can be obtained from the fitting function integral. Additionally, the mass window for counting can also be varied to estimate the bias originating from the default setting.

As mentioned above, the dN/dy result relies upon the fitting function chosen for unmeasured p_T range. To account for this effect, two alternative functions (Equation 3.11 and 3.12) are used to fit the final corrected spectra and the largest difference between the results from

these two functions and the default Levy function is counted as the systematic uncertainty due to the fitting function.

Similar procedures are also applied to ϕ mesons measurement which is presented in next section. The cuts that are varied for the systematics estimation are shown in Table. 3.7.

Table 3.7: Reconstruction cuts combinations for ϕ mesons

# of TPC hits	≥ 15	≥ 20	≥ 25
$\lvert n\sigma_{\text{Kaon}}\rvert$	≤ 2.5	≤ 2.0	≤ 1.5
DCA to primay vertex	≤ 3.5 cm	≤ 3.0 cm	≤ 2.5 cm

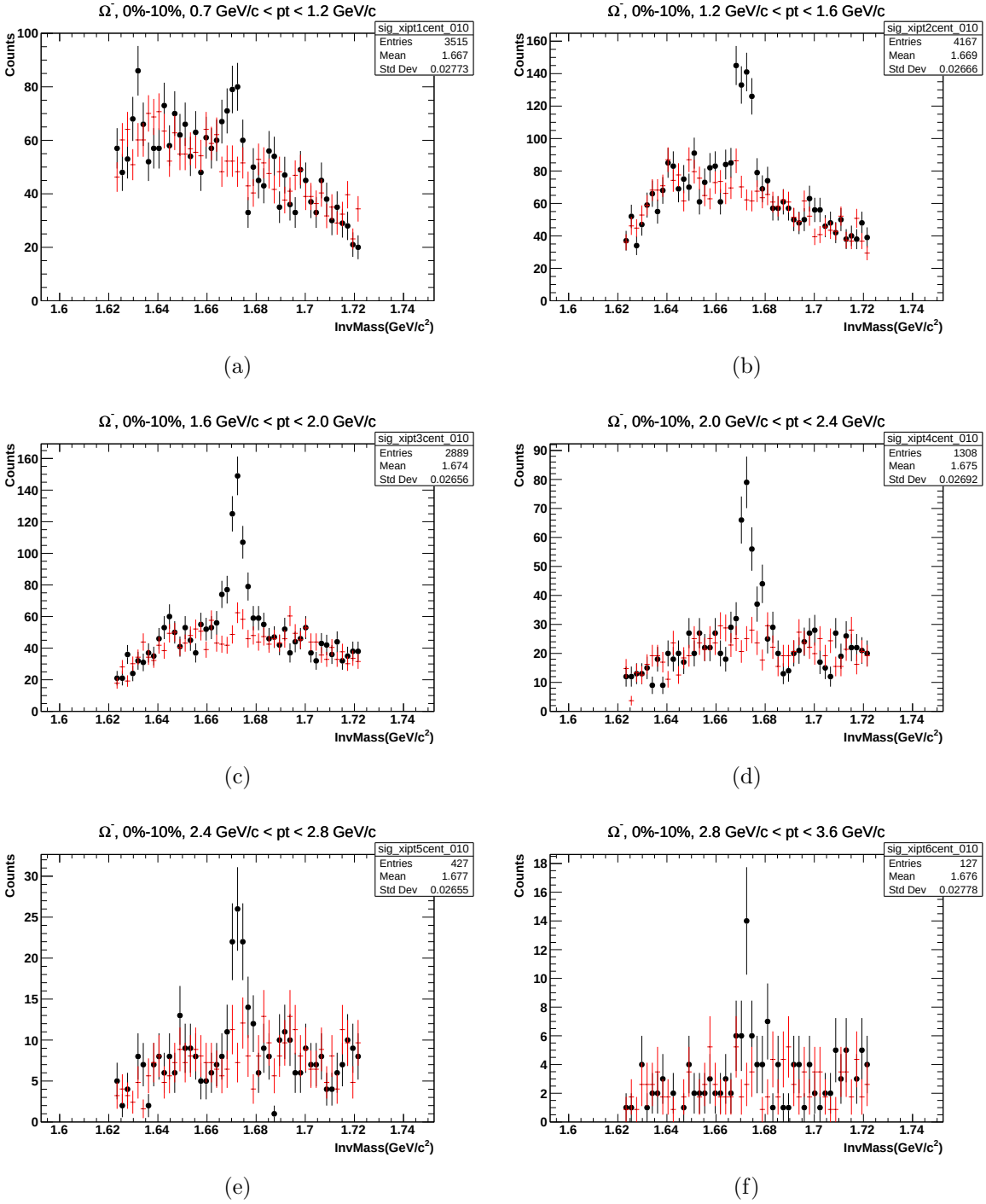

Figure 3.11: (a)-(f) The invariant mass distribution (black markers) of reconstructed Ω^-s in labeled pt bins for $0-10\%$ central Au+Au collisions at $\sqrt{s_{NN}} = 14.5$ GeV. Red markers represent the rotational background normalized using the two side-band windows defined by the two pairs of magenta dashed lines. The signal is the sum of the counts within the mass window defined by the two blue dashed lines.

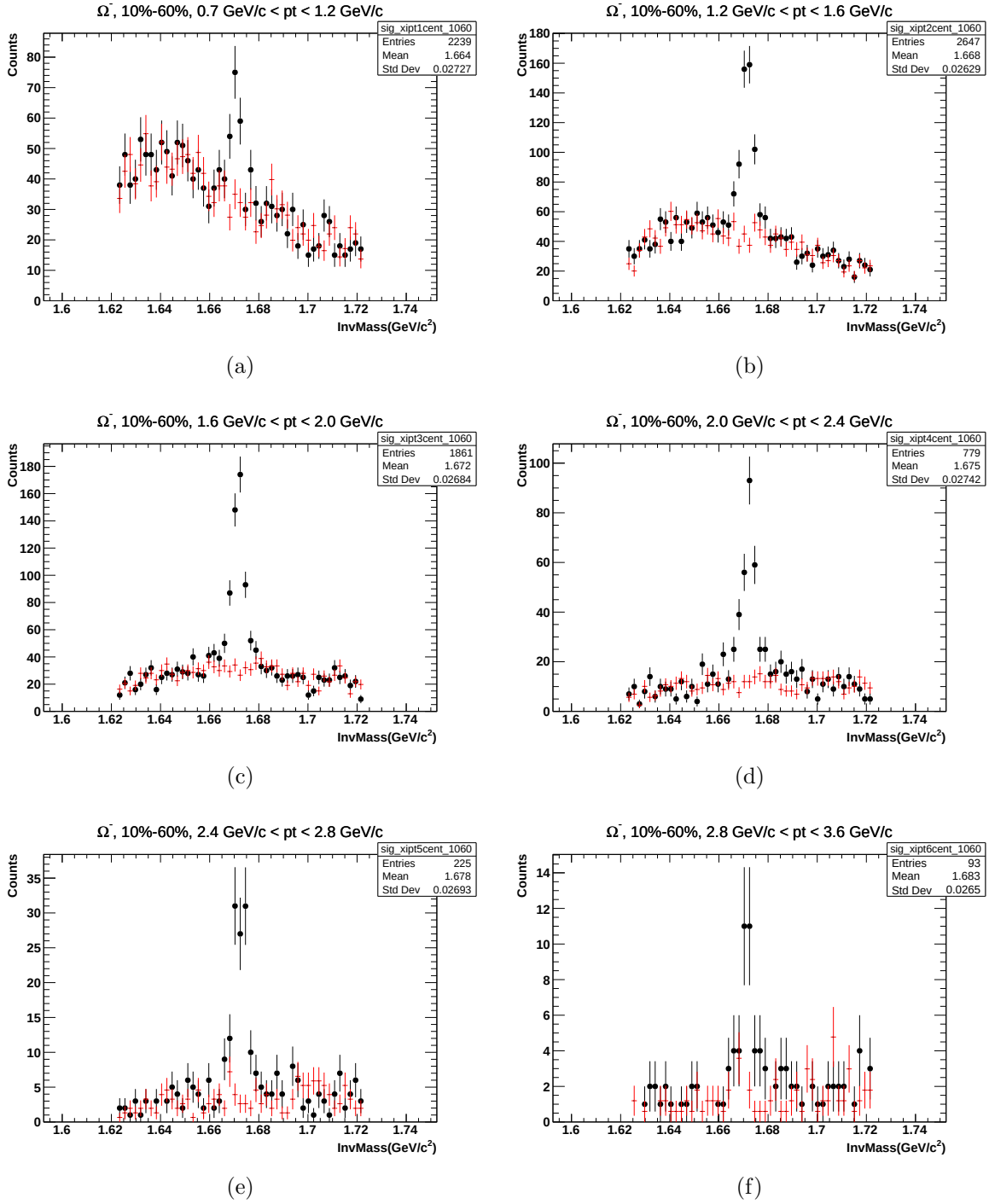

Figure 3.12: (a)-(f) The invariant mass distribution of reconstructed Ω^{-}s in labeled pt bins for $10-60\%$ central Au+Au collisions at $\sqrt{s_{NN}} = 14.5$ GeV. Red markers represent the rotational background normalized within the two side-band windows denoted by magenta dashed lines. The signal is the sum of the counts within the mass window defined by the two blue dashed lines.

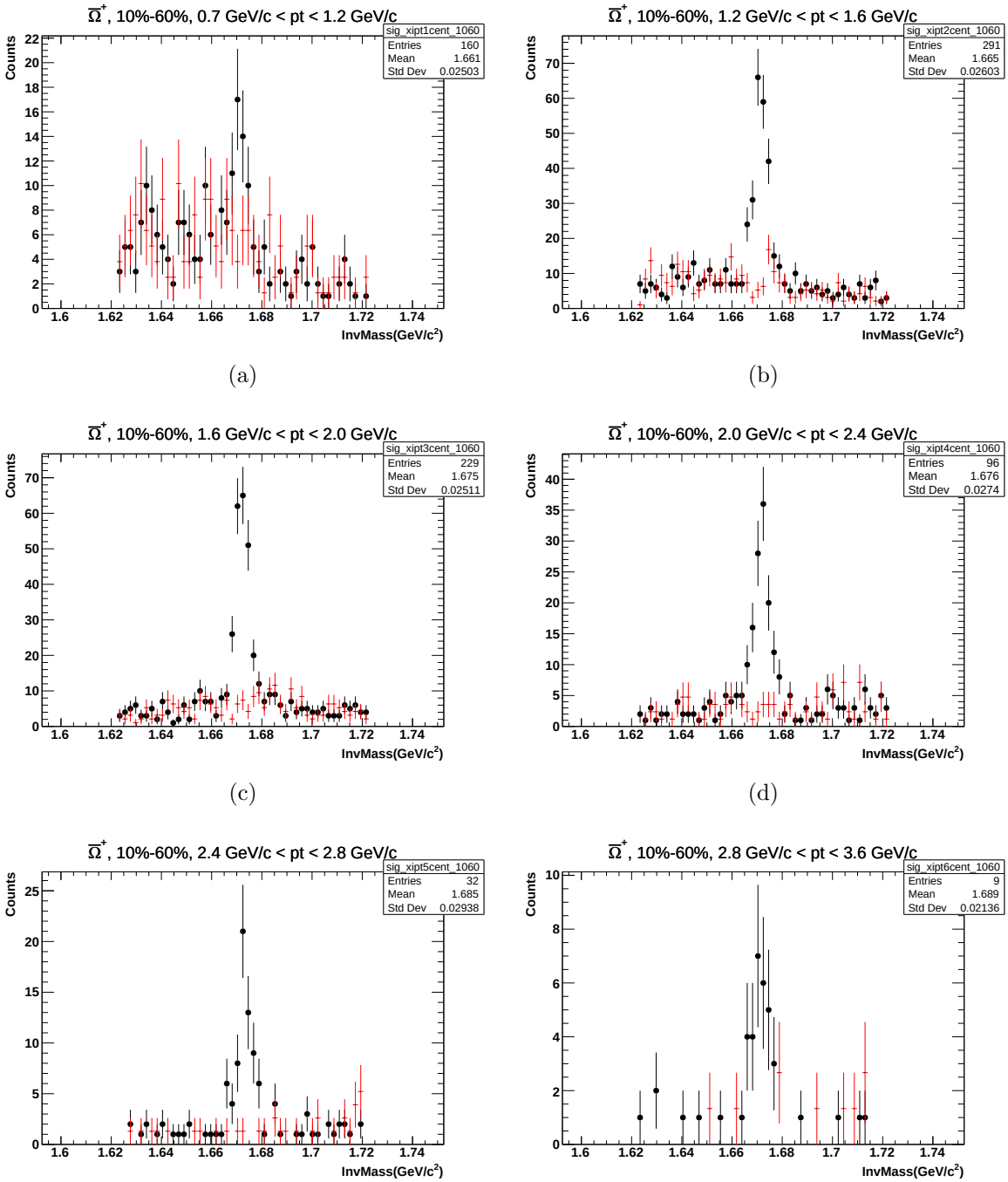

Figure 3.13: (a)-(f) The invariant mass distribution of reconstructed $\bar{\Omega}^+$s in labeled pt bins for $0-10\%$ central Au+Au collisions at $\sqrt{s_{NN}} = 14.5$ GeV. Red markers represent the rotational background normalized within the two side-band windows denoted by magenta dashed lines. The signal is the sum of the counts within the mass window defined by the two blue dashed lines.

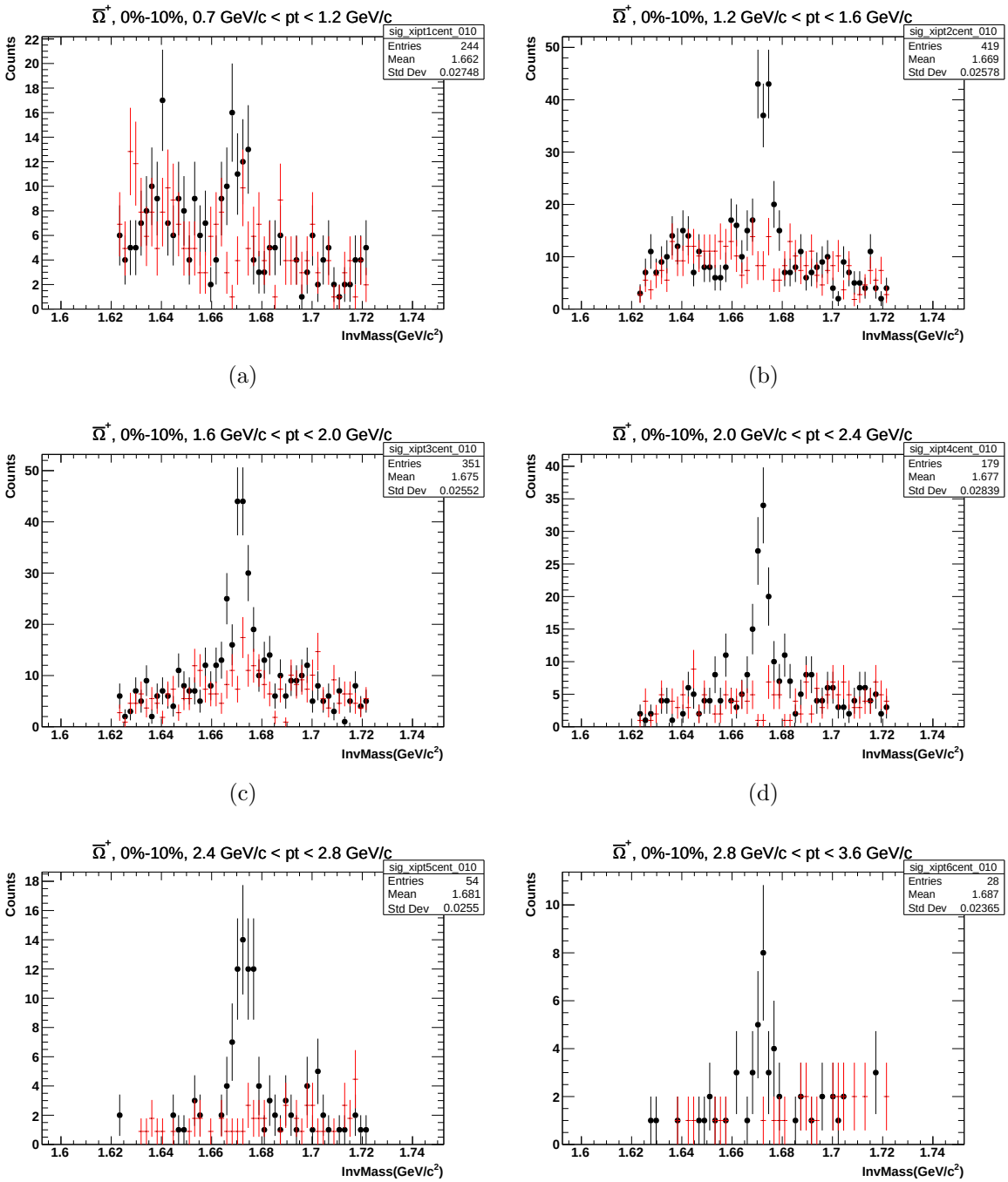

Figure 3.14: (a)-(f) The invariant mass distribution of reconstructed $\bar{\Omega}^+$s in labeled pt bins for $10-60\%$ central Au+Au collisions at $\sqrt{s_{NN}} = 14.5$ GeV. Red markers represent the rotational background normalized within the two side-band windows denoted by magenta dashed lines. The signal is the sum of the counts within the mass window defined by the two blue dashed lines.

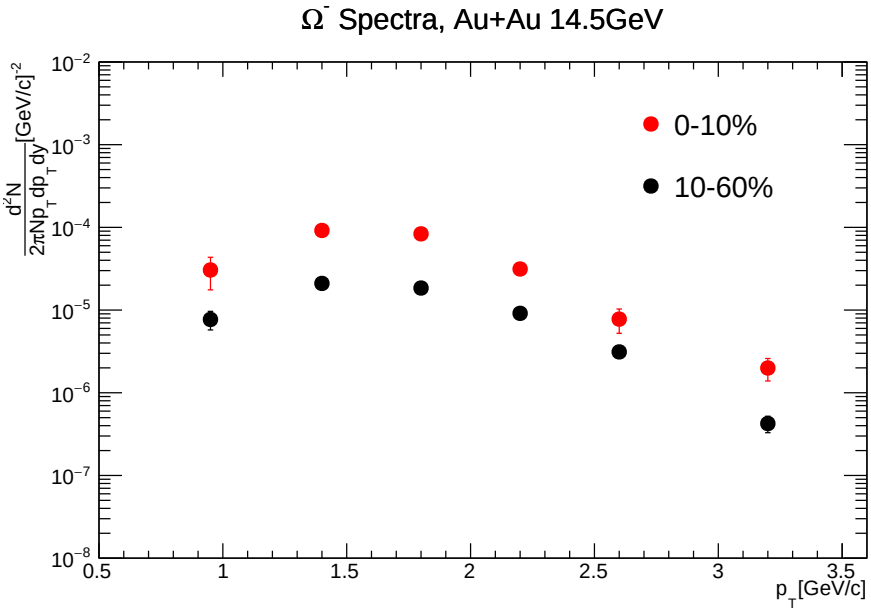

Figure 3.15: Raw spectra for Ω^- in Au+Au collisions at $\sqrt{s_{NN}} = 14.5\text{GeV}/c^2$.

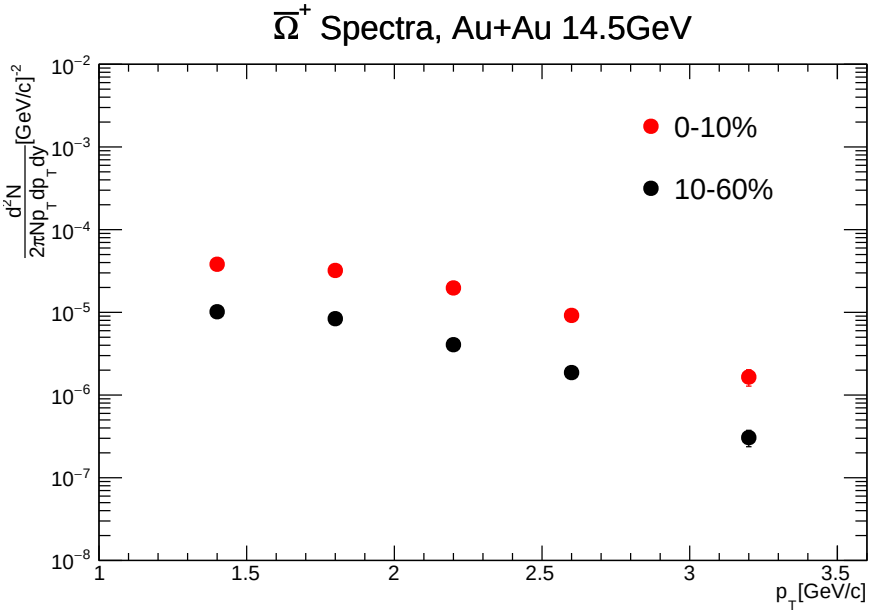

Figure 3.16: Raw spectra for Ω^+ in Au+Au collisions at $\sqrt{s_{NN}} = 14.5\text{GeV}/c^2$.

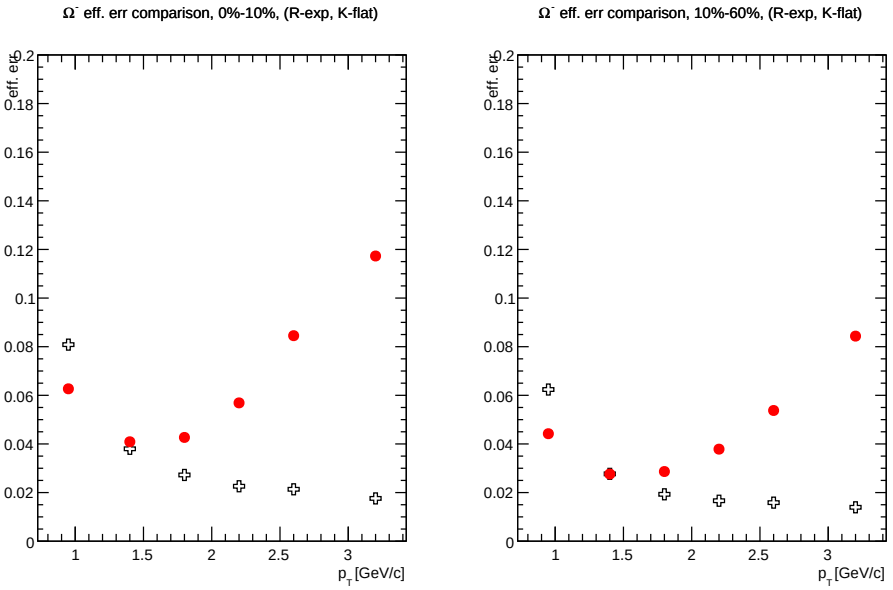

Figure 3.17: Comparison of efficiency error for Ω^-. Black: flat p_T; Red: exponential p_T.

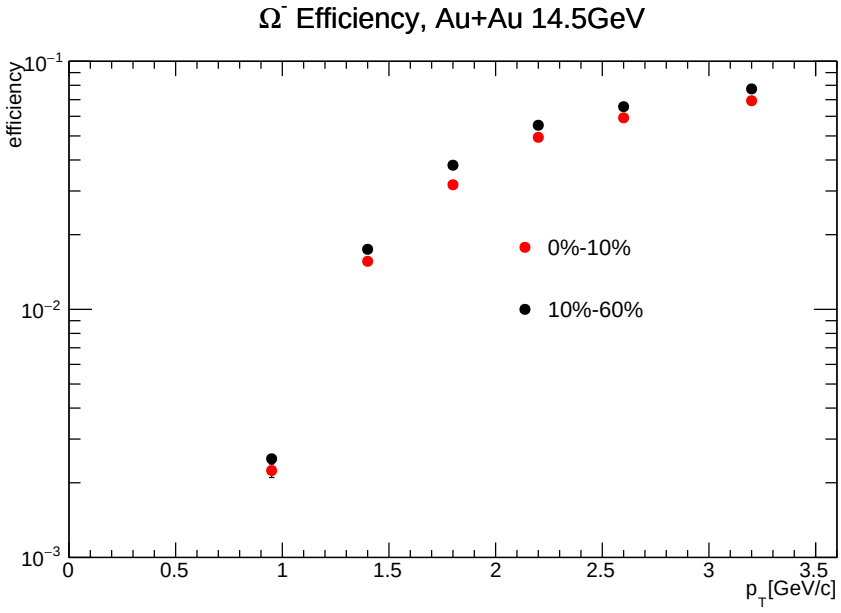

Figure 3.18: Combined efficiency for Ω^- in Au+Au 14.5 GeV.

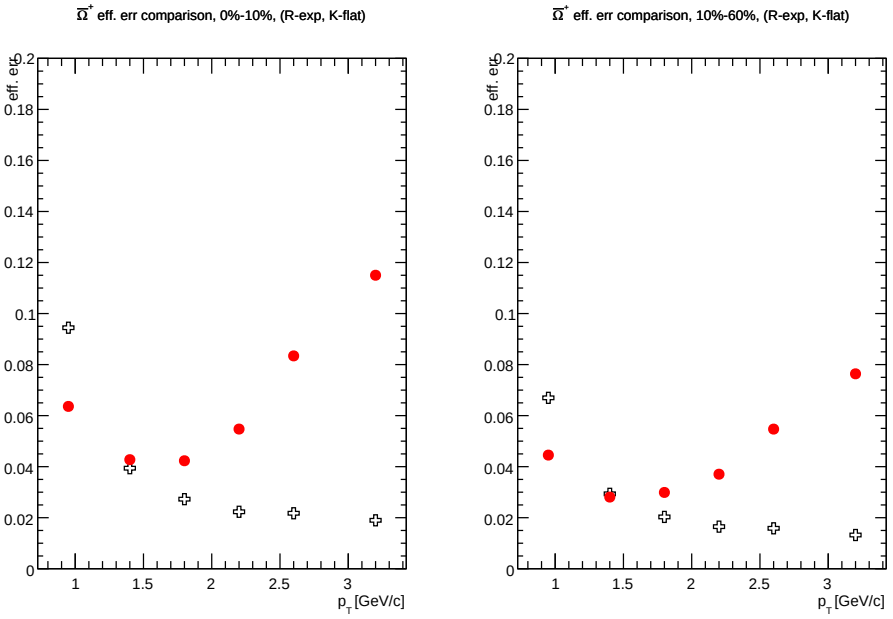

Figure 3.19: Comparison of efficiency error for $\bar{\Omega}^+$. Black: exponential p_T; Red: flat p_T.

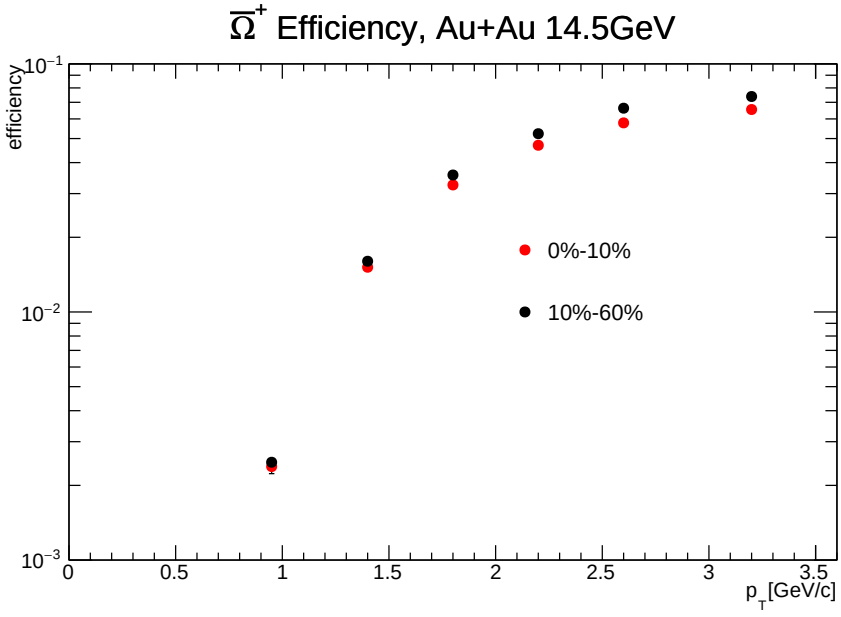

Figure 3.20: Combined efficiency for Ω^- in Au+Au 14.5 GeV.

3.4 ϕ Meson Reconstruction

3.4.1 Reconstruction Cuts

The cuts used to reconstruct ϕ meson signals are listed in Table 3.8. The decay mode we made use of is $\phi \to K^+K^-(BR = (49.2 \pm 0.5)\%, \tau = (1.55 \pm 0.01) \times 10^{-22}s)$ thus topological cuts that we exploited in $\Omega^-(\bar{\Omega}^+)$ study are not applicable, due to its shorter lifetime. The contamination of electrons in kaon samples may introduce significant mis-identified ϕ from e^+e^- pairs. Because the major source of e^+e^- pairs is photon conversion and the dip-angle of the conversion is usually small, it is effective to apply a cut on that quantity to largely remove the contamination. The dip-angle is shown in Figure 3.21 and can be computed as follows:

$$\delta = \cos^{-1}\left(\frac{p_{T,1}p_{T,2} + p_{z,1}p_{z,2}}{p_1 p_2}\right) \tag{3.13}$$

A significant level of background is still expected in the invariant mass distribution of ϕ because of the lack of effective topological cuts. The strategy we take to reconstruct the background shape is called event-mixing, or mixed-events.

Table 3.8: Reconstruction cuts for ϕ meson.

Cuts	Values
# of TPC hits	≥ 15
nHits Fit	≥ 0.52
p_T	≥ 0.15 GeV/c
DCA to primary vertex	≤ 3.0 cm
$\lvert n\sigma_{\text{Kaon}}\rvert$	≤ 2.0
dip-angle cut (see Figure 3.21)	≥ 0.04

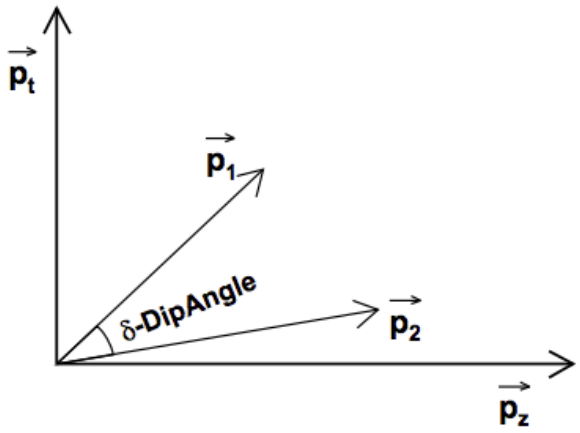

Figure 3.21: Dip angle cut for ϕ meson reconstruction.

3.4.2 Mixed-Event Technique

Given the procedure of reconstructing ϕ mesons by pairing two oppositely charged kaons without strict topological cuts, a high level of combinatorial background exits, especially in central collisions. The mixed-event technique is a useful tool to recover the background correlation while removing the resonance peak.

In mixed-event analysis, an event buffer, as shown in Figure 3.22, is usually used to store the events to mix with.

The entire event buffer is split into cells based on the centrality and vertex z position. As the number of events analyzed increases, the cells in the buffer gradually get populated by events which correspond to the centrality bin and vertex z position of each bin. The size of the cell (M, the maximum number of events to fit in) should be predefined to meet the practical analysis needs in terms of statistical precision.

The "mixing" procedure is basically as follows:

1. When a new event is analyzed, the mixed ϕ mesons are constructed by pairing the kaons in the new event with the opposite signed kaons from the events that are already stored in the same cell;

2. If the cell is not full yet, copy the new event into it. If it is full, swap it with one of the events in the cell randomly.

In detail, when the cell is full, one of the events in the corresponding cell gets swapped with the new incoming event by the following rules (reservoir sampling algorithm [Vit85]):

a. The probability to swap in the new event is M/N, where M is the capacity of the cell and N is the number of events which are qualified for the cell so far;

b. If the new event is picked for swap by step a, any one of the events in the cell gets swapped out with the same probability $1/M$.

This algorithm can guarantee that, without knowing the total number of events (N) falling into the cell beforehand, each event stored in the buffer is randomly selected with probability of M/N. This result can be proved by induction: assuming at any moment (N events so far qualified for this cell), the probability of each event stored in the cell is M/N. If the $(N+1)$th event fits in with a probability of $M/(N+1)$, then each event in the cell gets replaced with probability of $1/(N+1)$, in other words, the probability for it to survive is $N/(N+1)$. In the end, each event surviving the first $N+1$ events stream will be either $M/(N+1)$ (if it is the newest one) or $N/(N+1) \times M/N = M/(N+1)$,

3.4.3 Signal Extraction

To scale the mixed-event background, the counts within a variable range $[a, b]$ is required to match the number from the real data. After subtracting the mixed-event background, we use a function fitting method to extract the counts of ϕ mesons under the invariant mass peak. The function we used to fit the signal peak is a Breit-Wigner plus a first order polynomial. Of course, second-order polynomial could be used if the first-order can't fit well. In this thesis, the variation of background fitting functions is counted as a source of systematic uncertainties.

3.4.4 Reconstruction Efficiencty and Raw Transverse Momentum Spectra of ϕ

As described in Section 3.3.3, two p_T distribution of artificial ϕ mesons are also used for embedding simulations and their corresponding statistical error of efficiency as a function of p_T are shown in Figure 3.25. We take the efficiency data point with smaller stat. err. to

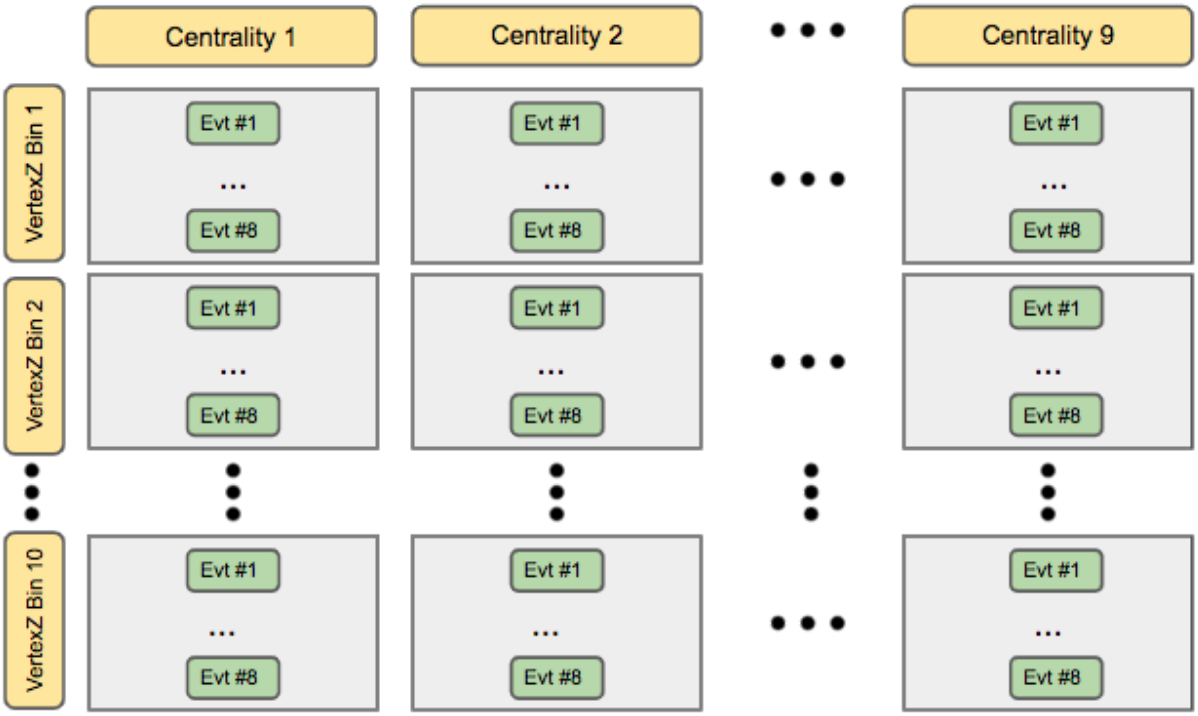

Figure 3.22: Mixed event buffer.

construct the final transverse momentum dependence of ϕ meson reconstruction efficiency for 9 centralities, which is plotted in Figure 3.26. Before the correction, the raw spectra of ϕ mesons in Au+Au collisions at $\sqrt{s_{NN}} = 14.5$ GeV can be found in Figure 3.27

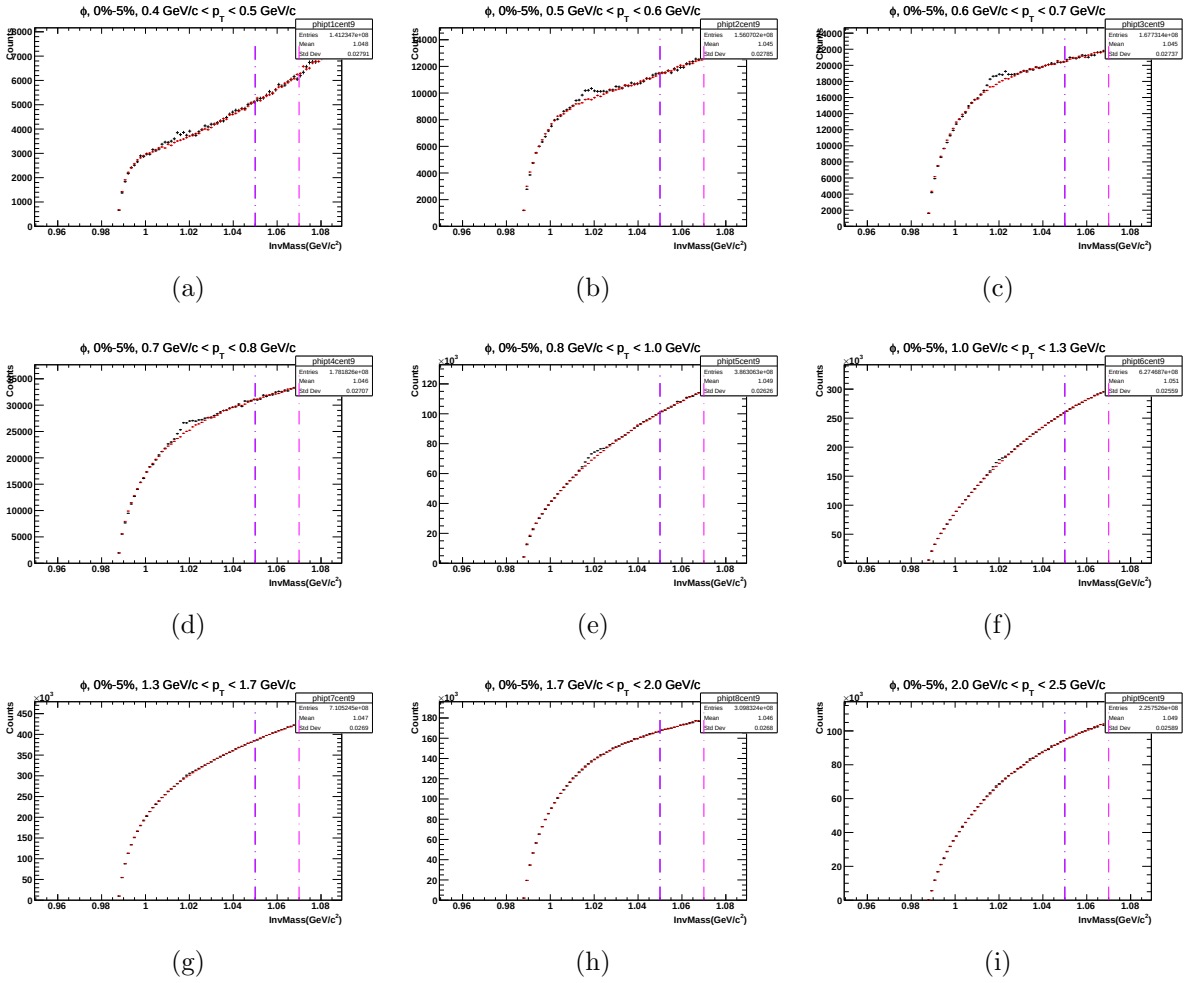

(a) (b) (c)

(d) (e) (f)

(g) (h) (i)

Figure 3.23: (a)-(i) The invariant mass distribution of reconstructed ϕ in labeled pt bins for $0-5\%$ central Au+Au collisions at $\sqrt{s_{NN}} = 14.5$ GeV. Red markers represent the mixed-event background, normalized within the side-band windows denoted by the two vertical dashed lines.

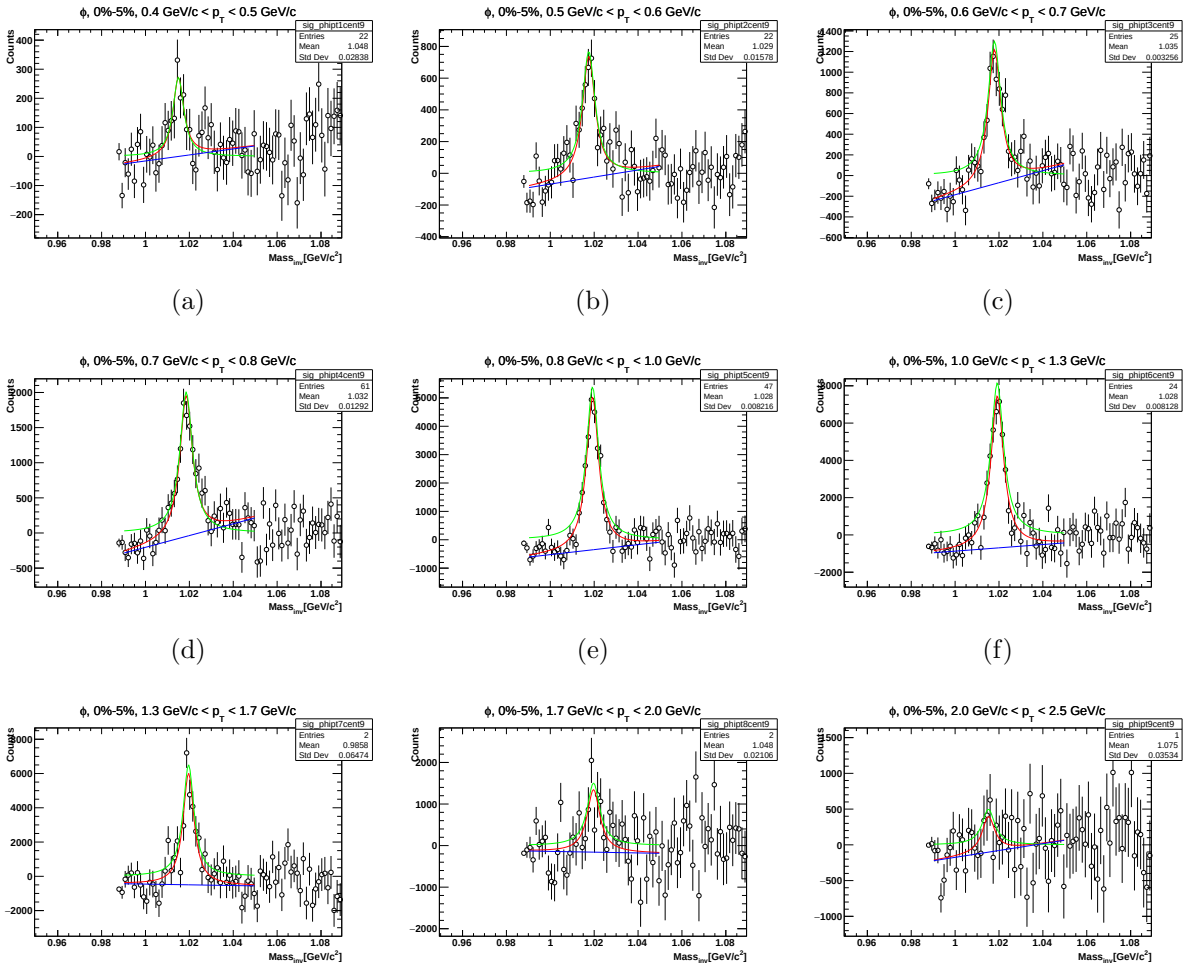

Figure 3.24: (a)-(i) The invariant mass distribution of reconstructed ϕ after subtracting mixed-event background in labeled pt bins for $0-5\%$ central Au+Au collisions at $\sqrt{s_{NN}} =$ 14.5 GeV. Green: the Breit-Wigner function. Blue: the first order polynomial. Red: the sum of green and blue.

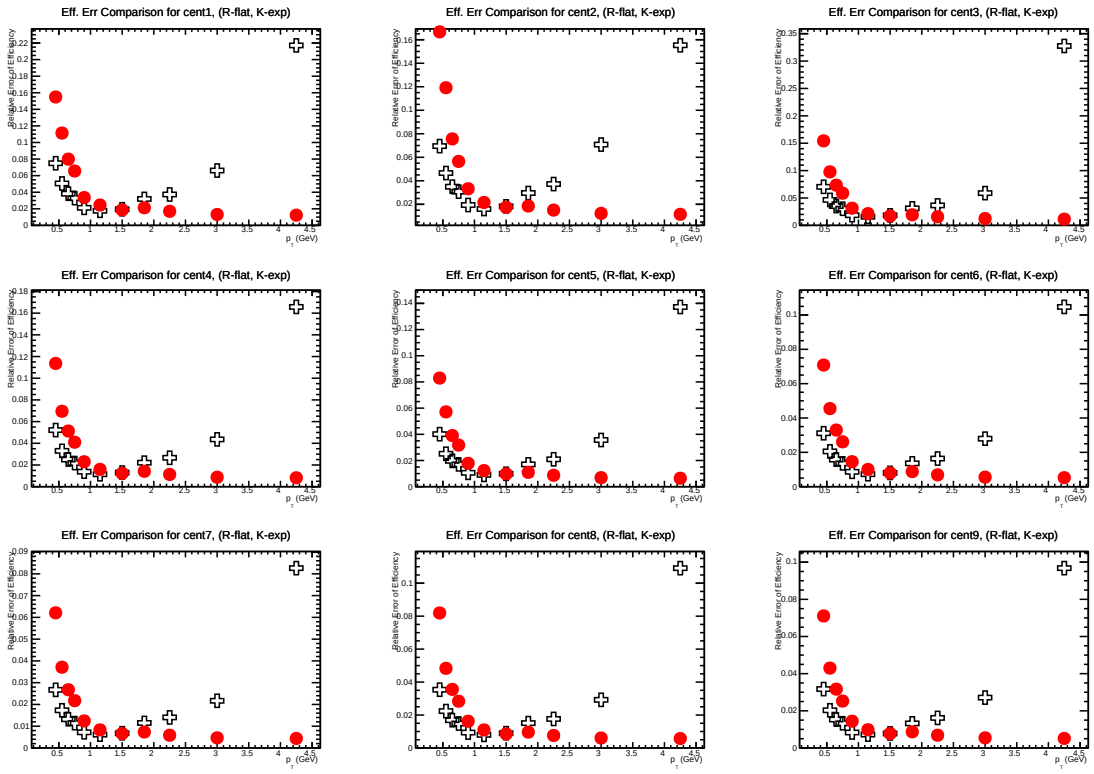

Figure 3.25: Error for ϕ meson reconstruction efficiency. Black: embedding samples with exponential p_T distribution. Red: embedding samples with flat p_T distribution.

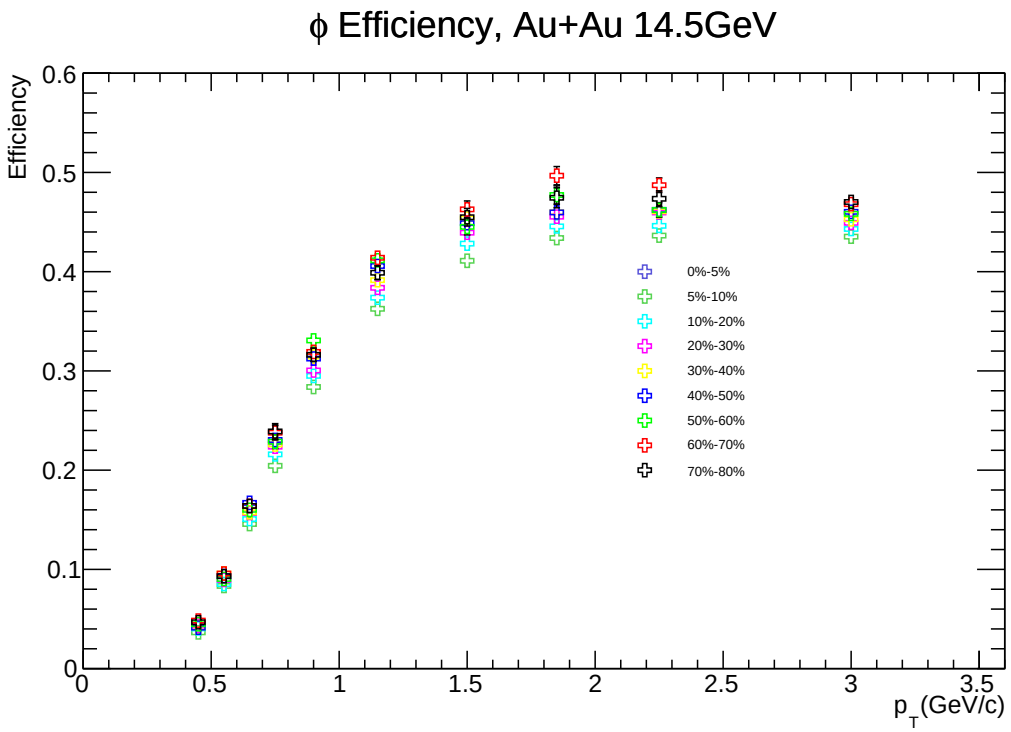

Figure 3.26: Reconstruction efficiency for ϕ mesons in Au+Au collisions at $\sqrt{s_{NN}}$ = 14.5 GeV.

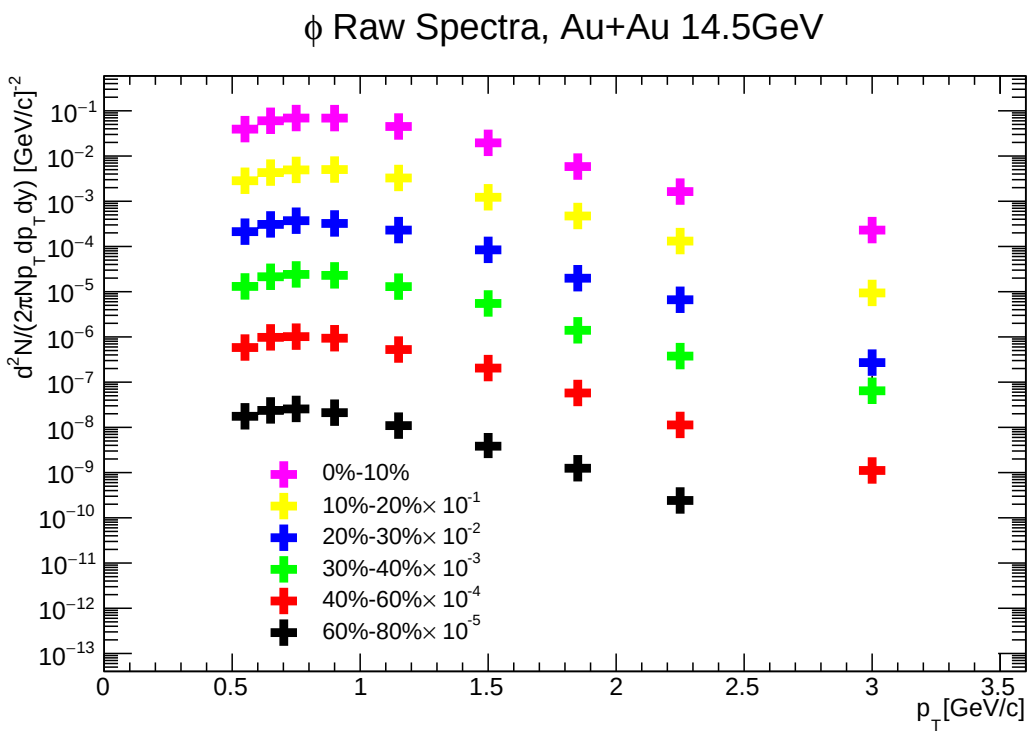

Figure 3.27: Raw spectra of ϕ in Au+Au collisions at $\sqrt{s_{NN}} = 14.5$ GeV.

CHAPTER 4

Identified Particle Correlation

4.1 Data Analysis Strategy

In Ref. [KPT98], possible $\mathcal{P}-$ and $\mathcal{CP}-$ violated chiral effects in high energy heavy ion collisions was proposed for the first time. To hunt for these effects, e.g. CME, several observables, all of which look for non-statistical differences among the reaction planes reconstructed from different groups of particles, either of difference charge or in different kinematic regions, are suggested in the early literature [KPT98, FCL$^+$01, Vol00]. However, no deviation from the expectation for these observables has yet been found. Another possibility for detecting the CME effect is to exploit the preferential emission direction of charged pions after collisions [Vol04a, Kha06]. The essence of the idea is, given the existence of parity violation interactions, an asymmetry of charged pion production along the direction of the system angular momentum should occur and the magnitude could be as high as one percent in mid-central Au+Au collisions at RHIC. An exaggerated diagram showing this effect can be found in Fig. 4.1. However, the orientation of the asymmetry varies event-by-event (positive pions are not necessarily going along the magnetic field direction as the Fig. 4.1 shows), so if by taking the average of event-wise measurements of the asymmetry over large samples, the result would end up being zero. However, a correlation measurement could be used to uncover the underlying tiny asymmetry due to the parity violation effect. A detailed description of the method can be found, below. The charged pion production asymmetry can be parameterized as follows:

$$dN/d\phi \propto (1 + 2a\sin(\phi)) \tag{4.1}$$

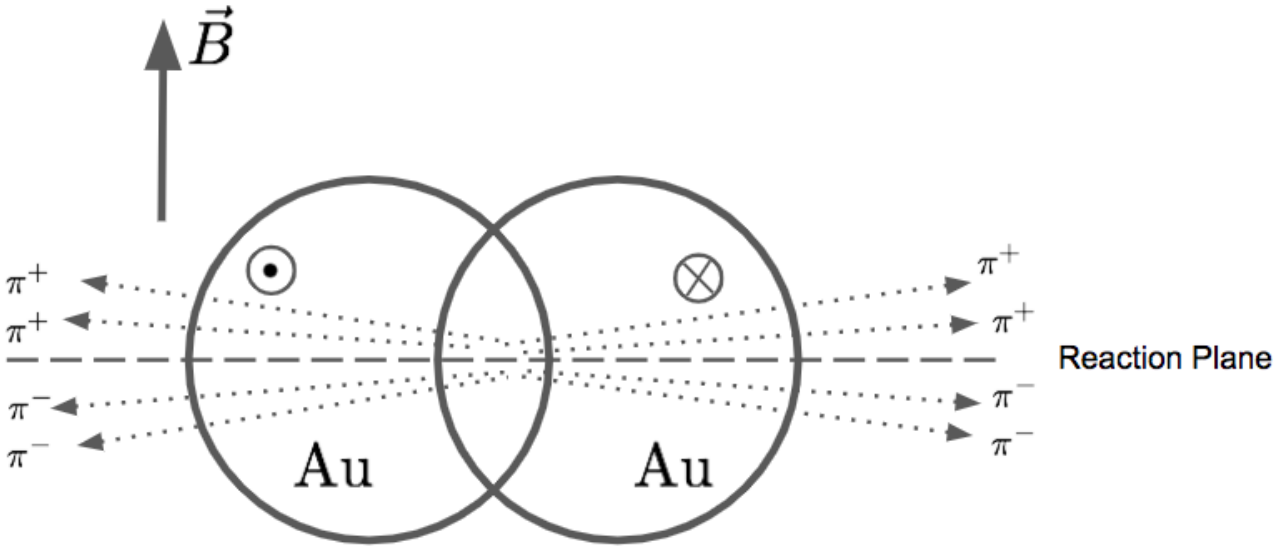

Figure 4.1: An exaggerated diagram showing the preferential emission direction of pions in non-central Au+Au collisions.

where ϕ is the particle emission azimuthal angle with respect to the reaction plane. The parameter a can be directly connected to the pion production asymmetry via $A_{\pi^+} = \pi a/4 \approx Q/N_{\pi^+}$ [Kha06], where Q the topological charge ($Q \geq 1$) and N_{π^+} the positively charged pion multiplicity over about one unit of rapidity. Let us consider an azimuthal angle correlation between two particles (a, b):

$$\langle\cos(\phi_a + \phi_b - 2\Psi_2)\rangle \tag{4.2}$$

$$= \langle\cos(\phi_a + \phi_b - 2\Psi_{\rm RP} + 2\Psi_{\rm RP} - 2\Psi_2)\rangle \tag{4.3}$$

$$= \langle\cos(\phi_a - \Psi_{\rm RP})\cos(\phi_b - \Psi_{\rm RP}) - \sin(\phi_a - \Psi_{\rm RP})\sin(\phi_b - \Psi_{\rm RP})\rangle \tag{4.4}$$

$$(\langle\cos(2\Psi_{\rm RP} - 2\Psi_2)\rangle - \sin(2\Psi_{\rm RP} - 2\Psi_2)) \tag{4.5}$$

$$=(\langle\cos(\phi_a - \Psi_{\rm RP})\rangle\langle\cos(\phi_b - \Psi_{\rm RP})\rangle - \langle\sin(\phi_a - \Psi_{\rm RP})\rangle\langle\sin(\phi_b - \Psi_{\rm RP})\rangle)\langle\cos(2\Psi_{\rm RP} - 2\Psi_2)\rangle \tag{4.6}$$

$$=(v_{1,a}v_{1,b} - a_a a_b)\langle\cos(2\Psi_{\rm RP} - 2\Psi_2)\rangle \tag{4.7}$$

Ψ_2 is the second order event plane [PV98] and $\Psi_{\rm RP}$ is the true reaction plane. The term $\langle\sin(2\Psi_{\rm RP} - 2\Psi_2)\rangle$ vanishes due to the symmetry of the reconstructed second order event plane orientation with respect to the true reaction plane and the term of $\langle\cos(2\Psi_{\rm RP} - 2\Psi_2)\rangle$

is the so-called reaction plane resolution. The equality sign between Eq. 4.6 and Eq. 4.7 holds only approximately. $v_{1,*}$ are the terms representing the direct flow of the particles and a_* are the asymmetry parameter mentioned above. The brackets require the quantity be calculated as the average over all of the events. We define the γ_{112} observable by rearranging Eq. 4.2:

$$\gamma_{112} = \langle \cos(\phi_a + \phi_b - 2\Psi_2) \rangle \,/\, \langle \cos(2\Psi_{\rm RP} - 2\Psi_2) \rangle = (v_{1,a} v_{1,b} - a_a a_b) \tag{4.8}$$

If v_1 for particles a, b are equal to zero, the Eq. 4.8 can be directly used to measure the particle production asymmetry. Actually, this condition can be achieved by studying the correlation in the rapidity region which is symmetric about mid-rapidity, where the average directed flow goes to zero. In practice, a more convenient way to probe this effect is to make a comparison between opposite sign and same sign correlations. That is, if charge production asymmetry across the reaction plane exists, a measurement of same sign pion pair correlation ($\pi^+\pi^+$ or $\pi^-\pi^-$) is expected to yield a lower value (because the "$-a_a a_b$" term in Eq. 4.8 is negative) than the opposite sign correlation of $\pi^+\pi^-$ pairs (the "$-a_a a_b$" term in Eq. 4.8 is positive).

4.1.1 Event Plane Orientation Estimation

4.1.1.1 Algorithm

The approach we take to estimate the second order event plane is using the sizable elliptical flow [PV98] in Au+Au collisions. The event flow vector Q_n is defined below as:

$$Q_n \cos(n\Psi_n) = \sum_i w_i \cos(n\phi_i) \tag{4.9}$$

$$Q_n \sin(n\Psi_n) = \sum_i w_i \sin(n\phi_i) \tag{4.10}$$

where i goes through all of the particles used for event plane reconstruction in the event and w_i is the assigned weight (transverse momentum pT in this analysis) for the corresponding track. So, the nth order event plane angle Ψ_n can be solved as follows:

$$\Psi_n = \left(\tan^{-1} \frac{\sum_i w_i \sin(n\phi_i)}{\sum_i w_i \cos(n\phi_i)} \right) / n \tag{4.11}$$

The value of Ψ_n lies within $[0, 2\pi/n)$.

4.1.1.2 Detector Acceptance Correction

The finite acceptance of detector system (for example, due to the dead area between STAR TPC end-cap sections) might introduce an azimuthal anisotropy of particles, which usually results in unflatten distribution of reconstructed event plane orientations. To eliminate this artificial effect, a few different approaches are proposed. One of them, which uses the Fourier coefficients of the event plane distribution to do event-by-event shifting, will be explained below. It is also the method employed in the identified particle correlation measurement presented in later sections.

We can expand the unflatten distribution of the second order event plane orientation as:

$$\frac{dN}{d\psi} = \frac{a_0}{2} + \sum_{n=2,4...} (a_n \cos n\psi + b_n \sin n\psi), \psi \in [0, \pi) \tag{4.12}$$

$$a_0 = \frac{2N_{\text{events}}}{\pi} \tag{4.13}$$

$$a_n = \frac{2N_{\text{events}}}{\pi} \int \frac{dN}{d\psi} \cos n\psi d\psi \cdot \frac{1}{N_{\text{events}}} = a_0 \langle \cos n\psi \rangle, n = 2, 4, ... \tag{4.14}$$

$$b_n = \frac{2N_{\text{events}}}{\pi} \int \frac{dN}{d\psi} \sin n\psi d\psi \cdot \frac{1}{N_{\text{events}}} = a_0 \langle \sin n\psi \rangle, n = 2, 4, ... \tag{4.15}$$

Now our goal is to find an equation that shifts the raw ψ to ψ', so that:

$$\frac{dN}{d\psi'} = \frac{dN}{d\psi}\frac{d\psi}{d\psi'} = a_0/2 \tag{4.16}$$

Thus we can get a differential equation and solve it as below:

$$d\psi'/d\psi = 1 + \sum_{n=2,4...} \frac{2}{n}(a_n/a_0 \cos n\psi + b_n/a_0 \sin n\psi) \tag{4.17}$$

$$\psi' = \psi + \sum_{n=2,4...} \frac{2}{n}(\langle \cos n\psi \rangle \sin n\psi - \langle \sin n\psi \rangle \cos n\psi) \tag{4.18}$$

Eq. 4.18 is what we need to eliminate the un-flatness of the reconstructed event plane orientation. In this analysis, we corrected the event plane up to $8th$ order, which produces a quite even distribution of Ψ_2. An example showing the effect of event plane correction can be found in Fig. 4.2

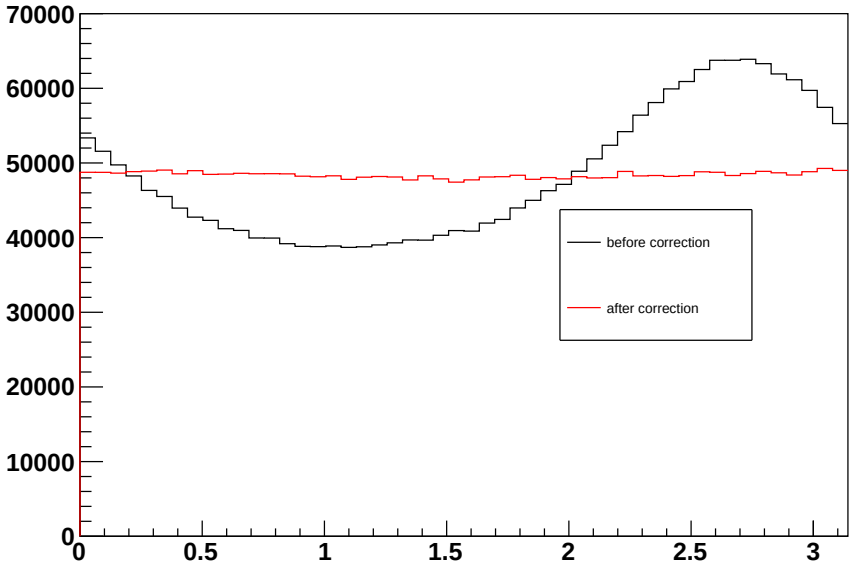

Figure 4.2: Event plane orientation distribution before and after flatness correction.

4.1.2 Event Plane Resolution

To measure γ_{112} using Eq. 4.8, the event plane resolution term $\langle\cos(2\Psi_r - 2\Psi_2)\rangle$ (we use Ψ_r interchangeably with Ψ_{RP} in the following text) has to be determined. The "event plane resolution" is a measure to quantify the spread of the reconstructed event plane around the true reaction plane, which means if the reconstruction is more precise, the value of the event resolution is closer to unity, because $(\Psi_r - \Psi_2) \to 0$.

As pointed out by Ref. [PV98], an analytical evaluation of event plane resolution exists. To get the final result, we can start off writing down the distribution of $m(\Psi_m - \Psi_{\mathrm{r}})$:

$$\frac{dP}{d[m(\Psi_m - \Psi_r)]} = \int \frac{v'_m dv'_m}{2\pi\sigma^2} \times \exp\left(-\frac{v_m^2 + v_m'^2 - 2v_m v'_m \cos[m(\Psi_m - \Psi_{\mathrm{RP}})]}{2\sigma^2}\right) \quad (4.19)$$

Where $\sigma^2 = \frac{\langle w^2\rangle}{2N\langle w\rangle^2}$, If we define $\chi_m = v_m/\sigma$, then the event plane resolution is

$$\langle\cos[km(\Psi_m - \Psi_r)]\rangle = \frac{\sqrt{\pi}}{2\sqrt{2}}\chi_m \exp(-\chi_m^2/4) \times [I_{(k-1)/2}(\chi_m^2/4) + I_{(k+1)/2}(\chi_m^2/4)] \quad (4.20)$$

This solution shows how the mth harmonic is used to determine the $n = km$th order event plane resolution, which is plotted in Fig. 4.3. However, Eq. 4.20 is not sufficient to evaluate $\langle\cos[km(\Psi_m - \Psi_r)]\rangle$ in practice, since we do not know v_m beforehand. The cyclic dependence between harmonic flow and the corresponding event plane resolution can be cleverly broken by exploiting the correlation between flow angles of independent sets of particles.

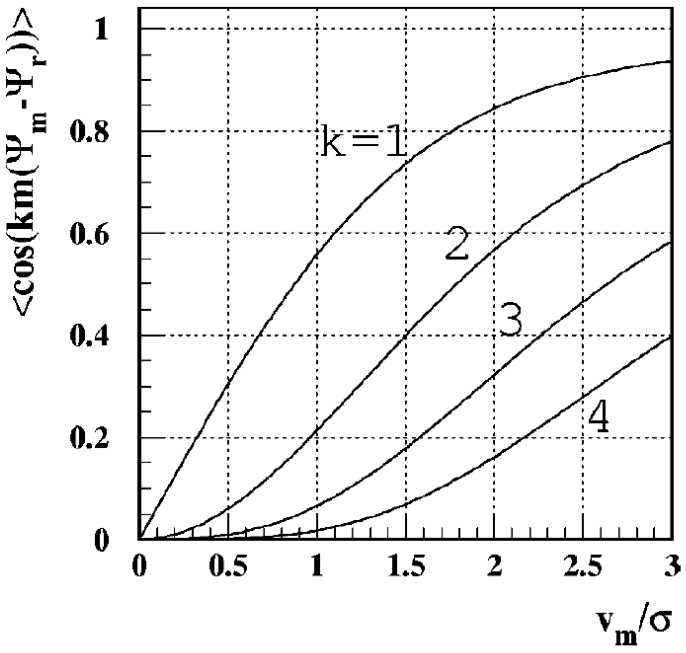

Figure 4.3: The event plane resolution for the nth harmonic of the particle distribution with respect to the mth harmonic plane, as a function of $\chi_m = v_m/\sigma$.

Supposing the particles used to reconstruct the full event plane are divided into two sub-events a, b (randomly or based on the rapidity range), the correlation between the event planes reconstructed from these two is:

$$\begin{aligned}
\left\langle\cos[n(\Psi_m^a - \Psi_m^b)]\right\rangle &= \left\langle\cos[n(\Psi_m^a - \Psi_r + \Psi_r - \Psi_m^b)]\right\rangle && (4.21)\\
&= \left\langle\cos[n(\Psi_m^a - \Psi_r)]\cos[n(\Psi_m^b - \Psi_r)]\right\rangle \\
&\quad + \left\langle\sin[n(\Psi_m^a - \Psi_r)]\sin[n(\Psi_m^b - \Psi_r)]\right\rangle && (4.22)\\
&= \left\langle\cos[n(\Psi_m^a - \Psi_r)]\right\rangle\left\langle\cos[n(\Psi_m^b - \Psi_r)]\right\rangle && (4.23)
\end{aligned}$$

So if there is no correlation between these two sub-events other than flow and these two

sub-events have equal multiplicity, then we have the following relation to obtain sub-event plane resolution (taking the second order event plane as an example):

$$\langle \cos[2(\Psi_2^a - \Psi_r)] \rangle = \sqrt{\left\langle \cos[2(\Psi_2^a - \Psi_2^b)] \right\rangle} \tag{4.24}$$

Given this data-driven method to compute sub-event plane resolution, Eq. 4.20 can be taken advantage of to determine the full event plane resolution. Since the independent variable χ_m/σ is proportional to $\sqrt{N}$, then the χ_m/σ for full event should be $\sqrt{2}$ bigger than the sub-event. For low value of event plane resolution, a linear approximation is close to the true functional relationship between x, y quantities presented in Fig. 4.3, thus we have the following result:

$$\left\langle \cos[2(\Psi_2^{\text{full}} - \Psi_r)] \right\rangle = \sqrt{2} \left\langle \cos[2(\Psi_2^{\text{half}} - \Psi_r)] \right\rangle \tag{4.25}$$

which enables us to use the sub-event plane to compute the full event plane resolution.

4.1.3 Correlation Measurement

With the event plane orientation being determined, the remaining procedures to compute the γ_{112} correlator becomes straight-forward. The diagram below, taking Λp correlation as the example, shows a flexible and convenient software framework built for this type of event-plane related two particle azimuthal angle correlation measurement. The functionality of each module is described as follows:

- StPhiWeightMaker: This module of code interfaces with MuDst data (the data structure used by STAR to store the collision data) directly and should be executed first to obtain the raw azimuthal angle ϕ distribution for the particles of interest. In this example, the ϕ distribution of Λ, p (used for the correlation study), and charged primary hadrons (used for event plane reconstruction) are recorded for each event. In practice, a fine correction of azimuthal angle for particles in different rapidity, primary vertex z position, and electric charge categories is essential for an accurate azimuthal angle correlation analysis, thus histograms of the ϕ distribution produced by this module will be as many as the number of categories for each type of track, e.g., (Λ, p, and

charged primary tracks). Meanwhile, the Fourier coefficients for the azimuthal angle correction Eq. 4.18, $\langle \cos n\phi \rangle$ and $\langle \sin n\phi \rangle$, can also be measured here for future use (see StGammaMaker).

- StEpWeightMaker: In this module, the raw sub-event planes are reconstructed using primary tracks (after taking out the p's and daughters of Λ's) and the Fourier coefficients in Eq. 4.18 will be also recorded for future correction use. The w_i in Eqs. 4.9 and Eq. 4.10, which are used to determine the event plane orientation, is taken from the value of the multiplication of p_T and the weight of the corresponding azimuthal angle ϕ that is based on the raw distribution of ϕ obtained from StPhiWeightMaker.

- StEpResolMaker: This module produces the full event plane resolution that is used in final γ_{112} correction. It is taking in the correction terms from StEpWeight and flatten the full event plane orientation distribution.

- StGammaMaker: In this piece of code, the final result of γ_{112} correlator is computed with corrected azimuthal angles for p's, Λ's and event plane orientations. The correction terms, for either p, Λ or the event plane, are all taken from the output of previous modules. After these quantities are computed, this framework can be easily extended to measure a lot of other azimuthal angle correlations, such as δ or γ_{123}...

This set of software can be compiled and run in parallel on the BNL rcf cluster, and the total time to run the entire analysis cycle for 15M events (e.g., Au+Au 27 GeV in Run 11) is only one day, which makes fast experimentation with fine-tuning and checks of the analysis convenient and plausible.

4.1.4 Flow Normalized "γ_{112}", κ_{112} Correlator

The flow-related background is known to contribute to the γ_{112} correlation. To quantitatively estimate the flow background, a background model for γ_{112} and the two-particle correlator $\delta \equiv \langle \cos(\phi_a - \phi_b) \rangle$ has been proposed and a pure signal correlator H has been introduced in

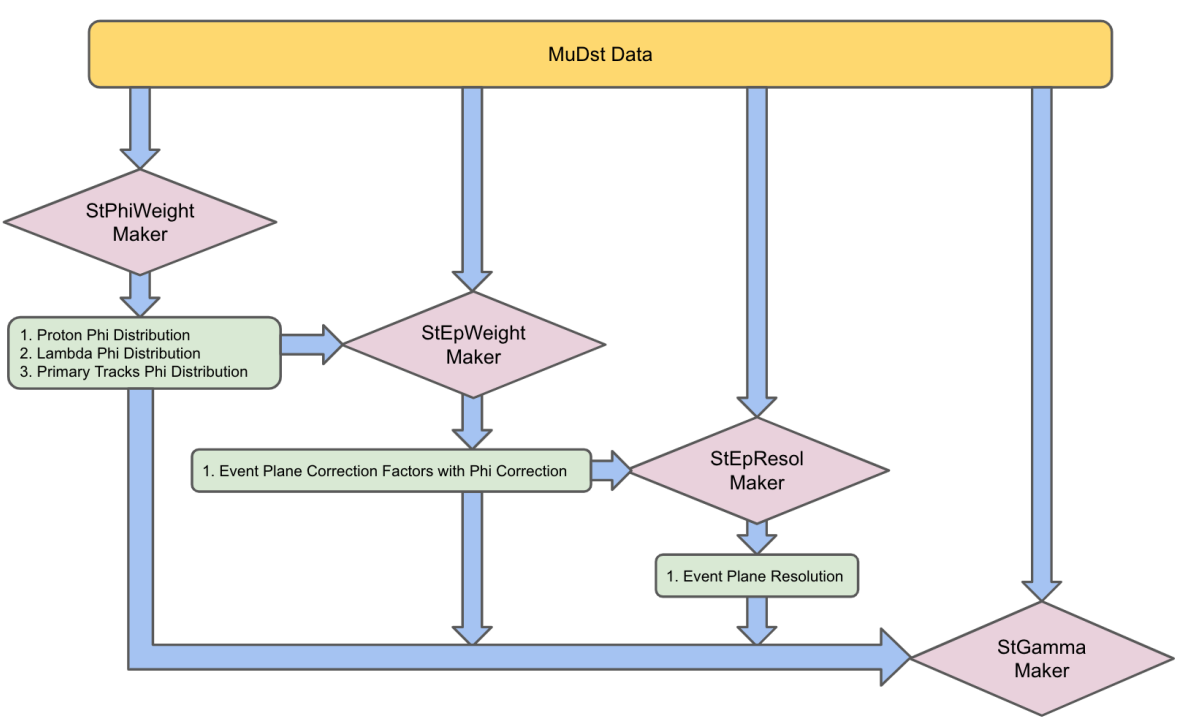

Figure 4.4: Analysis procedures for γ_{112} correlation measurement.

Ref. [BKL13]:

$$\Delta\delta \equiv \langle \cos(\phi_a - \phi_b) \rangle_{\text{OS-SS}} = \Delta F + \Delta H \tag{4.26}$$

$$\Delta\gamma_{112} \equiv \langle \cos(\phi_a + \phi_b - 2\Psi_2) \rangle_{\text{OS-SS}} = \kappa v_2 \Delta F - \Delta H \tag{4.27}$$

where H denotes the charge separation due to chiral effects. "Δ" refers to the difference between "opposite-sign" and "same-sign" correlation. κ quantifies the coupling between v_2 and δ, which contaminates the γ_{112} measurement:

$$\kappa = \frac{\Delta\gamma_{112} + \Delta H}{v_2(\Delta\delta - \Delta H)} \tag{4.28}$$

We introduce a new quantity or new observable κ_{112} by setting ΔH to be zero for a maximum background scenario:

$$\kappa_{112} = \frac{\Delta\gamma_{112}}{v_2 \Delta\delta} \tag{4.29}$$

Thus we can compare the κ_{112} from the data to the one from background models such as AMPT simulations. Any excess of measured κ_{112} for particle pairs of interest over the

expected range from background models could indicate the presence of physics beyond the known background, e.g., the CME/CVE. In Chapter 5, the measurement of κ_{112}, along with AMPT simulations for identified particle pairs will be presented.

A simplistic example that can demonstrate the advantage of H correlator (given κ is known to be unity [BKL13]) for charge separation detection is given in Fig. 4.5. In this example, various background mechanisms are presented: flow, momentum conservation, local charge conservation, and resonance decay. If we compute the δ, γ_{112} and elliptic flow v_2 for this case, we can easily get:

$$\gamma_{112,\mathrm{SS}} = -1.0,\ \gamma_{112,\mathrm{OS}} = 0 \Rightarrow \Delta\gamma_{112} = 1.0 \tag{4.30}$$

$$\delta_{\mathrm{SS}} = -1.0,\ \delta_{\mathrm{OS}} = 0 \Rightarrow \Delta\delta = 1.0 \tag{4.31}$$

$$v_2 = 1.0 \tag{4.32}$$

Thus the H correlation becomes:

$$H = \frac{\kappa v_2 \delta - \gamma}{1 + \kappa v_2} \tag{4.33}$$

$$H_{\mathrm{SS}}^{\kappa=1.0} = 0, H_{\mathrm{OS}}^{\kappa=1.0} = 0 \tag{4.34}$$

$$\Delta H = H_{\mathrm{SS}} - H_{\mathrm{OS}} = 0 \tag{4.35}$$

From the simple calculation presented above, we find, given that $\kappa = 1.0$ (based on Ref. [BKL13], κ is estimated to be near unity), ΔH result correctly reflects the input separation while sizable $\Delta\gamma_{112}$ still contains contamination from the other trivial physics mechanisms.

4.2 Data Set and Cuts

4.2.1 Search for CME using Identified Particles

The data set we used to search for CME with identified particle correlation is Run11 AuAu 200 GeV and Run10 AuAu 39 GeV collisions, where the latter served as a cross-check of the top energy result. The minimum bias triggered data (Table 4.1 and Table 4.2) was selected, and around 200M good events were left after applying very basic event-wise cuts for 200

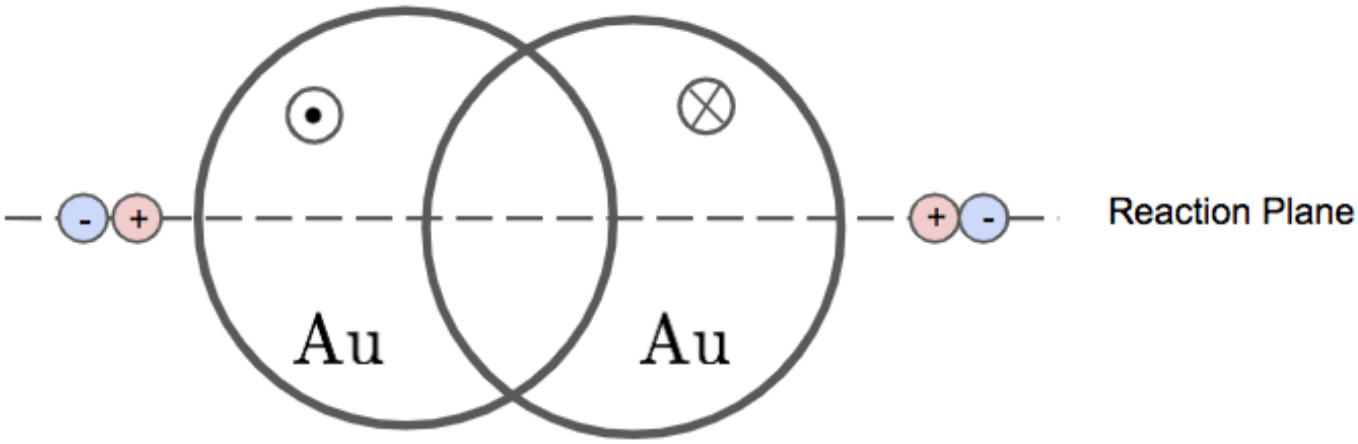

Figure 4.5: A simplistic example demonstrating H could be a better observable to probe charge separation across the event plane. The left (right) gold nucleus is going out of (into) the plane of the paper. Blue and red circles represent positively and negatively charged particles emitted within the event plane in pairs, exaggerating the flow, local charge conservation or resonance decay effects.

GeV collisions and M for 39 GeV. The event, track, and particle identification cuts applied throughout the analysis are presented in Table 4.3, Table 4.4, and Table 4.5

Table 4.1: Used Triggers in Run11 Au+Au Collisions at $\sqrt{s_{NN}} = 200$ GeV

Trigger Label	Offline Trigger ID
vpd-zdc-mb-protected	350003
vpd-zdc-mb-protected	350013
vpd-zdc-mb-protected	350023
vpd-zdc-mb-protected	350033
vpd-zdc-mb-protected	350043

Table 4.2: Used Triggers in Run10 Au+Au Collisions at $\sqrt{s_{NN}} = 39$ GeV

Trigger Label	Offline Trigger ID
mb	1
mb	280001

Table 4.3: Event Cuts in Analyses for Au+Au Collisions at $\sqrt{s_{NN}} = 39, 200$ GeV

Cuts	Values
Primary Vertex Z	$[-50.0, 50.0]$ cm
Primary Vertex R	$[0.0, 2.0]$ cm

Table 4.4: Track Cuts in Analyses for Au+Au Collisions at $\sqrt{s_{NN}} = 39, 200$ GeV

Cuts	Values
Track Flag	$>= 0$
# of TPC Hits	> 15
TPC Hits Ratio	> 0.52
Pseudo-rapidity	$[-1.0, 1.0]$
Transverse Momentum	$[0.2, 2.0]$ GeV/c
DCA to Primary Vertex	< 2.0 cm

4.2.2 Search for CVE using AuAu 27 GeV Collisions

Λp correlation is used to search for CVE induced baryon number separation across the reaction plane in heavy-ion collisions. The reconstruction of Λ hyperons is using topological cuts shown in Table. 4.6. The reconstructed invariant mass spectrum can be found in Fig. 4.6. When reconstructing the event plane using primary tracks, those used as the Λ candidate's daughter should be eliminated from the pool. Meanwhile, the protons used for the correlation computation should also be discarded, otherwise, a huge self-correlation will be introduced.

Table 4.5: Particle Identification Cuts in Analyses for Au+Au Collisions at $\sqrt{s_{NN}} = 39,200$ GeV

Cuts	Values
$N\sigma$ (π, K, p)	[-2.0, 2.0]
M^2 for π	[-0.1, 0.1]
M^2 for p	[0.8, 1.0]
M^2 for K	[0.16, 0.36]

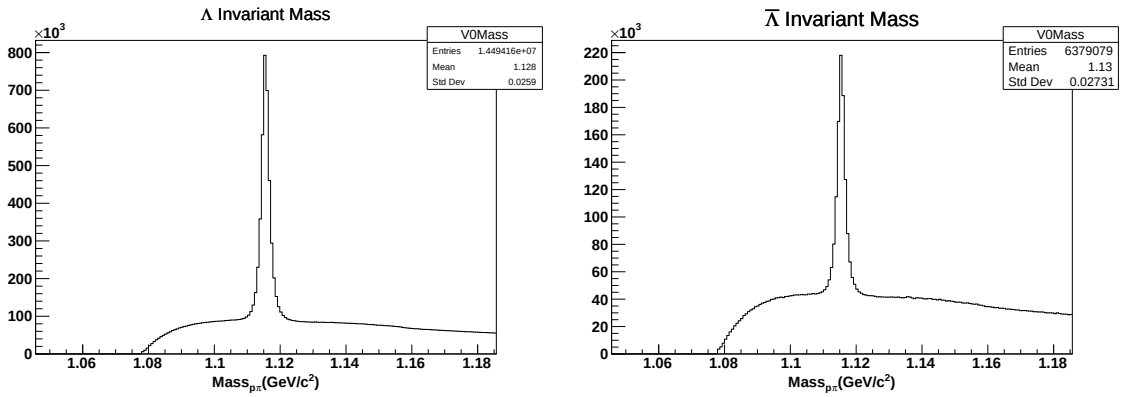

(a) (b)

Figure 4.6: Invariant mass distribution of reconstructed Λ and $\bar{\Lambda}$ in Au+Au collisions at $\sqrt{s_{NN}} = 27$ GeV.

Table 4.6: $\Lambda(\bar{\Lambda})$ Reconstruction Cuts

Cuts	Values
TPC Track NHits	> 15
TPC Track NHits Ratio	> 0.52
$N\sigma$ for Proton	$[-3.0, 3.0]$
$N\sigma$ for Pion	$[-3.0, 3.0]$
Decay Length	> 6.0 cm
Dca for Proton	> 0.6 cm
Dca for Pion	> 1.8 cm
Dca from Proton to Pion	< 0.7 cm
Invariant Mass of Λ	$[1.111683, 1.119683]$ GeV/c^2

CHAPTER 5

Results and Discussions

5.1 $\Omega^-(\bar{\Omega}^+)$ Hyperon and ϕ meson production in AuAu 14.5 GeV Collisions

5.1.1 Transverse Momentum Spectra and Mid-Rapidity Yields

After correcting the raw spectra of $\Omega^-(\bar{\Omega})^+$ (Fig. 3.15 and Fig. 3.16) and ϕ (Fig. 3.27) with the particle reconstruction efficiency (Ω^-: Fig. 3.18; $\bar{\Omega}^+$: Fig. 3.20; ϕ: Fig. 3.26), the p_T dependence of invariant yield of $\Omega^-(\bar{\Omega}^+)$ and ϕ can be obtained, which are shown in Fig. 5.1 (Fig. 5.2) and Fig. 5.3. The Levy function (Eq. 3.10) is used to fit the data. Since measurements cannot reach the full p_T range, dN/dy in the unmeasured portions of the range can be computed by integrating the fitted function over the desired transverse momentum domain. In addition, by using the function value at any p_T, it is also possible to calculate the particle production ratio (e.g. Ω/ϕ), even if the original p_T bins of the particles in interest do not match.

Using this method, the mid-rapidity production of $\Omega^-(\bar{\Omega}^+)$ and ϕ are summarized in Table. A.11, Table. A.12 and Table. A.13. Fig. 5.4 plots the energy dependence of mid-rapidity ϕ meson production in central Au+Au collisions at BES-I energies, along with results from central Pb+Pb collisions at NA49 [A$^+$08]. Within error bars, STAR results are consistent with NA49.

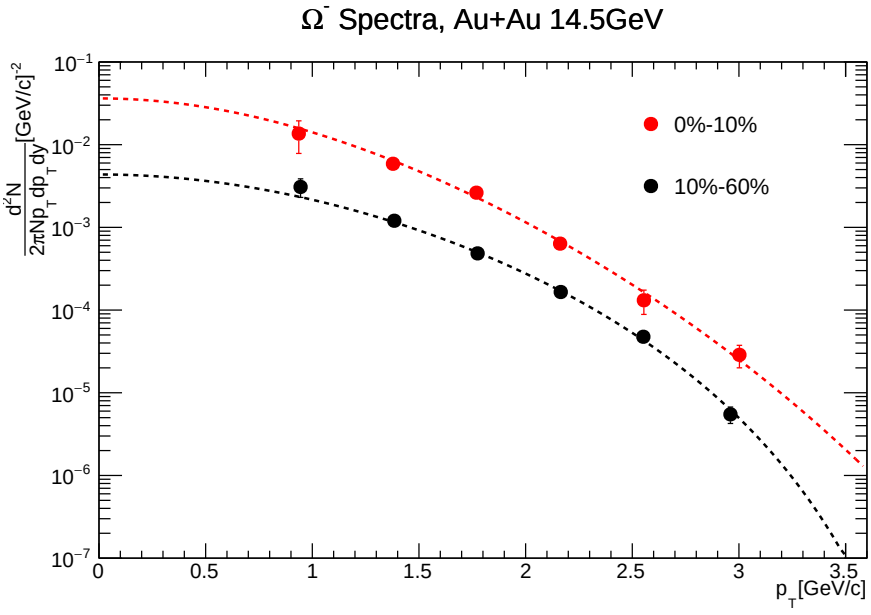

Figure 5.1: Corrected spectra of Ω^- in Au+Au collisions at $\sqrt{s_{NN}} = 14.5$ GeV.

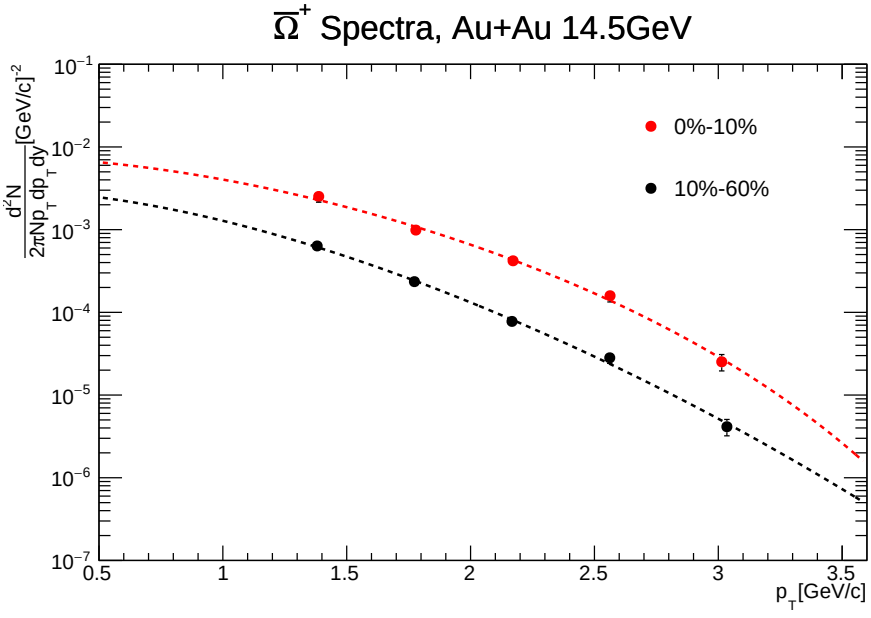

Figure 5.2: Corrected spectra of $\bar{\Omega}^+$ in Au+Au collisions at $\sqrt{s_{NN}} = 14.5$ GeV.

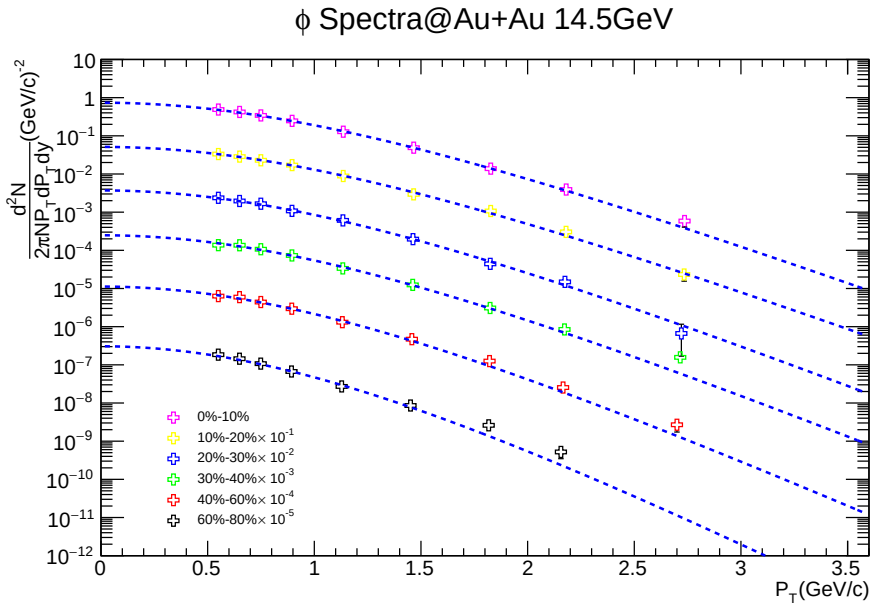

Figure 5.3: Corrected Spectra for ϕ in Au+Au collisions at $\sqrt{s_{NN}} = 14.5$ GeV.

5.1.2 Antibaryon-Baryon ratio

Figure 5.5 depicts the collision energy dependence of anti-baryon over baryon ratios for Ω, Ξ, and Λs. The data shows a very clear hierarchy of the ratios ($\bar{\Omega}/\Omega > \bar{\Xi}/\Xi > \bar{\Lambda}/\Lambda$) and the three trends are separated further as the energy decreases. This result is consistent with predictions made by statistical thermal models [BCK$^+$01] [BMG06] [RT02] [ABMS06].

It has been proposed in Ref. [Cle98] that a statistical model (with parameters of particle mass, degeneracy factor, baryon/strangness/charge chemical potentials (μ_B, μ_S, μ_Q), a strangeness saturation factor (γ_s) and a chemical freeze-out temperature T) can be used to describe the anti-baryon and baryon yields. If we take the log of the anti-baryon to baryon ratio, many unknown parameters will be canceled out and the expression below emerges:

$$\ln(\bar{B}/B) = -2\mu_B/T + \mu_S/T \cdot \Delta S \tag{5.1}$$

where ΔS is the strangeness difference between measured baryon and anti-baryon (e.g., $\Delta S = 2$ for $\Lambda(\bar{\Lambda})$, $\Delta S = 6$ for $\Omega(\bar{\Omega})$). Given the measured $\bar{B}/B$ ratio and ΔS, a linear relationship between μ_B/T and μ_S/T can be obtained. Figure 5.7 shows the fitting using data points measured in Au+Au at 14.5 GeV. If we take μ_B/T and μ_S/T as the independent

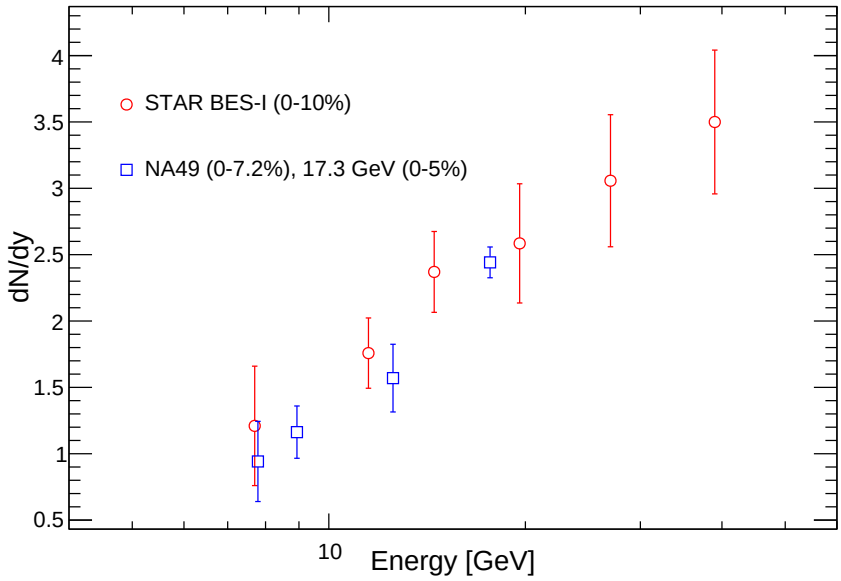

Figure 5.4: Energy dependence of mid-rapidity ($|y| < 0.5$) ϕ meson yields in central Au+Au and Pb+Pb collisions. Statistical and systematic errors are added in quadrature. NA49 data is taken from Ref. [A+08]

.

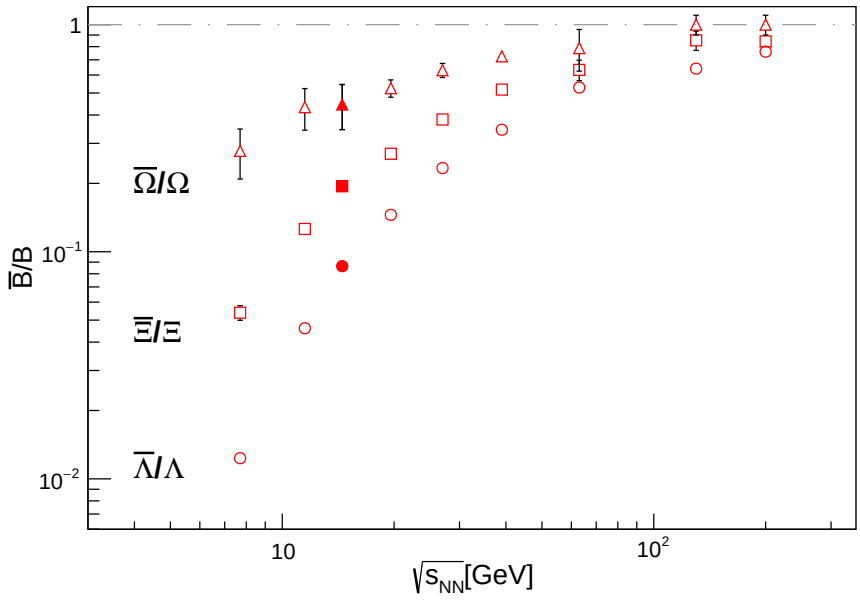

Figure 5.5: Energy dependence of anti-baryon/baryon ratios for Λ (circles), Ξ (sqaures), $and \Omega$ (triangles)s at STAR. Solid markers are the preliminary results for 14.5 GeV Au+Au collisions.

variables in Eq. 5.1, three straight lines for three particle species (Λ, Ξ, Ω) can be used to test the validity of the thermal model. As shown in Fig. 5.6, within error bands, the three lines cross at a single point that corresponds to the fitted result, which is consistent with the expectation from the thermal model.

The same procedures are applied to other energies in BES-I and the energy dependence of the obtained μ_B/T and μ_S/T are shown in Fig. 5.8. The red markers on the figure represent the result of fitting the thermal model to the yields of $\pi, K, p, \Lambda, \Xi, K^0_S$, and Ω at 39 GeV [A$^+$17a].

5.1.3 Nuclear Modification Factor R_{cp}

The nuclear modification factor is a sensitive tool to detect the production dynamics and hadronization process in relativistic heavy ion collisions. R_{cp}, the binary-collision number-

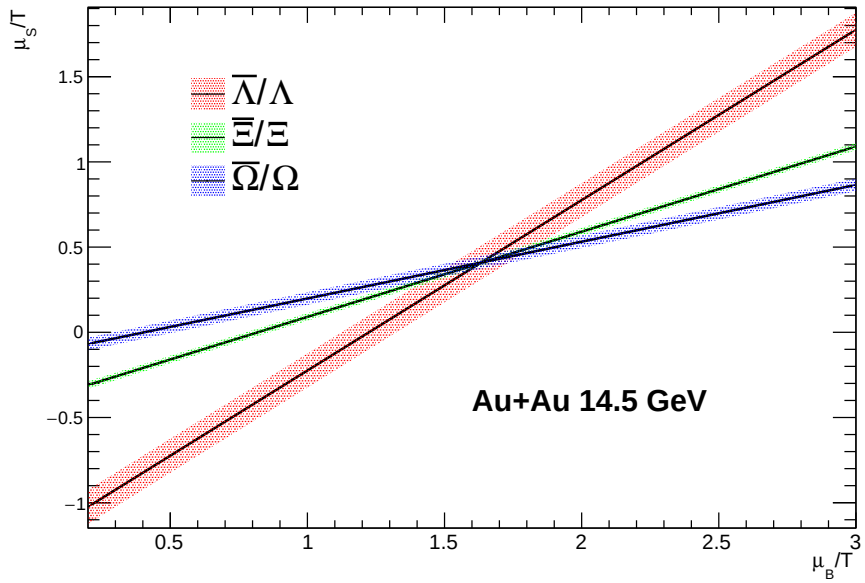

Figure 5.6: A test for thermal model parameter (μ_B/T and μ_S/T) space with $\bar{\Lambda}/\Lambda, \bar{\Xi}/\Xi$ and $\bar{\Omega}/\Omega$ ratios in the most central Au+Au 14.5 GeV collisions.

scaled particle yield ratio of central to peripheral collisions, is defined as:

$$R_{cp} = \frac{[dN/(N_{\rm coll}dp_T)]^{\rm central}}{[dN/(N_{\rm coll}dp_T)]^{\rm peripheral}} \tag{5.2}$$

where $N_{\rm coll}$ is the number of binary collisions that can be obtained from Glauber Monte-Carlo simulation. If the central nucleus-nucleus collisions are just superpositions of nucleon-nucleon collisions, this quantity is expected to be unity. Figure 5.9 shows the R_{cp} comparison between Au+Au collisions at 14.5 GeV and 200 GeV (taken from Ref. [A$^+$09]). For Au+Au 14.5 GeV, R_{cp} increases from 0.5 at low p_T to around 2.0 in intermediate p_T range. By contrast, the Au+Au 200 GeV result shows the R_{cp} of ϕ mesons is significantly below unity over a p_T range from 0.5 to 4.5 GeV/c. This sharp difference may indicates that the nuclear matter created in these two collision systems is very different and the suppression of $R_{\rm cp}$ in 200 GeV collisions could be a hint for a strong medium effect. Figure 5.10 shows the transverse momentum-dependence of R_{cp} for BES-I energies. We can observe that when the collision energy is equal to or less than 14.5 GeV, R_{cp} is monotonically increasing as p_T rises. For the other energies, the rising trend stops at intermediate $p_T \sim 2$ GeV/c and fall to unity for the

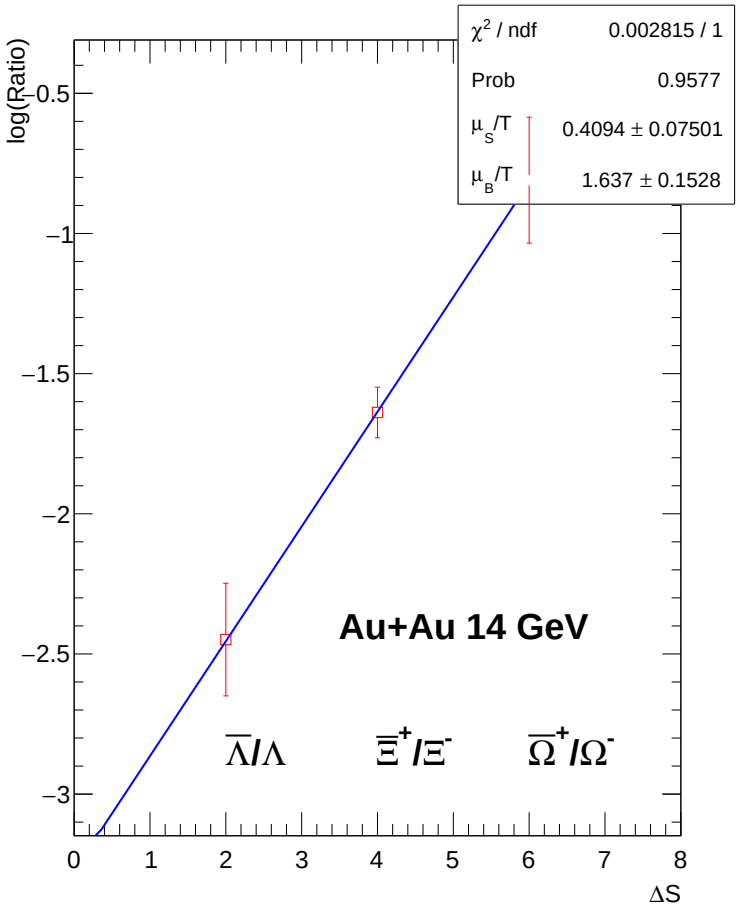

Figure 5.7: μ_B/T and μ_S/T determination for AuAu 14.5 GeV collisions using thermal model fitting. The $\bar{\Lambda}/\Lambda$ and $\bar{\Xi}^+/\Xi^-$ are from Ref. [Ash16] (with 10% estimated systematic error).

higher p_T range. This may indicate the medium effect becomes less important and hadronic dynamics starts to dominate for energies $\leq$ 14.5 GeV. For comparison, the K^0_s result (except 14.5 GeV) is also shown and similar energy-dependent features are observed.

5.1.4 Ω/ϕ Ratio

As mentioned before, multi-strange hadrons, such as $\phi(s\bar{s})$ mesons and $\Omega(sss)$ hyperons, are expected to have relatively small hadronic interaction cross-sections [Sho85] [vHSX98], which grants them the advantages of carrying early chemical freeze-out stage information with little or no distortion from hard scatterings. In addition, very minimal feed-down

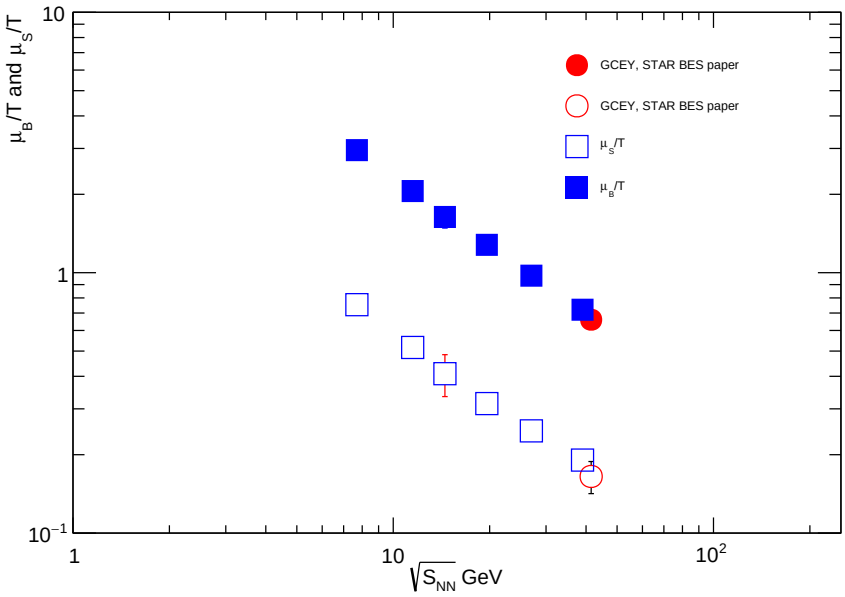

Figure 5.8: Energy dependence of μ_B/T and μ_S/T in the most central Au+Au collisions. The red markers are the result from the thermal model fitting to yields of a wide range of particles ($\pi, K, p, \Lambda, \Xi, K^0_S$) in AuAu 39 GeV collisions [A$^+$17b].

contamination is expected for Ω and ϕ production. Therefore, Ω and ϕ can carry primordial information of the collision to effectively detect the underlying transition from partonic to hadronic dynamics in heavy ion collisions.

Figure 5.11 shows the transverse momentum dependence of $N(\Omega^- + \bar{\Omega}^+)/(2N(\phi))$ in Au+Au collisions at 14.5 GeV, along with other energies in BES-I [A$^+$16b] and 200 GeV data [A$^+$07b] [A$^+$09]. The lines (dashed and solid) represent recombination/coalescence model calculations from [HY02] [HY07]. The dashed line includes the contribution from thermal quarks only and the solid line includes contributions from high p_T shower-partons. These calculations claim that most of the ϕ and Ω production up to intermediate transverse momentum is attributed to recombination/coalescence of thermal strangeness quarks that follows an exponential p_T distribution. Therefore, the deviation from the dashed line at low p_T can be interpreted as a hint that thermal strangeness quarks may not have an exponential p_T distribution. Also, particle production mechanisms, other than recombination/coalescence picture, could play an important role if data deviates significantly from the

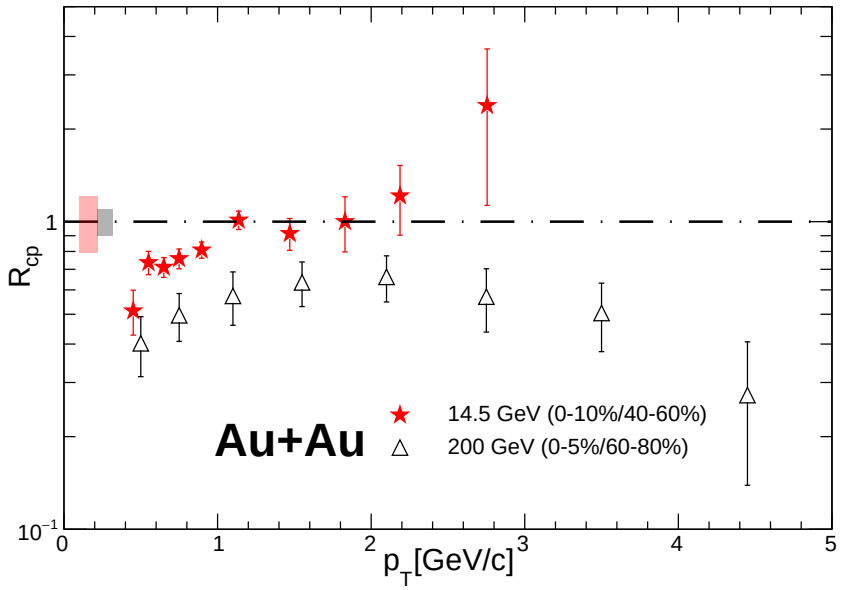

Figure 5.9: p_T dependence of $R_{\rm cp}$ for ϕ mesons in Au+Au collisions at $\sqrt{s_{NN}} = 14.5$ and 200 GeV (statistical uncertainty only). The red (gray) bar on the left indicates the normalization error introduced by $N_{\rm coll}$ for Au+Au 14.5 (200) GeV, which is around 20 (10)%.

calculation.

It can be observed that in Au+Au collisions at 19.6, 27 and 36 GeV, the ratios closely follow the 200 GeV result, which monotonically increases up to $p_T \sim 4.0 GeV/c$ and then starts turning down afterwards. This result is roughly consistent with the predictions from the recombination/coalescence picture for p_T ranging from 1.0 to 4.0 GeV/c. By contrast, the ratios for lower energies (7.7, 11.6 and 14.5 GeV) start falling at $p_T \sim$ 2.0 GeV/c and cluster together closely over the measured p_T range. Given the relatively small hadronic scattering cross section of ϕ and Ω, this significant difference may originate from the partonic rather than the hadronic phase. Thus, the gap between energy 19.6 GeV (or above) and energy 14.5 GeV (or below) could be a strong indication of the transition from partonic to hadronic dynamics with decreasing collision energies. This also narrows the collision energy corresponding to the possible onset of de-confinement down to the interval from 14.5 GeV to 19.6 GeV.

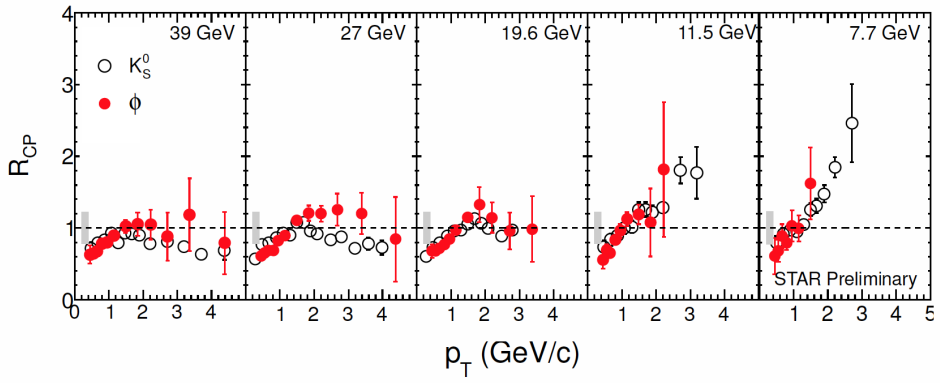

(a)

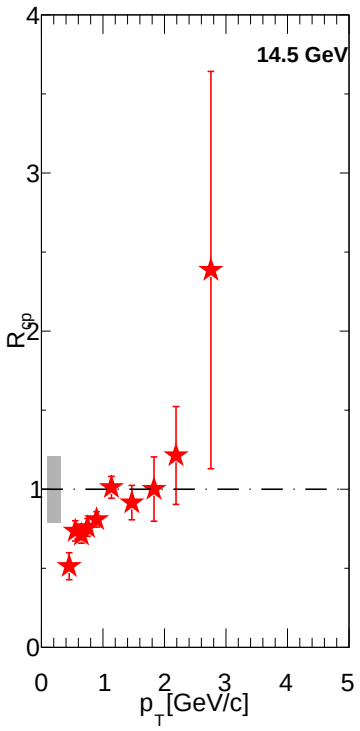

(b)

Figure 5.10: Transverse momentum dependence of $R_{\rm cp}$ for K_s and ϕ in Au+Au collisions at $\sqrt{s_{\rm NN}} = 39$ (a), 27 (a), 19.6 (a), 11.5 (a), 7.7 (a) and 14.5 (b) GeV (data points in subfigure (a) are taken from [Nas13]. Error bars give the statistical uncertainty only and the gray bar is the error from $N_{\rm coll}$.

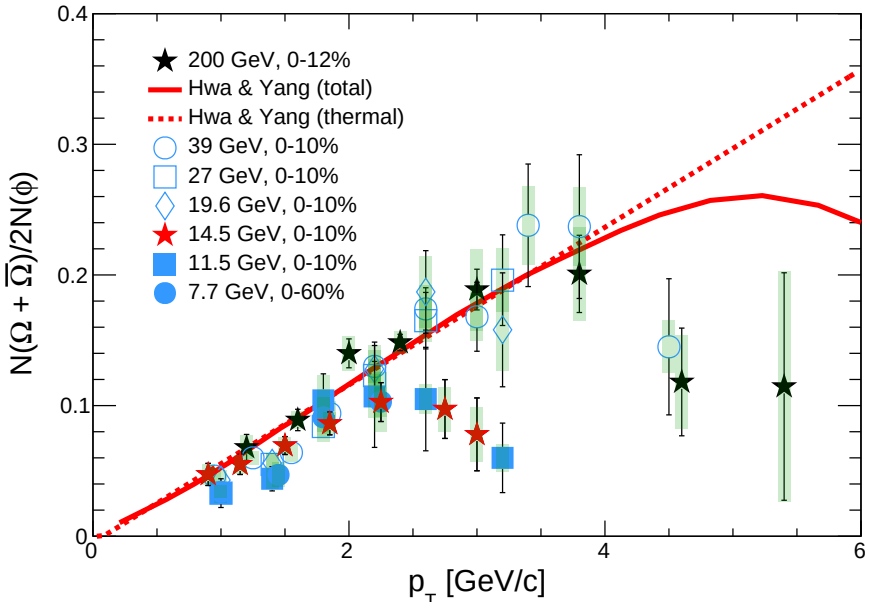

Figure 5.11: Ω/ϕ ratio as a function of p_T in mid-rapidity ($|y| < 0.5$) from Au+Au collisions at $\sqrt{s_{NN}} = 7.7 - 200$ GeV (green bands are systematic error). The solid and dashed lines are from the recombination model calculations for central collisions Au+Au collisions at $\sqrt{s_{NN}}$=200 GeV with total and thermal quark contributions, respectively.

5.2 Search for CME Using Identified Particle Correlation

The three-point correlator γ_{112} has been used extensively to measure the fluctuations in the charge separation magnitudes and we use subtraction of Opposite-Sign (OS) and Same-Sign (SS) charged particle pairs to suppress common backgrounds. Recent studies have indicated that a considerable amount of residual background remains in the subtracted γ_{112} correlator [A$^+$14b] [K$^+$17]. To quantify the range of the residual background, we use the κ_K parameter to compare with the expected range of known background levels from AMPT simulations (v2.21, string melting, hadronic scattering turned on, charge not strictly conserved [LKL$^+$05]).

5.2.1 γ_{112} Correlation for $\pi\pi$, πp, pp, and pK Pairs

In Au+Au 200 GeV collisions, as shown in Fig. 5.12, the $\Delta\gamma_{112}$ correlation for charged $\pi\pi$ (empty red circles) shows sizable signal in peripheral centralities. The magnitude of signal gradually decreases as collisions become more central. The charged hadron result [A+14b] is plotted with solid blue circles and shows similar trend. In the most peripheral collisions (60%-80%), $\pi\pi$ has stronger signal than hh, while very close values of $\Delta\gamma_{112}$ can be found in mid-peripheral to central collisions. To compare with the background model, AMPT (without CME induced charge separation implemented) simulated $\Delta\gamma_{112}$ for $\pi\pi$ is plotted in cyan band and showing very similar relationship between $\Delta\gamma_{112}$ and collision centrality, though the signal magnitude is lower than the data.

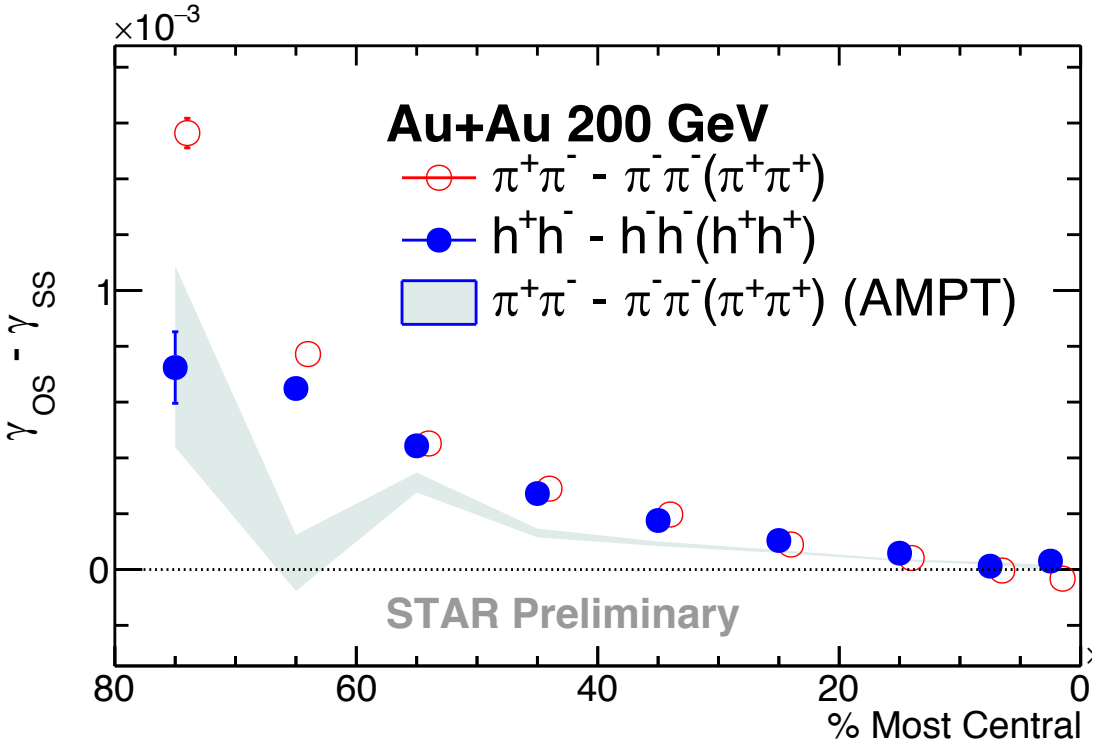

Figure 5.12: $\Delta\gamma_{112}$ for $\pi\pi$ correlation in Au+Au 200 GeV. AMPT simulation and charged hadron correlation result are presented for comparison.

As a cross-check, the similar measurement in Au+Au 39 GeV is shown in Fig. 5.13. The result of $\pi\pi$ is found to be very close to hh correlation within error bars. Significant difference between opposite-sign and same-sign correlation can be observed from peripheral

to mid-central collisions.

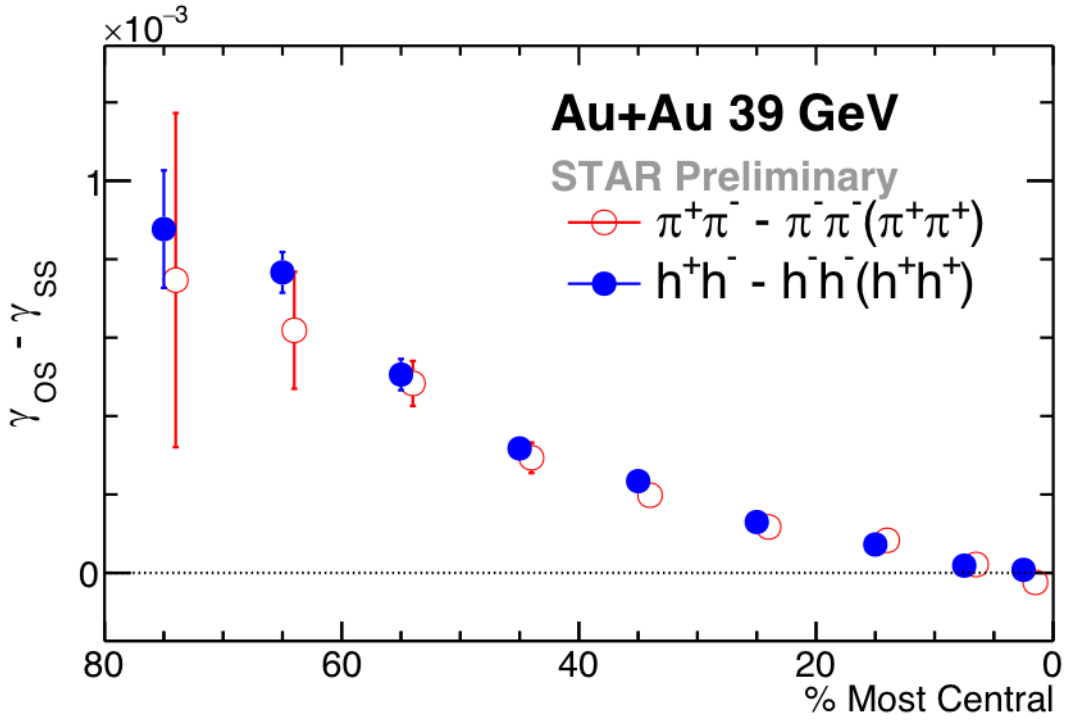

Figure 5.13: $\Delta\gamma_{112}$ for $\pi\pi$ and hh correlation [A$^+$14b] in Au+Au 39 GeV collisions.

Other major constituents of hh correlation could be from πK, pK and pp pairs. In Fig. 5.14, the measurements of both Au+Au 200 GeV and 39 GeV collisions show significant signals of πK correlation in mid-peripheral to mid -central collisions. The magnitude is similar to hh or $\pi\pi$ results. The pK correlation of Au+Au 200 GeV, as plotted in Fig. 5.15 is also similar to hh. Most interestingly, pp correlation, though showing similar trend, the signal magnitude is significantly higher than hh or $\pi\pi$. In the analysis of γ_{112}, the measurement may be contaminated by secondary tracks from decays. For example, in $p\pi$ correlation, Λ decays into π and p that may drag down $\langle\cos(\phi_a + \phi_b - 2\Psi_2)\rangle$. An estimation of this kind of contribution was studied using invariant-mass spectrum of the correlated pairs. We can find from Fig. 5.17, the opposite sign correlation between $p\pi^-$ from Λ is concentrating around zero for three the most peripheral centralities. In Fig. 5.18, a sharp peak of Λ's can be observed. However, the ratio of the area under the peak over the total area is extremely small and it decreases as the collisions become more central. Thus it is safe to say this

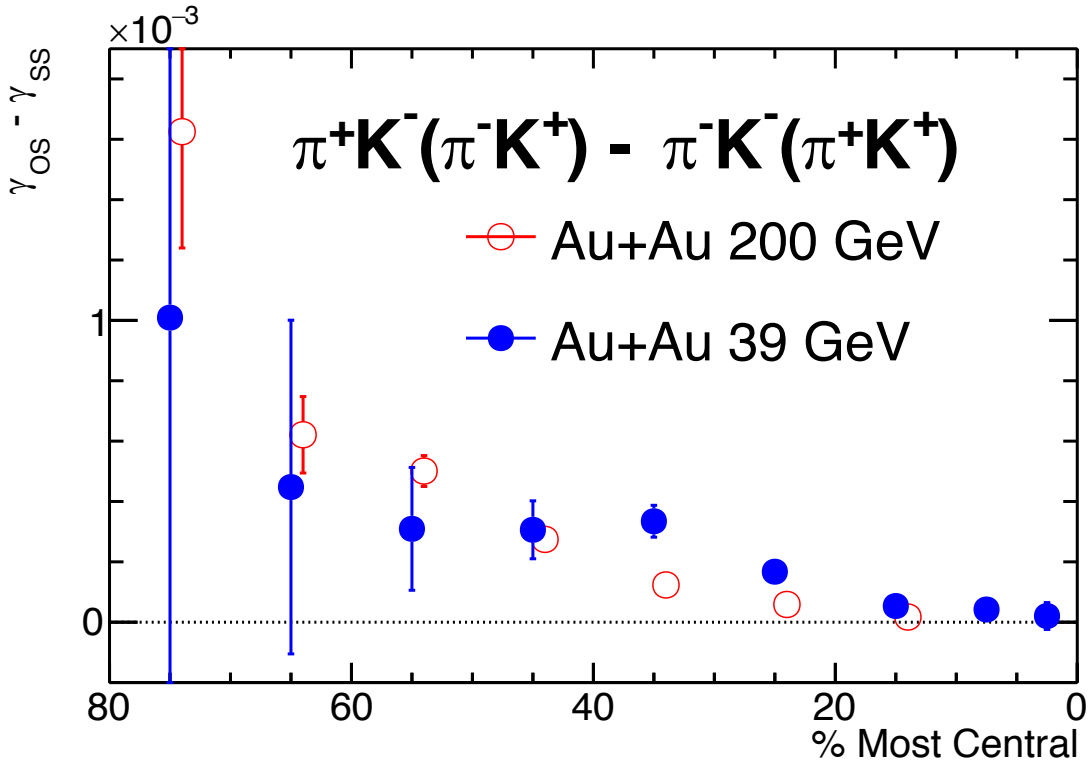

Figure 5.14: $\Delta\gamma_{112}$ for πK pairs in Au+Au 200 and 39 GeV.

correlation due to the Λ daughter contamination is negligible. To be continued.

5.2.2 Comparison with the CME Background Model

As pointed out multiple times in previous text, several background physics mechanisms may also contribute to the $\Delta\gamma_{112}$ signal observed. The Eq. 4.29 defines a flow normalized "γ_{112}" observable, κ_K, which can be used to compare with background model to evaluate the magnitude of known background quantitatively. The κ_K of hh pairs for Au+Au collisions at BES energies larger than 7.7 GeV shows the data is well above the background model (AMPT) in peripheral to mid-central collisions. The κ_K for Au+Au 7.7 GeV collisions shows weak centrality dependence with values near $1.0 - 2.0$, which coincides with AMPT simulations. An "anatomy" of the charged hadron κ_K could be interesting to see the contribution of different identified particle pairs.

The κ_K for $\pi\pi$ as a function of centrality in Au+Au collisions at 200 and 39 GeV can be

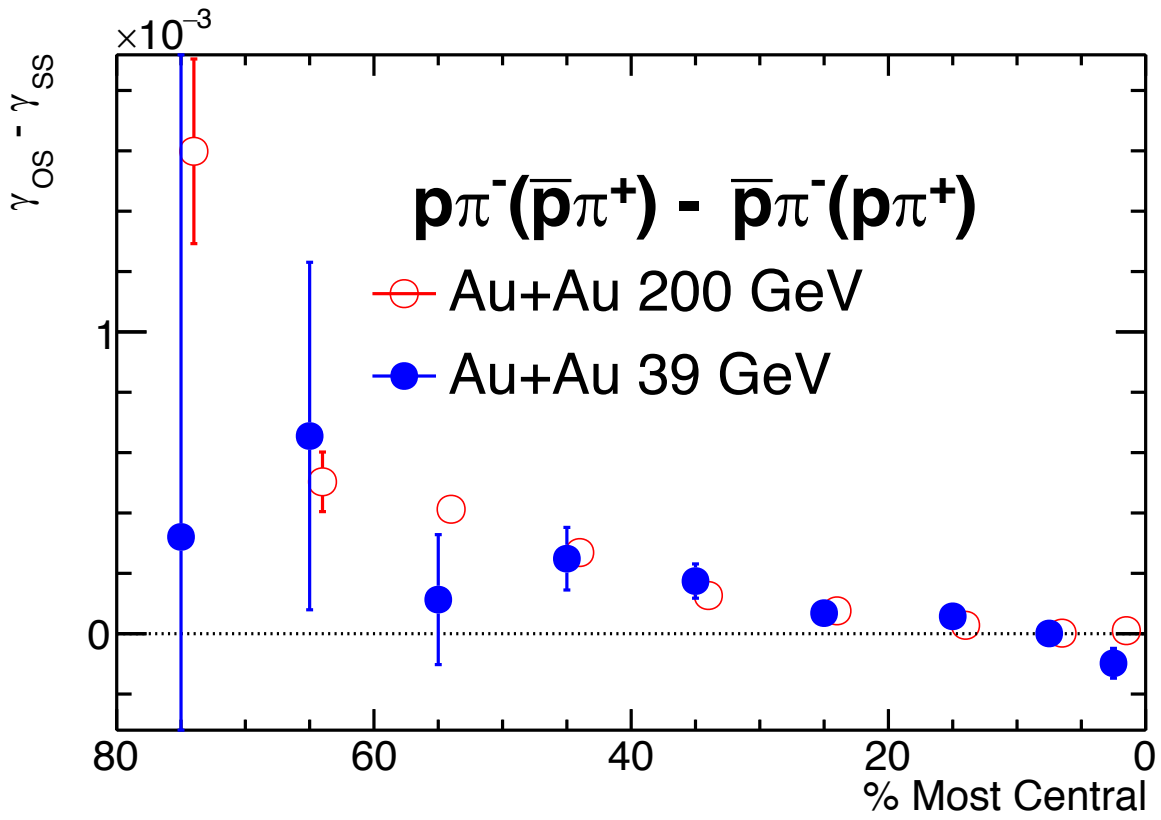

Figure 5.15: $\Delta\gamma_{112}$ for $p\pi$ pairs in Au+Au 200 and 39 GeV.

found in Fig. 5.20 and Fig. 5.21. $\pi\pi$ shows larger signal magnitude than hh for peripheral to mid-peripheral centralities in both energies.

The other combinations (Fig. 5.22-Fig. 5.24), except pp correlation, are all producing κ_K that is close to the pure background scenario with very slight centrality dependence. κ_K for pp is found to be lower than unity in mid-peripheral and mid-central collisions.

These results seem to suggest that the major contribution to hh charge separation signal arises from $\pi\pi$. The other particle pairs cannot be distinguished from background scenario and will require more simulation statistics to determine the background. The charge separation and background level for pp is very different from the rest and further investigation is needed.

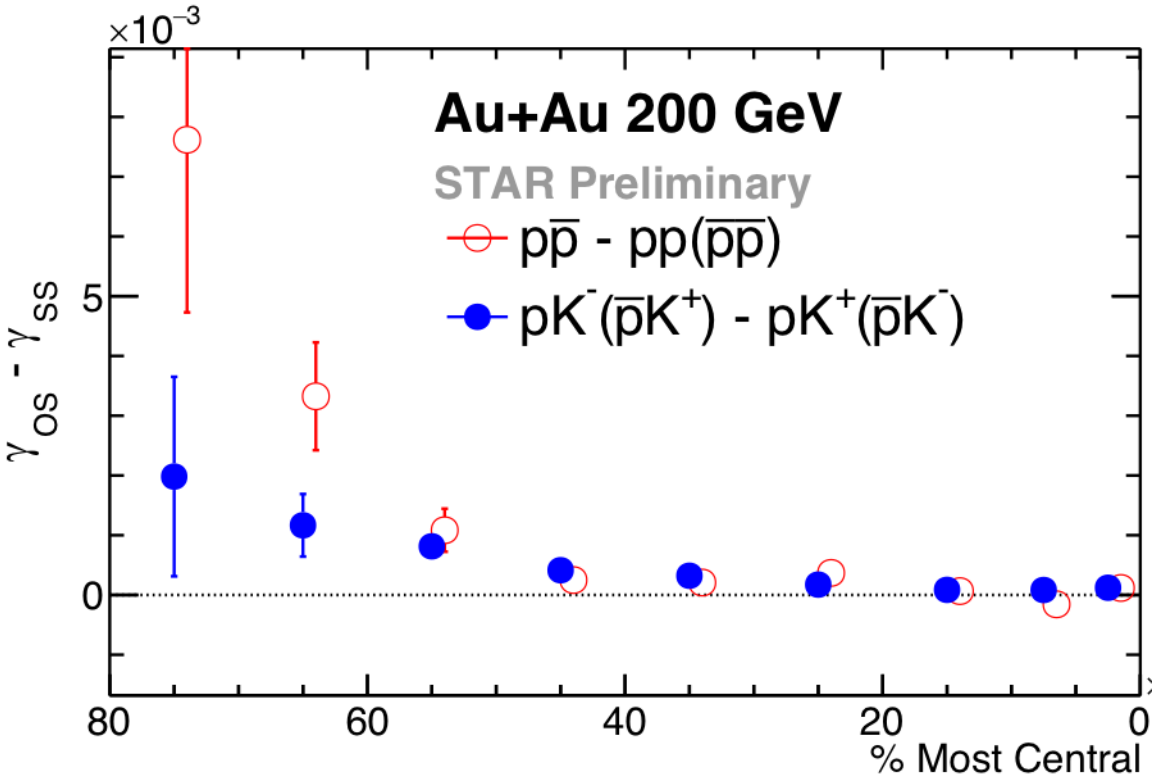

Figure 5.16: $\Delta\gamma_{112}$ for pp and pK correlation in Au+Au 200 GeV and Au+Au 39 GeV.

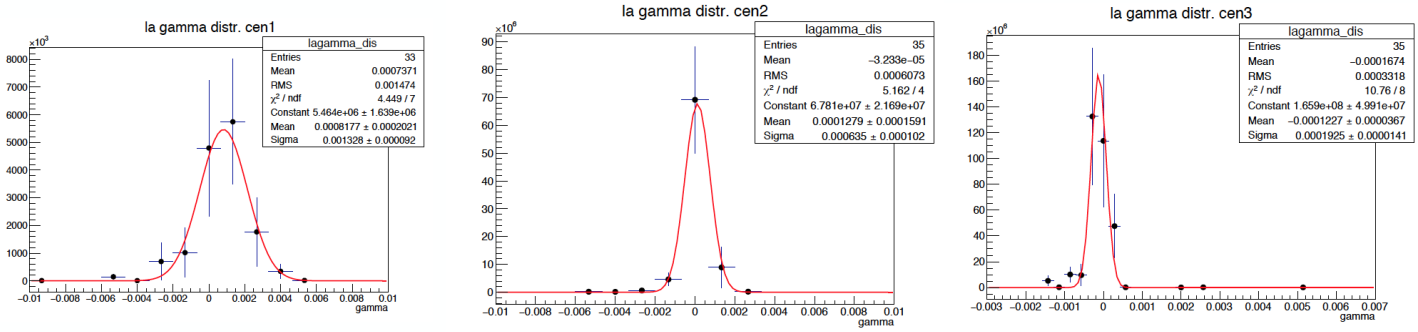

Figure 5.17: Distribution of γ_{112} of mis-identified Λ daughters.

5.3 Search for CVE using γ_{112} Correlation for Λp

Using Λp correlation to search for baryon number separation is based on the assumption that CME cannot contaminate the measurement due to the charge neutrality of Λ hyperon. Therefore, any finite separation signal observed could be interpreted as hints for baryon number separation driven by the vorticity. In Ref. [Zha14], the measurement of γ_{112} for

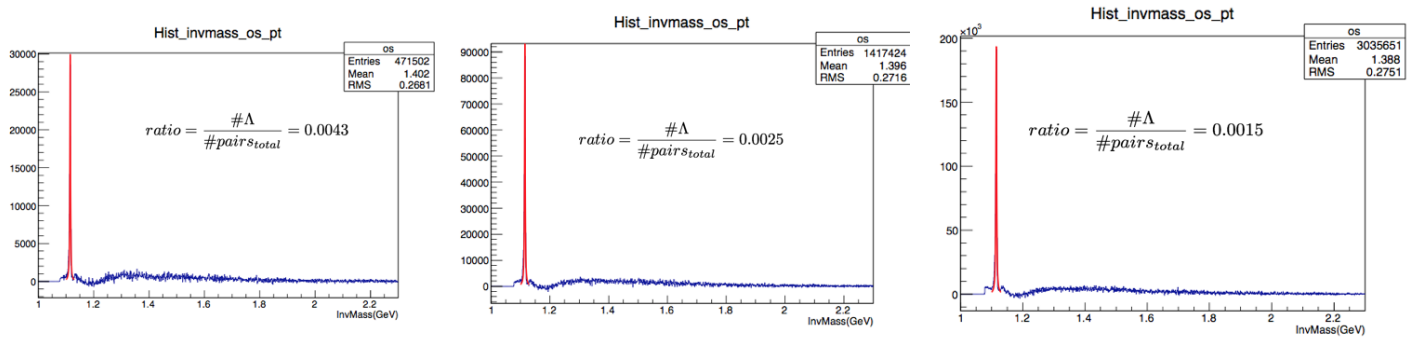

Figure 5.18: Invariant mass spectrum of $p\pi^-$ pairs in γ_{112} measurement for the 70%-80%, 60%-70%, and 50-60% central collisions of Au+Au 200 GeV.

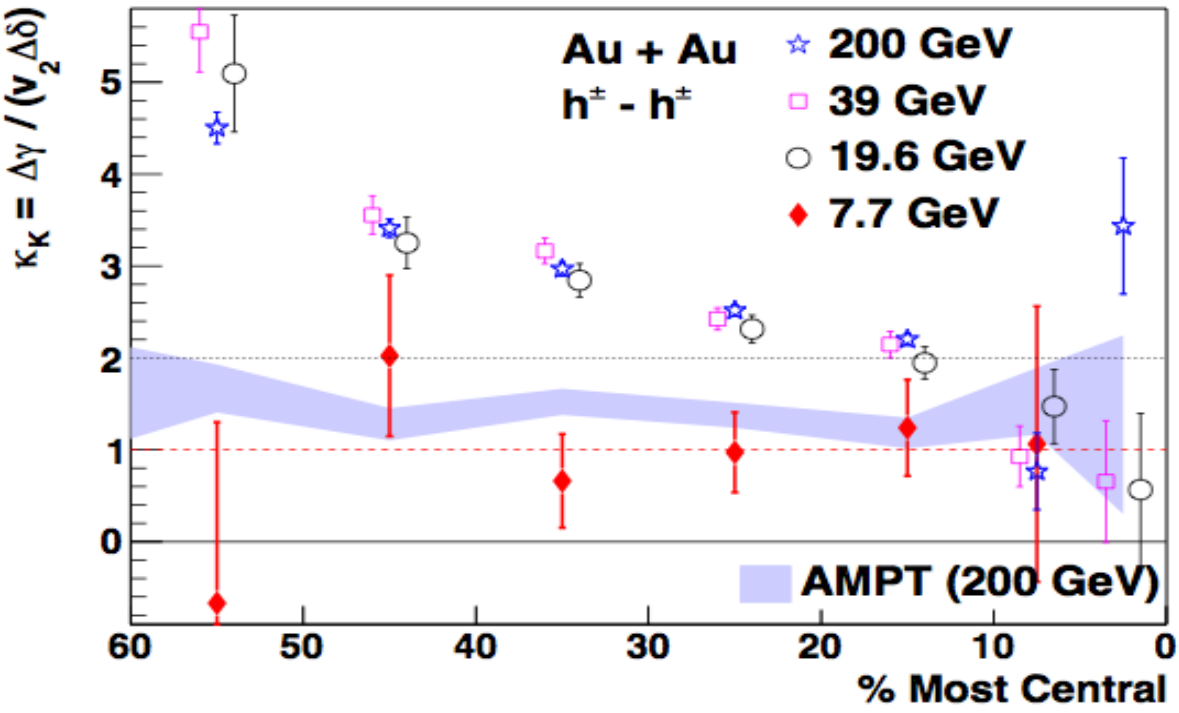

Figure 5.19: κ_K for charged hadron in Au+Au collisions at 7.7, 19.6, 39, 200 GeV [A$^+$14b].

Λp in Au+Au collisions at $\sqrt{s_{NN}}$ = 200 GeV was carried out for the first time and the result is shown in Fig. 5.25. Nonzero value of $\Delta\gamma_{112}$ for Λp can be observed in non-central Au+Au collisions. Meanwhile, a few systematic checks have been done in Ref. [Zha14] and show that the signal disappears in $\Lambda h^{\pm}$ and $K^0_S p$ measurements. All of these results strongly implies the baryon number dependence of the separation signal. Given this intriguing study,

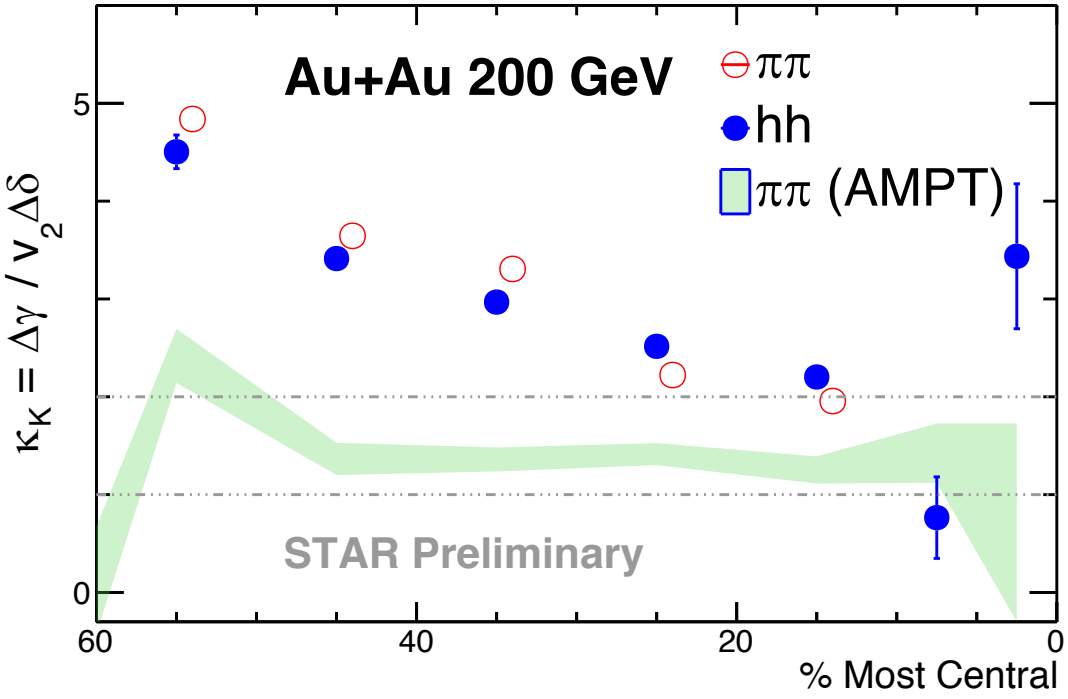

Figure 5.20: κ_K for $\pi\pi$ and hh in Au+Au collisions at 200 GeV. AMPT simulation for $\pi\pi$ is plotted with green band for comparison.

interests of measuring vorticity in heavy-ion collisions have been sparked and in the recent publication from STAR [A$^+$17c], the energy dependence of vorticity of the created medium in Au+Au collisions has been measured. Since it is not possible for direct measurement of local fluid vorticity in heavy-ion collisions, $\Lambda(\bar{\Lambda})$ hyperon polarization has been used as a proxy to probe the vorticity indirectly. $\Lambda(\bar{\Lambda})$ is called "self-analyzing" because its decaying daughter proton is preferred to be emitted in its spin direction. Thus, the spin direction of $\Lambda(\bar{\Lambda})$ can be inferred from the measurement of decay daughter proton and the average of its projection onto the system angular momentum ($\bar{\mathcal{P}}_H$) can be measured. In Fig. 5.26, the energy dependence of $\bar{\mathcal{P}}_H$ for $\Lambda(\bar{\Lambda})$ in Au+Au collisions is shown. We can observe finite signal of $\bar{\mathcal{P}}_H$ for energies lower than 200 GeV and the magnitude decreases as energy goes down. Based on hydrodynamic calculation [BKL$^+$17], vorticity of the system is proportional to the measured $\bar{\mathcal{P}}_H$ for primary $\Lambda(\bar{\Lambda})$. This interesting result of collision system vorticity suggests that the CVE induced baryon number separation may be more prominent in low

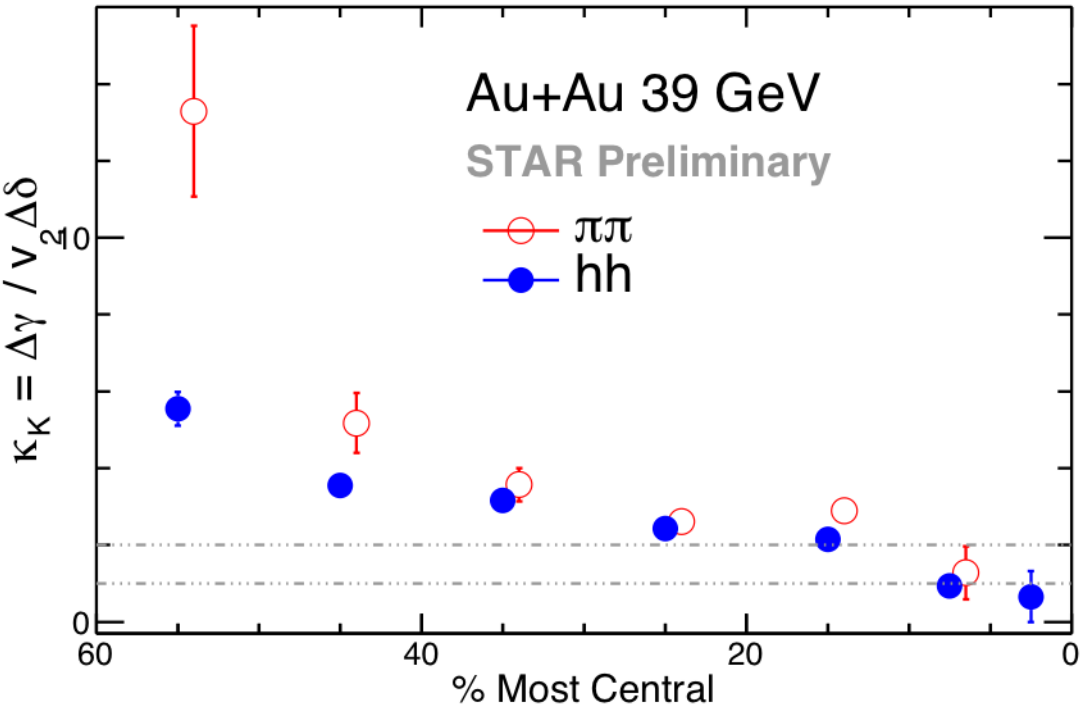

Figure 5.21: κ_K for $\pi\pi$ in Au+Au 39 GeV.

energy Au+Au collision. Due to the constraint of $\Lambda(\bar{\Lambda})$ production in low energy collision, 27 GeV could be a sweet spot to hit. As shown in Fig. 5.27, we do observe finite signal of $\Delta\gamma_{112}$ in mid-peripheral collisions, though with big error bars. As collisions become more central, the magnitude goes down which could be due to the decreasing vorticity of the created medium. Figure 5.28 shows the difference between two particle correlation of oppo- and same-signed pairs, $\Delta\delta$, is very close to zero, which may indicate that the flowing resonance decay contamination is not as serious as $\pi\pi$. If enough AMPT events are accumulated, a direct comparison between the experimental data and the one from pure background model will be useful to make a more solid conclusion concerning the existence of vorticity induced baryon charge separation in heavy-ion collisions.

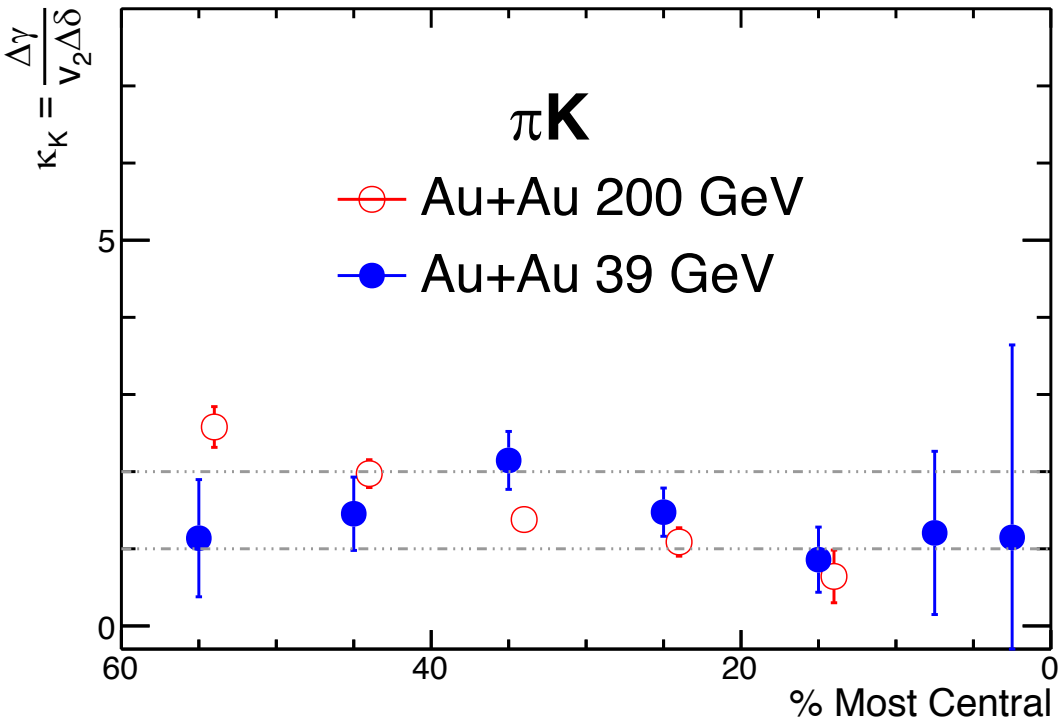

Figure 5.22: κ_K for πK in Au+Au collisions at 39 and 200 GeV.

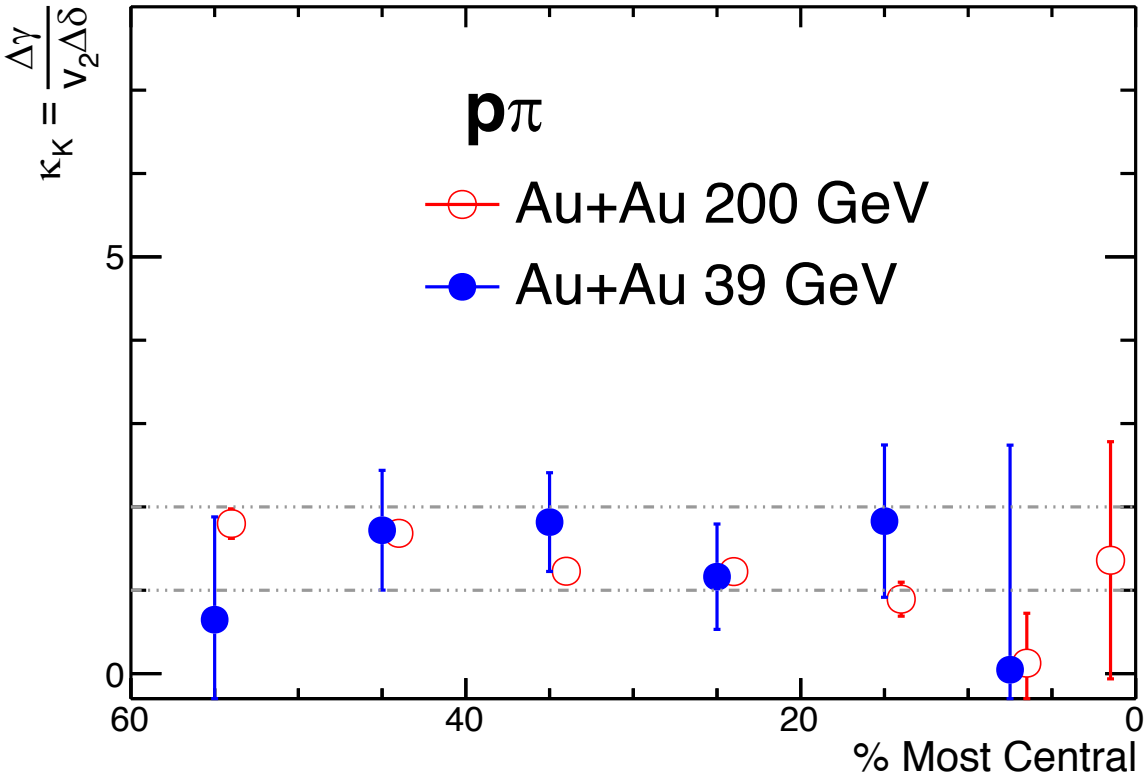

Figure 5.23: κ_K for $p\pi$ in Au+Au collisions at 39 and 200 GeV.

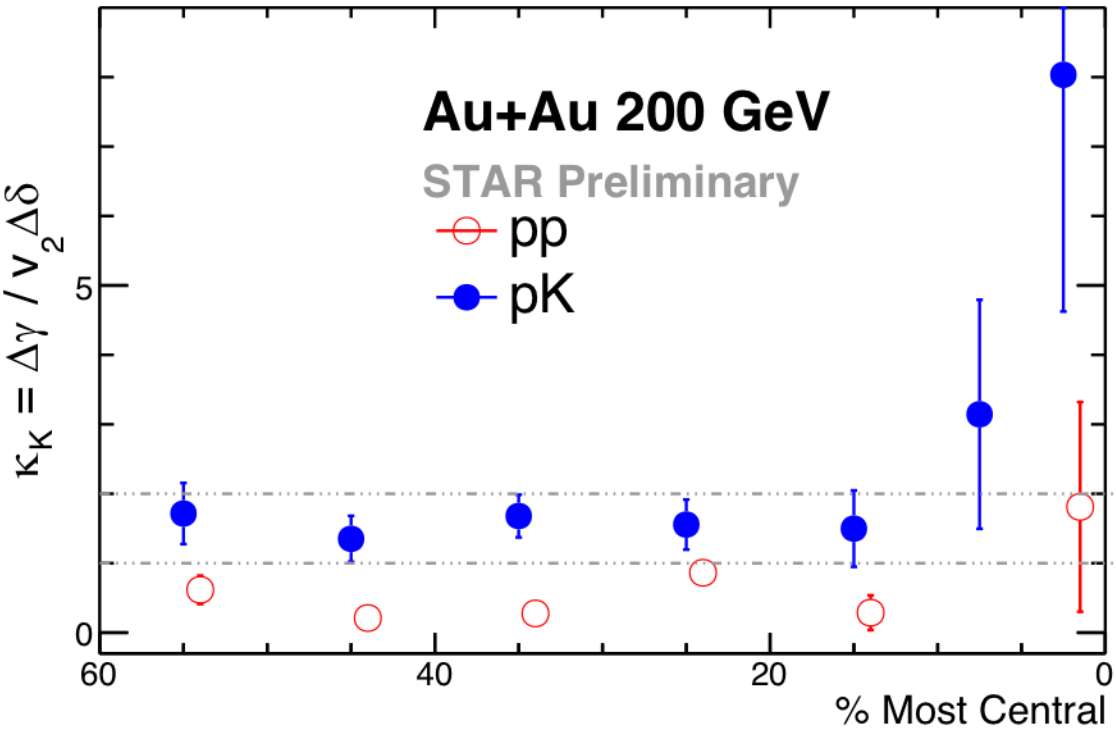

Figure 5.24: κ_K for pp and pK in Au+Au collisions at 200 GeV.

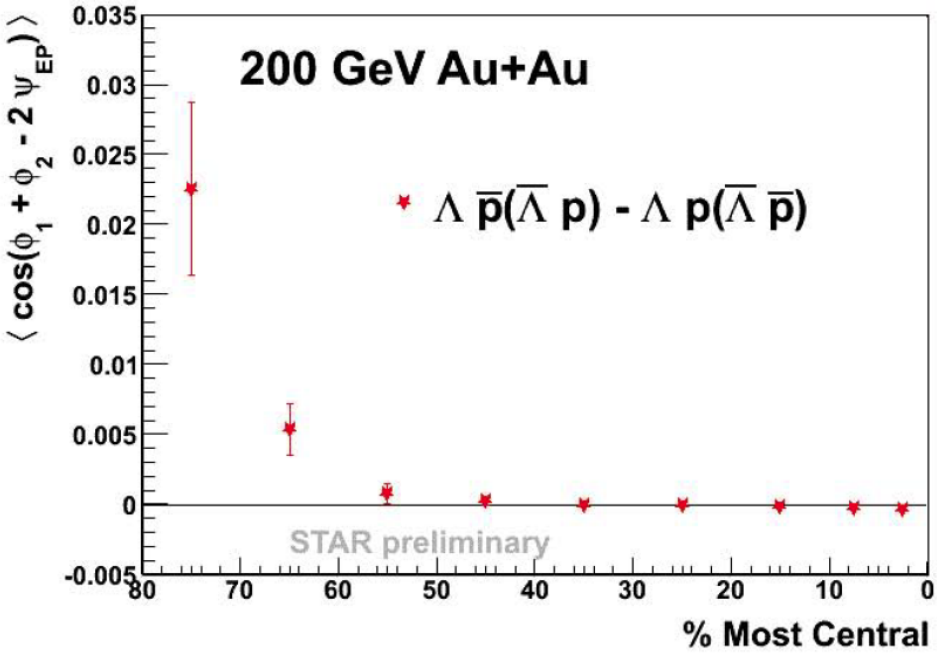

Figure 5.25: (Taken from Ref. [Zha14]) $\Delta\gamma_{112}$ for Λp correlation in Au+Au collisions at $\sqrt{s_{NN}}$ = 200 GeV at STAR.

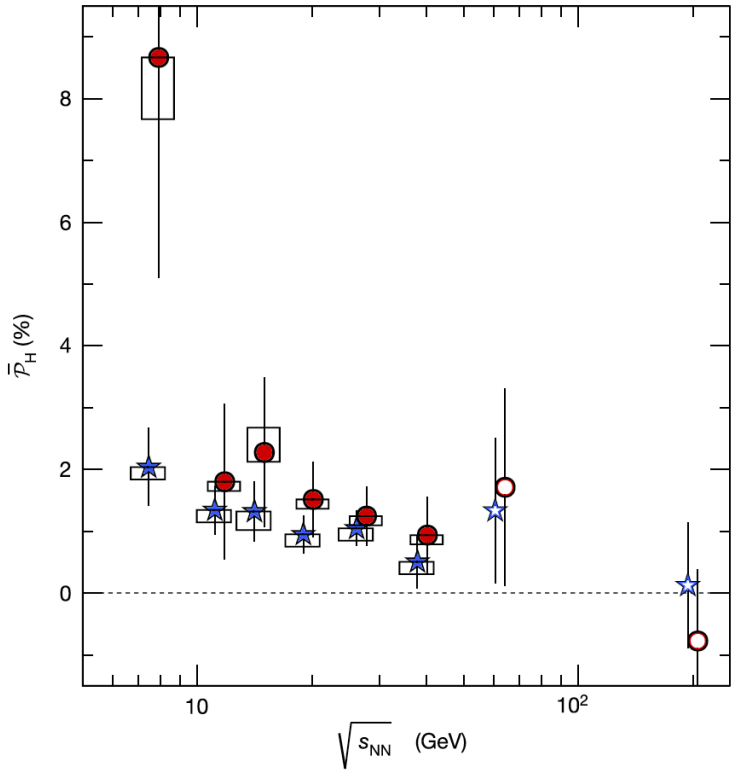

Figure 5.26: (Taken from Ref. [A$^+$17c])Collision energy dependence of the average polarization for Λ (blue stars) and $\bar{\Lambda}$ (red circles) in 20-50% central Au+Au collisions. Open symbols are representing results from previous studies [A$^+$07a].

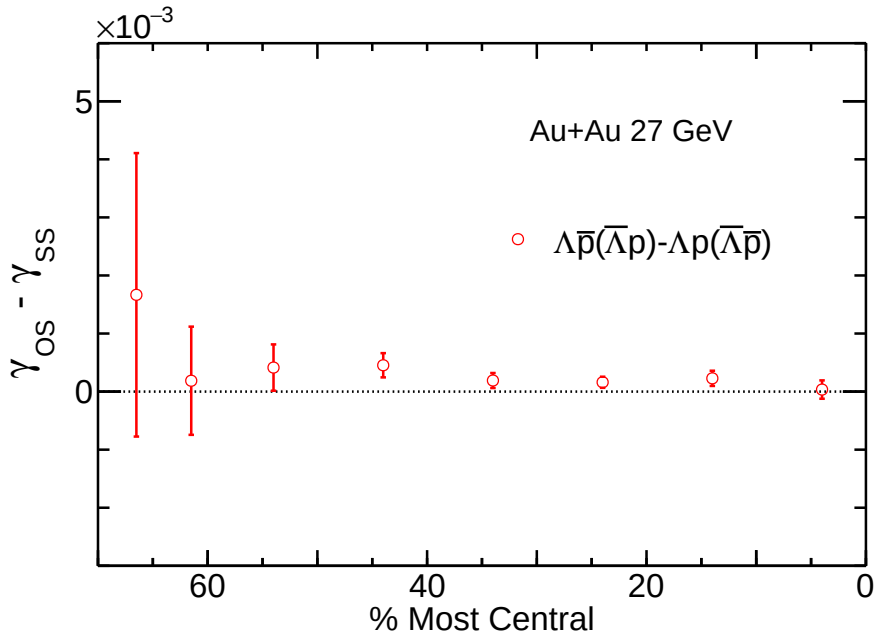

Figure 5.27: $\Delta\gamma_{112}$ for Λp in Au+Au collisions at $\sqrt{s_{NN}} = 27$ GeV at STAR.

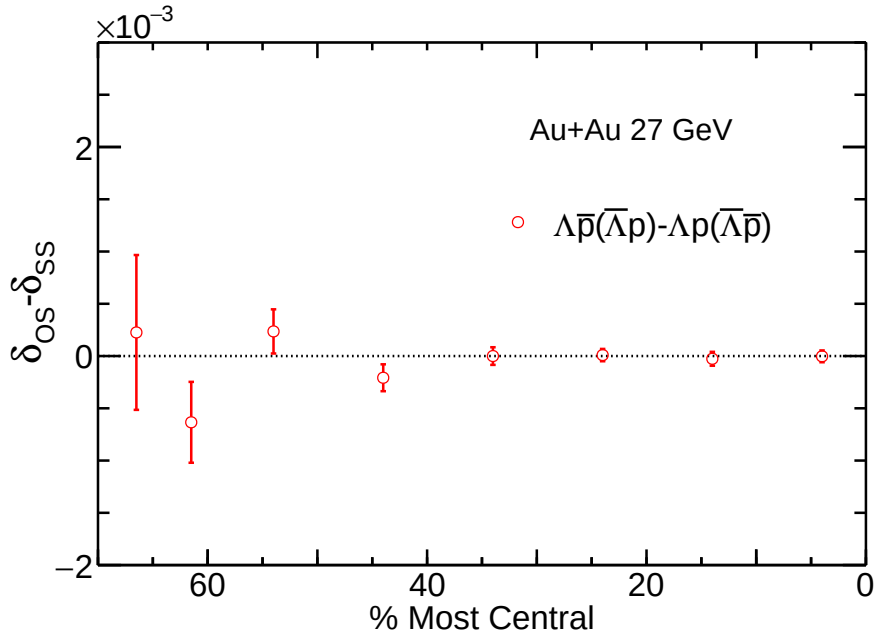

Figure 5.28: $\Delta\delta$ for Λp in Au+Au collisions at $\sqrt{s_{NN}} = 27$ GeV at STAR.

CHAPTER 6

Outlook:Towards Background-Free Measurements of Chiral Effects in Heavy-Ion Collisions

6.1 The Background Coupling to Reaction Plane: Elliptic Flow

Although the γ_{112} correlation measurements at STAR show sizable signals for the CME, extensive studies have indicated that other conventional physics mechanisms, including local charge conservation (LCC) [Pra10, SP11], transverse momentum conservation (TMC) [BKL11, PSG11], particle cluster (resonance, jet, di-jets) decay [Vol04b]... may couple to reaction plane and contribute to the charge separation signal in the presence of elliptic flow (v_2).

6.1.1 Local Charge Conservation

Local charge conservation means in all fundamental processes, charges are created in balanced pairs that are produced at the same point in space-time. With strong collective flow the charge separation will be pushed outward radially differently along the directions in-plane and out-plane of the reaction plane. In Ref. [Pra10, SP11], it is pointed out that LCC could account for the difference between same charge and opposite charge γ_{112} correlations observed at STAR. LCC itself can be observed experimentally through the balance function (Eq. 3 in Ref. [SP11]), which is defined to measure the chance that a charge at angle ϕ has a balancing charge emitted with angle $\phi + \Delta\phi$. By making use of the balance function with parameters derived from the blast wave model fit to STAR spectra and v_2 data [A$^+$05a], it is convenient to compute a like-sign and opposite-sign γ_{112} correlator. Equation 8 in Ref. [SP11] shows the charge separation signal induced by the balance function is proportional to v_2. We

can find from Fig. 6.1, that the balance function computation of γ_{112} scaled with multiplicity (red squares) is very similar to STAR results.

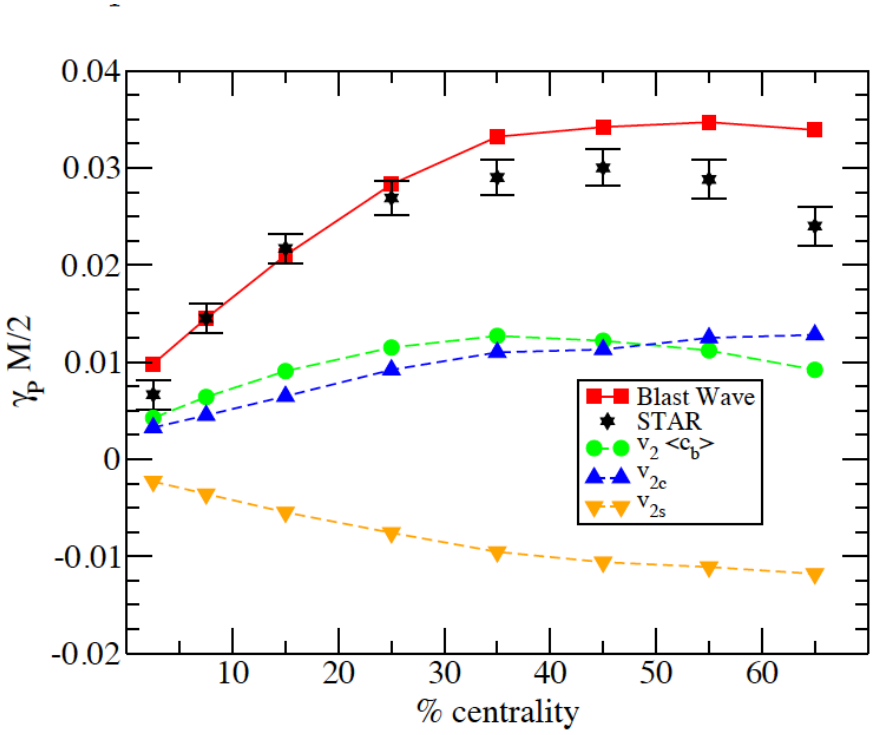

Figure 6.1: γ correlator from STAR (black stars) and blast wave calculations (red squares). The other three are the decomposition of the blast wave-induced signals (see Eq. 9 in Ref. [SP11]).

6.1.2 Transverse Momentum Conservation

Transverse momentum conservation (TMC) is a well-known possible source of azimuthal correlation of particles in heavy-ion collisions. Based on the analytical calculation (see Eq. 14 in Ref. [BKL11]), it is estimated that the signal due to the TMC, combined with elliptic flow v_2, can account for about 20%-33% of the charge separation signal that STAR has observed for very peripheral to very central Au+Au collisions at 200 GeV.

6.1.3 Particle Cluster Decay

Another possible source of the non-CME contamination in the charge separation signal $\Delta\gamma_{112}$ is particle cluster decay coupled with v_2, such as from resonance decay, jet or di-jets. It is estimated [Vol04b] that the corresponding contribution to the γ_{112} is:

$$\langle\cos(\phi_\alpha + \phi_\beta - 2\Psi_{RP})\rangle = \frac{N_{\text{pairs/event}} N_{\text{cluster/event}}}{N_{\text{pairs/event}}} \langle\cos(\phi_\alpha + \phi_\beta - 2\phi_{\text{cluster}})\rangle_{\text{cluster}} v_{2,\text{cluster}} \tag{6.1}$$

where $\langle ... \rangle_{\text{cluster}}$ means the average is taken only over pairs consisting of two daughters from the same cluster.

6.2 Three Approaches to Disentangle Flow-related Background and the CME signal

As stated above, conventional physics mechanisms, when coupled with elliptic flow, make the observable γ_{112} less powerful in detecting the charge separation effect emerging from the magnetic field. From the perspective of heavy-ion collision experiments, three approaches have been proposed to disentangle the flow-related background and the CME signal: a) U+U collisions, b) isobar collisions, and c) event-shape selection analysis. The following three sections will discuss the motivations and preliminary results of these schemes, in detail.

6.2.1 Vary the Background: U+U collisions

Experimentally, it is still not clear how to suppress the elliptic flow while preserving the magnetic field in the high energy heavy-ion collisions, however, the opposite is believed to be achievable via body-body U+U collisions [Vol10]. In central collisions, where most of the nucleons interact, the deformed uranium nuclei can collide with two, very different geometry configurations, tip-tip and body-body, as shown in Fig. 6.2. The studies of Monte-Carlo Glauber simulations [Vol10, MMX09] indicate for these two cases, very weak magnetic fields from the spectator protons will be created. However, strong elliptic flow, ∼30-60% larger

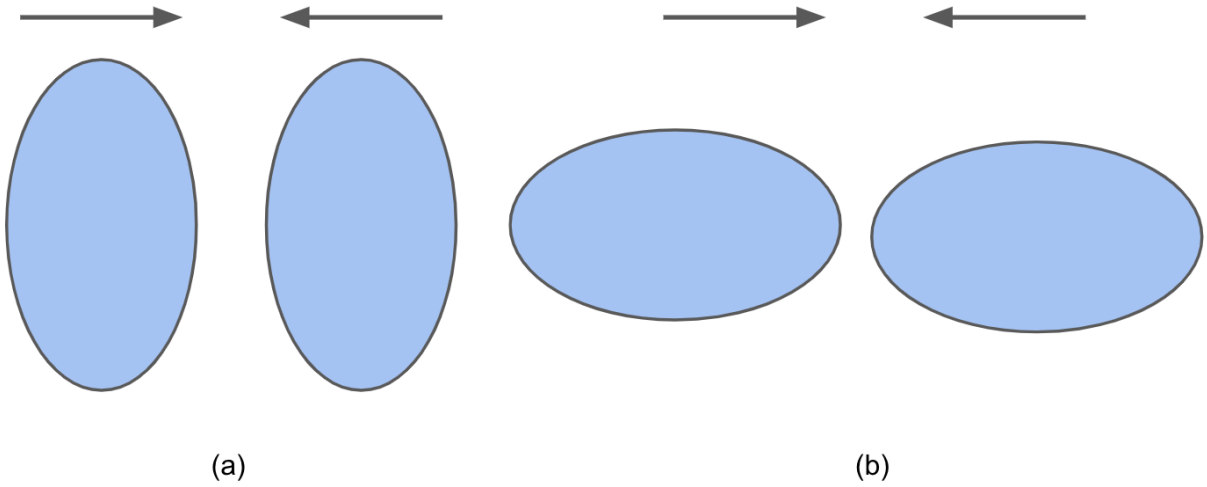

Figure 6.2: Geometry configurations of (a) body-body and (b) tip-tip U+U collisions. Arrows are aligned with the beam axis.

than the top 10% central collisions of Au+Au at 200 GeV, due to the large eccentricity still persists, but only in the case of body-body collisions. Therefore, by selecting these events, we may gain insights into the flow-related background in the scenario, without the strong magnetic field.

6.2.1.1 Preliminary Results

In 2012, STAR carried out γ_{112} measurements of U+U collisions at 197 GeV [Wan13] as shown in the Fig. 6.3. As we can observe, the very central (0-1%) U+U collisions still exhibit relatively small elliptic flow ($v_2 \sim 2.5\%$). This is due to the practical difficulties of selecting body-body type collisions based on the multiplicity measurements [A$^+$15a]. This reduces UU collision's capability of revealing the flow-related background magnitude with as large v_2 as the one in mid-central Au+Au collisions. In Fig. 6.4, the magnetic field as a function of eccentricity ϵ_2 [CT15], shows a trend which is similar to the v_2 dependence of the charge separation observable measured in the STAR detector [Wan13]. This measurement demonstrates that in very central heavy-ion collisions, where the elliptic flow is finite but magnetic field could be very small, the γ_{112} signal vanishes. Therefore, the signal is unlikely

to be due to v_2 driven background alone.

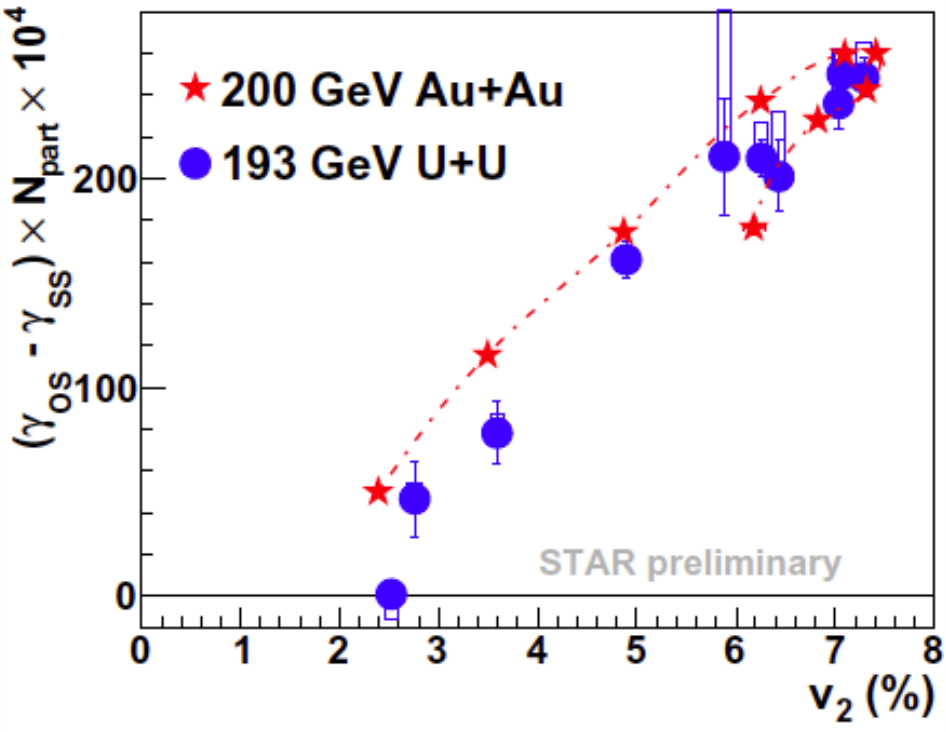

Figure 6.3: $\Delta\gamma_{112}$ v.s. v_2 comparison between Au+Au and U+U collisions.

6.2.2 Vary the Signal: Isobar Collisions

Given the practical difficulties of selecting body-body events in U+U analyses, isobar collisions provide a potentially more promising avenue to disentangle the magnetic field driven charge separation signal and flow-induced noise [Vol10]. The isobar collision program, launched in 2018 at RHIC, was planned to collide ${}^{96}_{44}$Ru $+{}^{96}_{44}$ Ru and ${}^{96}_{40}$Zr $+{}^{96}_{40}$ Zr at $\sqrt{s_{NN}} =$ 200 GeV, with the hope of varying the generated magnetic field in the two collision systems, while maintaining a similar level of flow-induced background.

6.2.2.1 Magnetic Field and Eccentricity Prediction

The driving force of charge separation in the CME is the magnetic field generated after collisions, mostly by the spectator protons [BHZL13]. Thus, the different charges in Ru and

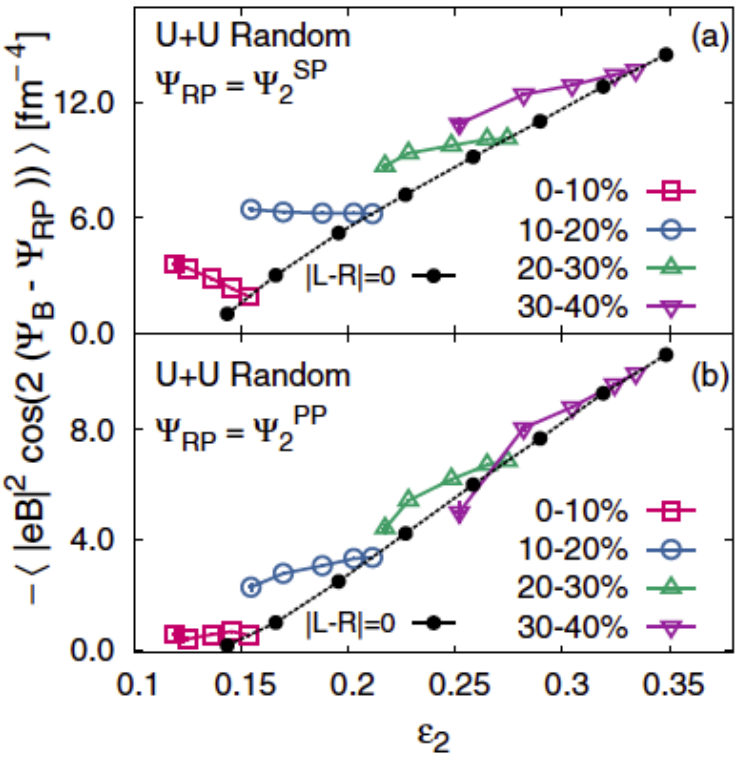

Figure 6.4: Magnetic field-induced charge separation signal as a function of eccectricity ϵ_2 in U+U collisions at $\sqrt{s_{NN}} = 193$ GeV. Top: signal measured with respect to the second-order spectator plane. Bottom: signal measured with respect to the second participant plane.

Zr nuclei become a good handle to vary the driving force, leading to differences between the charge separation signals from these two collision systems. Based on theoretical calculations of the magnetic field, investigators have compared the eccentricities and magnetic fields created in Ru+Ru and Zr+Zr collisions [DHMW16]. The results, as shown in Fig. 6.5, imply for the 20-60% central collisions of Ru+Ru and Zr+Zr collisions at 200 GeV, the relative difference of $B_{\rm sq}$ stays in the range from 15% to 18%, but the eccentricities in these two collision systems (ϵ_2), which drives the v_2, are roughly consistent with zero. Here, $B_{\rm sq}$ is defined as:

$$B_{\rm sq} = \left\langle (eB/m_\pi^2)^2 \cos[2(\Psi_B - \Psi_{\rm RP})] \right\rangle \tag{6.2}$$

where m_π is the pion mass. The reason $B_{\rm sq}$ is more interesting than B is that it is proportional to the γ_{112} observable. Therefore, the relative difference in $B_{\rm sq}$ can be directly translated to the observable's difference. The relative difference is given by $R_F = 2(F^{\rm Ru+Ru} - F^{\rm Zr+Zr})/(F^{\rm Ru+Ru} + F^{\rm Zr+Zr})$, where F could be $B_{\rm sq}, \epsilon_2$ or S (see the definition in the following text). The elliptic flow v_2 should closely follow the trend of ϵ_2. The direct study of the relative difference of v_2 will be discussed in Sec. 6.2.2.3.

6.2.2.2 Sensitivity to Magnetic Field Induced Charge Separation Effect

It is essential to estimate the background-level dependent event statistics due to flow in order to draw meaningful conclusions on magnetic field induced charge separation effect from the comparison between Ru+Ru and Zr+Zr collisions. In this study [DHMW16], the relative difference of the charge separation observables between Ru+Ru and Zr+Zr is defined as, $R_S = (1 - bg)R_{\rm sq} + bg \cdot R_{\epsilon_2}$. As shown in Fig. 6.6, with 1.2 (1.0) billion minimum-bias (specially triggered) events, a 5 (7) σ effect can be potentially observed given a background level lower than 80%.

6.2.2.3 Charge Separation Signal after Final State Interactions

Previous discussions, based on the analyses of the charge separation signal in the initial state, present the capability of isobar collisions to discern the CME signal and flow-related

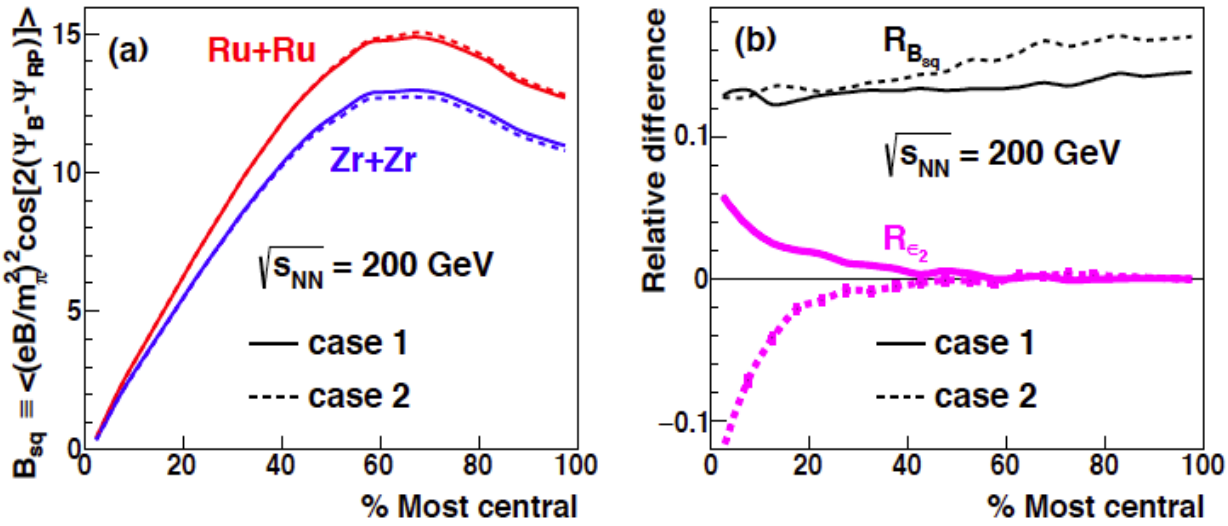

Figure 6.5: Cases 1(2) correspond to two parameter sets of Woods-Saxon potentials for two nuclei. Left: Theoretical calculation of B_{sq} in Ru+Ru and Zr+Zr at $\sqrt{s_{NN}} = 200$ GeV as a function of centrality. Right: The relative difference of B_{sq} and the initial eccentricity from the Monte-Carlo Glauber simulation.

background. However, as pointed out in an AMPT study [MZ11], the final state interactions (parton cascade and resonance decay...) can significantly reduce the magnitude of the observable, γ_{112}, from 10% to 1-2% in Au+Au collisions at 200 GeV. This result motivated another study [DHMW18], which illuminated the robust sensitivity of the proposed isobar collision program. Figure 6.7, taken from the paper, shows that, even with potential influence of final state interactions, the relative difference of the charge separation signal ($H_{\rm oppo} - H_{\rm same}$) In addition, the eccentricity-driven v_2 is very similar in these two systems, as shown in Fig. 6.8. We expect that the isobar collision data will provide valuable insight about the magnetic field induced charge separation effect. Observation of the effect from isobar data will be an experimental breakthrough in the search for the CME from heavy-ion collisions.

6.2.3 Event-shape Selection Analysis

Since the analyses mentioned above all show that the flow-related background is proportional to v_2, it would be an ideal scenario if flow-free ($v_2 = 0$) events could be accurately selected,

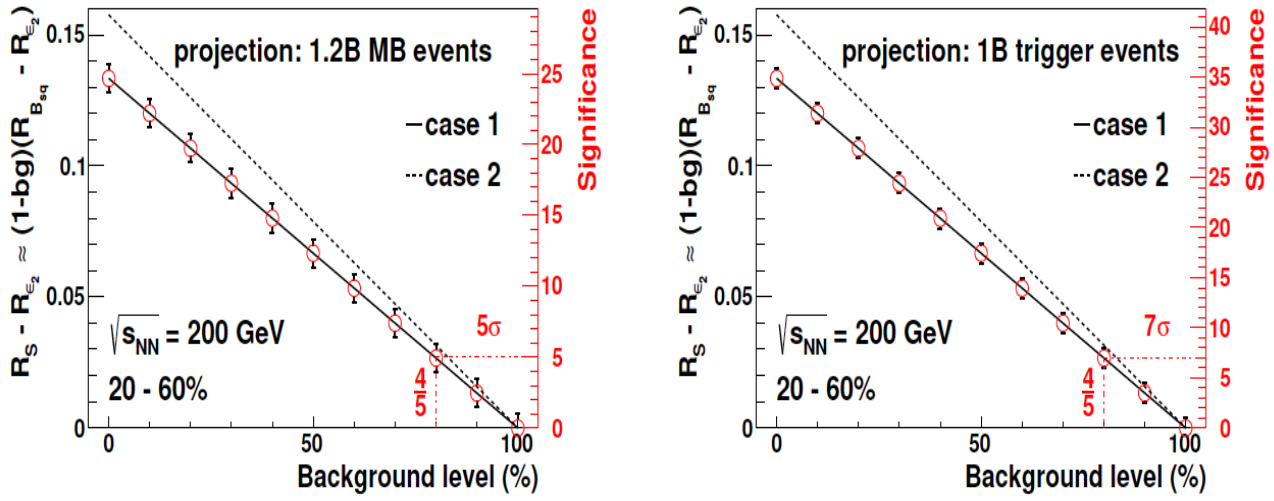

Figure 6.6: Magnitude and significance of the relative difference in the CME signal between Ru+Ru and Zr+Zr at 200 GeV, $R_S - R_{\epsilon_2}$, as a function of the background level. Results are estimated with TPC reconstructed event plane, based on 20-60% collisions selected from 1.2$\times$ 10^9 minimum bias events (left) or 10^9 specially triggered events (right). The case 1(2) refers to the set of parameters in the Woods-Saxon potential used in the calculations [DHMW18].

and a v_2 induced background-free γ_{112} correlation measurement became feasible.

6.2.3.1 Flow Vector q as the Handle

Recently, the ALICE collaboration reported a measurement [A$^+$18] on γ_{112} for Pb+Pb collisions at 2.76 TeV using an event-shape-engineering technique. In this study, the tracks separated by an η gap ($|\Delta\eta| > 0.9$) are used to select the event shape via the second-order reduced flow vector q (the q_2 in Ref. [A$^+$16a], for convenience, q is used to denote this quantity in the rest of the text) and do the measurements of v_2 and γ_{112} etc respectively. The q

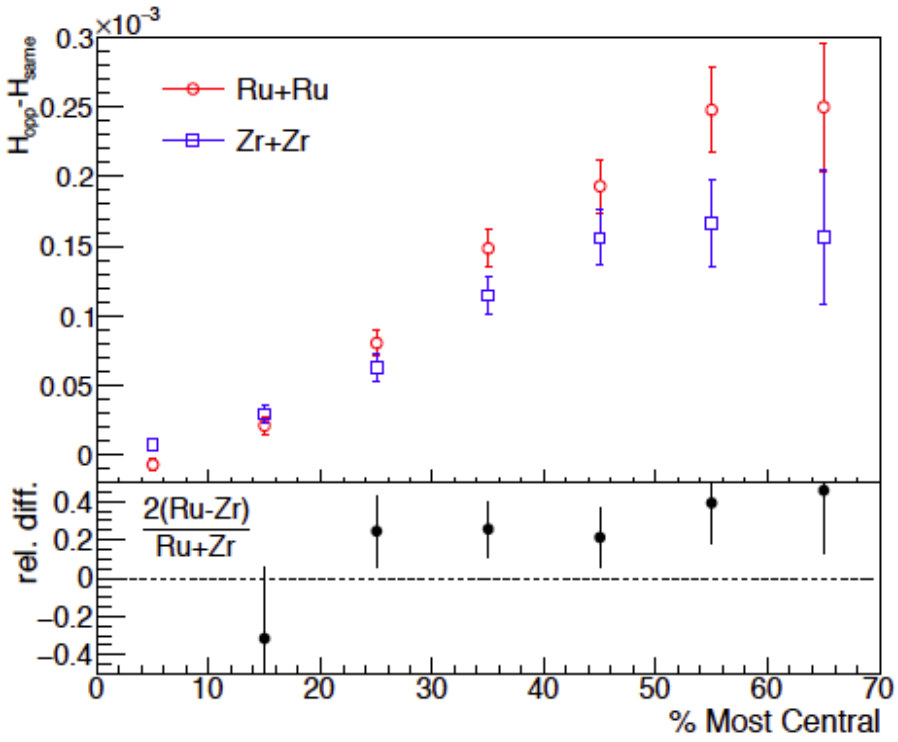

Figure 6.7: Upper: the centrality dependence of $H_{\rm opp} - H_{\rm same}$ (where $H_{\alpha\beta} = \gamma_{\alpha\beta}^{\rm CME} - \gamma_{\alpha\beta}^{\rm non\text{-}CME}$) for Ru+Ru and Zr+Zr collisions at $\sqrt{s_{NN}} = 200$ GeV. Lower: the corresponding relative difference.

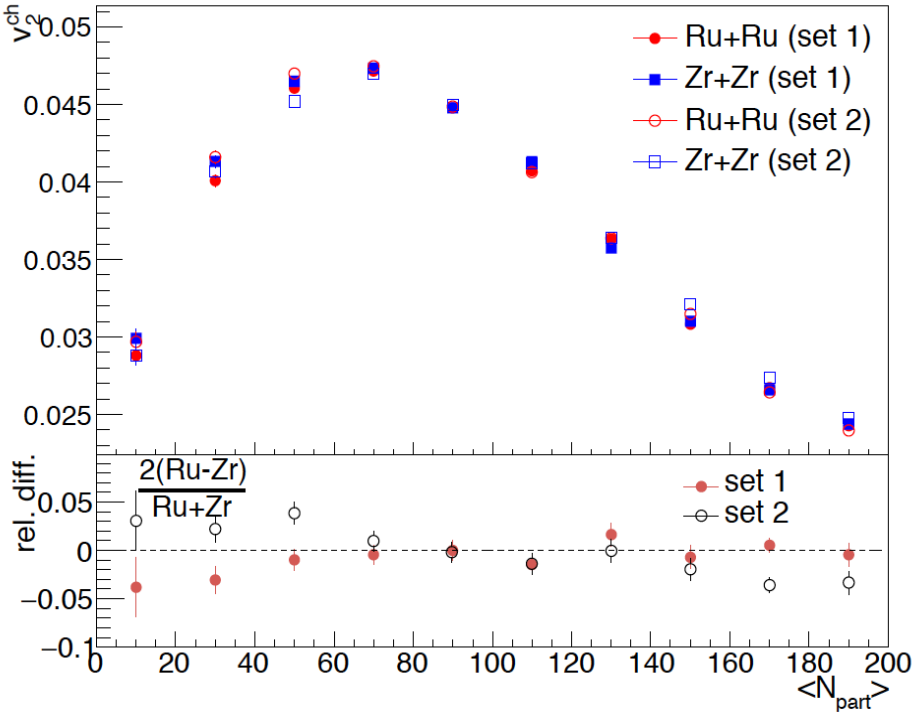

Figure 6.8: Upper: the N_{part} dependence of elliptic flow (v_2) of charged hadrons at mid-pseudorapidity ($|\eta| < 1$) from the string-melting model of AMPT, with two settings of isobar collisions at $\sqrt{s_{NN}} = 200$ GeV. Lower: the corresponding relative difference.

is defined as:

$$q = \frac{|\mathbf{Q_2}|}{\sqrt{M}} \tag{6.3}$$

$$|\mathbf{Q_2}| = \sqrt{Q_{2,x}^2 + Q_{2,y}^2} \tag{6.4}$$

$$Q_{2,x} = \sum_i^M \cos(2\phi_i),\ Q_{2,y} = \sum_i^M \sin(2\phi_i) \tag{6.5}$$

where ϕ_i is the azimuthal angle of the particle and M is the track multiplicity. For each centrality bin, events are divided into ten categories based on the q value (event shape). For each event shape category, the difference between $\gamma_{\alpha\beta}$ as a function of v_2 is shown in Fig. 6.9. In a pure background scenario, the linear trend in the bottom panel is supposed to cross the original point and the paper concludes the dominant component to the signal comes from non-CME effects. However, given the transient magnetic field in Pb+Pb collisions at such a high energy, this result does not necessarily veto the emergence of the CME in Au+Au collisions at RHIC energies, so it could be still interesting to apply a similar method in STAR data analysis.

6.2.3.2 Squared Flow Vector q^2 as the Handle

Another event shape handle has been proposed recently by this paper [WBWW18], with the key insight being to use q^2 of interested particle rather than q of other particles (see the definition in Eqs. 6.3). The advantage of this approach is it enables us to pick out events with apparent v_2 close to zero. When q^2 is small, there is an approximately linear relationship between q^2 and v_2. From Fig. 6.10, we can find the v_2^{observe}/R^B (reconstructed from a sub-event and corrected by the event plane resolution) successfully recovers the true elliptic flow (v_2^A) from the particles of interest, and the value indeed vanishes as q^2 goes to zero. As expected, a realistic AMPT simulation (without CME) shown in Fig. 6.11 indicates when q^2 vanishes, the background is consistent with zero. Therefore this technique could be used as a lever to obtain the CME induced charge separation signal in the flow-free scenario in real data analysis.

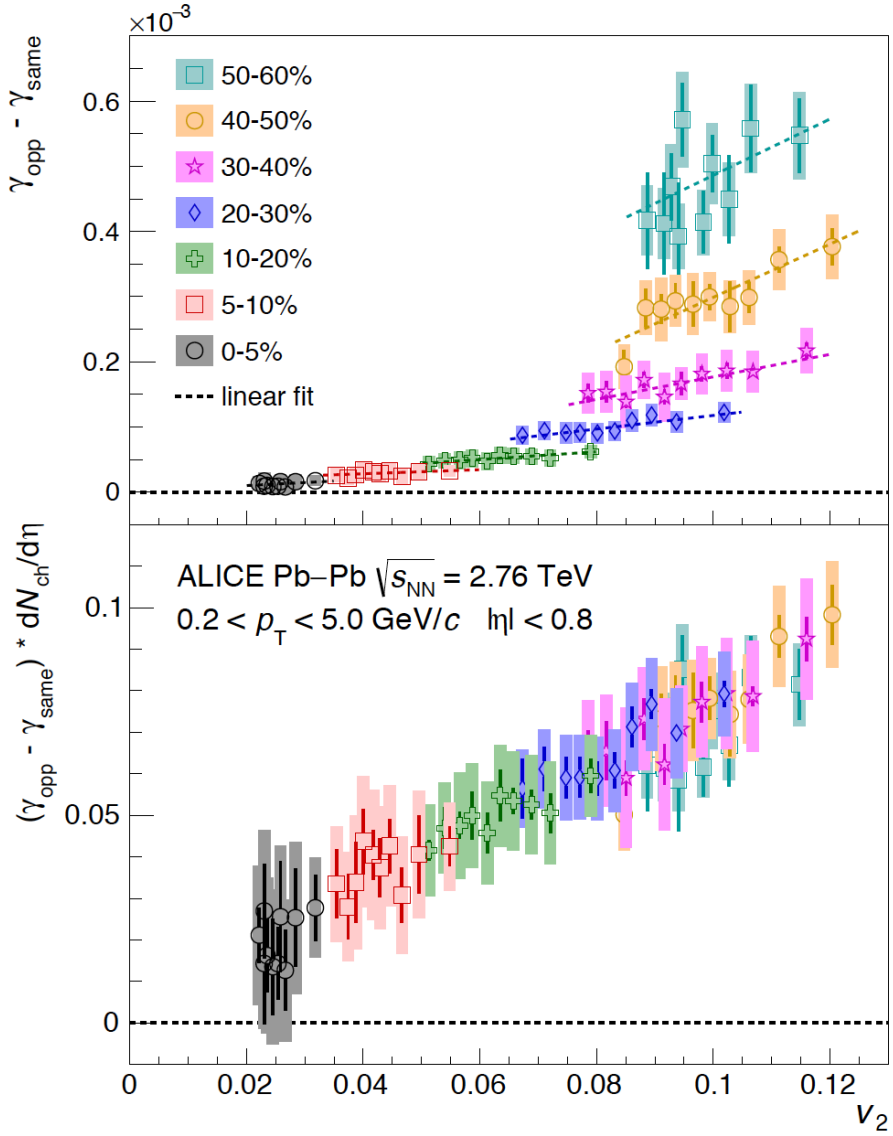

Figure 6.9: Top: Difference between opposite and same charge pair correlations for $\gamma_{\alpha\beta}$ as a function of v_2 for shape-selected events together with a linear fit (dashed lines) for various centrality classes. Bottom: Difference between opposite- and same-charge pair correlations for $\gamma_{\alpha\beta}$ multiplied by the charged-particle density as a function of v_2 for shape-selected events, together with a linear fit (dashed lines) for various centrality classes.

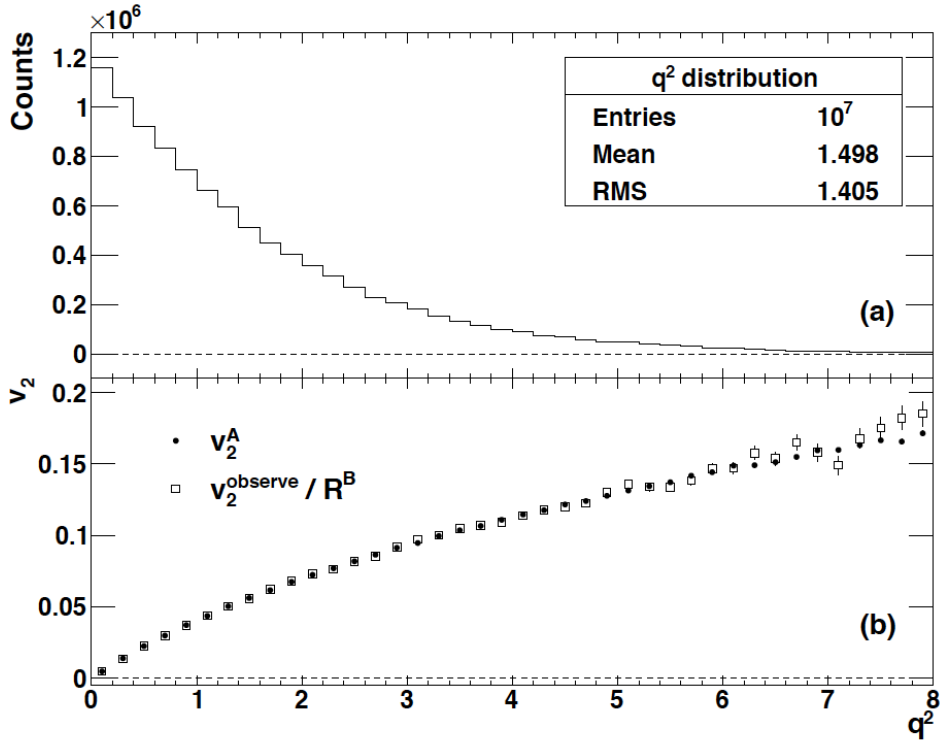

Figure 6.10: The distribution of q^2(a), and the true elliptic flow v_2^A and the corrected v_2^{observe} as functions of q^2 (b), from Monte-Carlo simulations

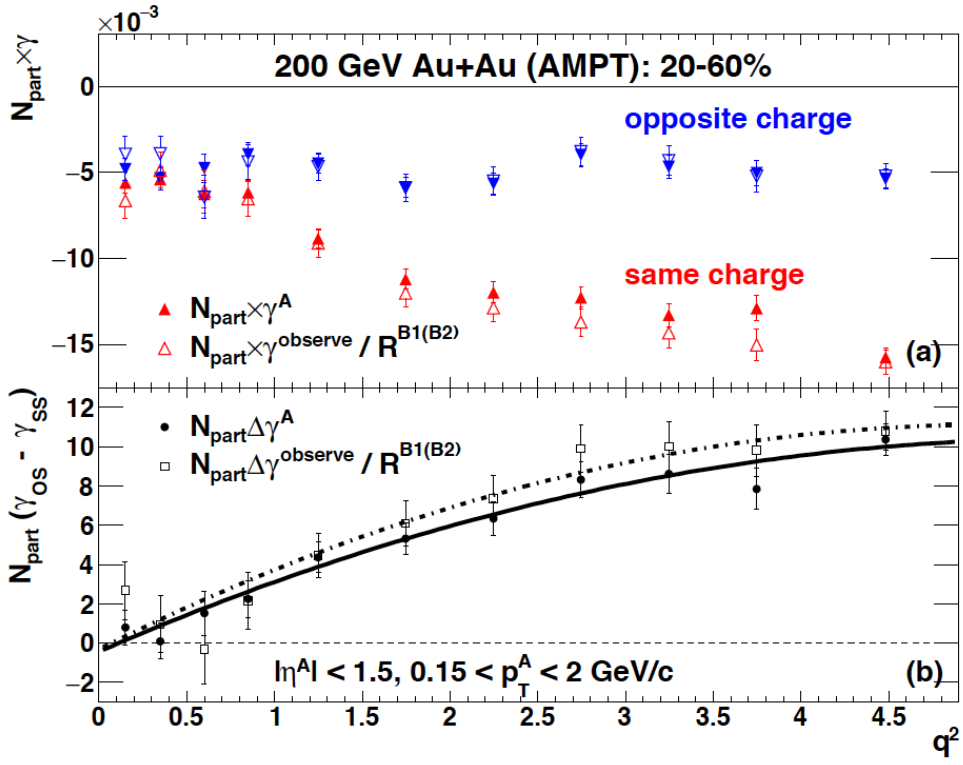

Figure 6.11: $N_{\rm part} \times \gamma$ (a) and $N_{\rm part}\Delta\gamma$ (b) as functions of q^2, from AMPT simulations. The full (open) symbols represent results obtained with the true reaction plane. The solid (dashed) line in the lower panel is a 2nd-order polynomial fit of the full (open) data points.

APPENDIX A

$\Omega^{-}(\bar{\Omega}^{+})$ and ϕ yield data

Table A.1: Ω^{-} spectra in Au+Au collisions at $\sqrt{s_{\rm NN}}$ =14.5 GeV $(0-10\%)$

p_T (GeV/c)	$\frac{d^2N}{2\pi p_T dp_T dy}$ $(\mathrm{GeV/c})^{-2}$	stat. err $(\mathrm{GeV/c})^{-2}$	sys. err $(\mathrm{GeV/c})^{-2}$
0.935611	0.0239488	0.00565275	2.18241e-03
1.37753	0.00747095	0.000828792	5.91284e-04
1.76893	0.00292456	0.000281681	2.10937e-04
2.16161	0.000783444	0.000102892	4.29182e-05
2.55479	0.000168013	4.16806e-05	1.16331e-05
3.0068	3.22137e-05	8.54276e-06	1.93861e-06

Table A.2: Ω^{-} spectra in Au+Au collisions at $\sqrt{s_{\rm NN}}$ =14.5 GeV $(10-60\%)$

p_T (GeV/c)	$\frac{d^2N}{2\pi p_T dp_T dy}$ $(\mathrm{GeV/c})^{-2}$	stat. err $(\mathrm{GeV/c})^{-2}$	sys. err $(\mathrm{GeV/c})^{-2}$
0.943727	0.00387391	0.000767111	3.01293e-04
1.3835	0.0013577	0.000119437	3.981103e-05
1.77422	0.000555251	3.84727e-05	1.09382e-05
2.16469	0.000179362	1.45455e-05	3.189961e-06
2.55341	5.2925e-05	5.95706e-06	1.009837e-06
2.97374	6.04494e-06	1.19997e-06	2.954128e-07

Table A.3: $\bar{\Omega}^{+}$ spectra in Au+Au collisions at $\sqrt{s_{\rm NN}}$ =14.5 GeV $(0-10\%)$

p_T (GeV/c)	$\frac{d^2N}{2\pi p_T dp_T dy}$	stat. err $(\mathrm{GeV/c})^{-2}$	sys. err $(\mathrm{GeV/c})^{-2}$
1.38649	0.00401611	0.000522312	2.18201e-04
1.77719	0.00184819	0.000178111	5.761112e-05
2.16681	0.000692122	7.60034e-05	2.87329e-05
2.55299	0.000225595	3.61618e-05	1.92914e-05
2.95302	2.19255e-05	9.21618e-06	2.12937e-06

Table A.4: $\bar{\Omega}^{+}$ spectra in Au+Au collisions at $\sqrt{s_{\rm NN}}$ =14.5 GeV $(10-60\%)$

p_T (GeV/c)	$\frac{d^2N}{2\pi p_T dp_T dy}(\mathrm{GeV/c})^{-2}$	stat. err $(\mathrm{GeV/c})^{-2}$	sys. err $(\mathrm{GeV/c})^{-2}$
1.3831	0.00104211	9.19077e-05	4.77213e-05
1.77317	0.000380215	3.13197e-05	1.12937e-05
2.1624	0.00011922	1.24169e-05	5.39168e-06
2.54877	3.7487e-05	5.92019e-06	2.01293e-06
2.95105	2.83288e-06	1.5689e-06	7.82711e-07

Table A.5: ϕ spectra in Au+Au collisions at $\sqrt{s_{\rm NN}}$ =14.5 GeV $(0-10\%)$

p_T (GeV/c)	$\frac{d^2N}{2\pi p_T dp_T dy}(\mathrm{GeV/c})^{-2}$	stat. err $(\mathrm{GeV/c})^{-2}$	sys. err $(\mathrm{GeV/c})^{-2}$
0.450854	0.396294	0.011939	1.4291e-02
0.550314	0.517564	0.00929488	1.88317e-02
0.649889	0.470199	0.00630797	1.31174e-02
0.749537	0.392584	0.00456589	9.013129-03
0.896434	0.32038	0.00232043	5.87091e-03
1.13707	0.20473	0.0012544	2.53112e-03
1.46857	0.0777991	0.000534093	1.34881e-03
1.82869	0.0221905	0.000204046	7.914501e-04
2.18529	0.00560135	5.9957e-05	6.42198e-05
2.74776	0.000712912	1.18908e-05	1.11294e-05

Table A.6: ϕ spectra in Au+Au collisions at $\sqrt{s_{\rm NN}}$ =14.5 GeV $(10-20\%)$

p_T (GeV/c)	$\frac{d^2N}{2\pi p_T dp_T dy}(GeV/c)^{-2}$	stat. err (GeV/c)$^{-2}$	sys. err (GeV/c)$^{-2}$
0.451059	0.358752	0.0114647	1.5291e-02
0.550551	0.339186	0.00700504	1.50315e-02
0.65015	0.318649	0.00492707	8.83321e-03
0.749813	0.26544	0.00353678	7.14209e-03
0.897552	0.221899	0.00184481	3.301139e-03
1.13917	0.138471	0.000968612	1.99289e-03
1.46954	0.0509642	0.000399938	7.59103e-04
1.82634	0.0178777	0.00017905	1.80902e-04
2.16697	0.00398258	4.69425e-05	2.76190e-05
2.64903	0.000406249	8.54884e-06	3.01772e-05

Table A.7: ϕ spectra in Au+Au collisions at $\sqrt{s_{\rm NN}}$ =14.5 GeV $(20-30\%)$

p_T (GeV/c)	$\frac{d^2N}{2\pi p_T dp_T dy}(GeV/c)^{-2}$	stat. err (GeV/c)$^{-2}$	sys. err (GeV/c)$^{-2}$
0.450833	0.248776	0.00920478	1.63221e-02
0.55029	0.273215	0.00650362	1.032338e-02
0.64986	0.21546	0.00395796	8.632311e-03
0.749505	0.190911	0.00298829	5.50213e-03
0.896287	0.143854	0.00143876	3.32101e-03
1.13668	0.0879438	0.000734096	1.62003e-03
1.46779	0.03095	0.000291645	3.80092e-04
1.82819	0.00928454	0.000117862	1.51299e-04
2.18393	0.00256777	3.61248e-05	3.00192e-05
2.74399	0.000197208	5.6764e-06	3.92432e-06

Table A.8: ϕ spectra in Au+Au collisions at $\sqrt{s_{\rm NN}}$ =14.5 GeV $(30-40\%)$

p_T (GeV/c)	$\frac{d^2N}{2\pi p_T dp_T dy}(GeV/c)^{-2}$	stat. err (GeV/c)$^{-2}$	sys. err (GeV/c)$^{-2}$
0.450757	0.167595	0.00789925	1.29231e-02
0.550198	0.151882	0.00448954	9.021658e-03
0.649754	0.156762	0.0035379	6.13132e-03
0.749385	0.12336	0.0024121	5.2192e-03
0.895737	0.0955182	0.00116087	2.0042e-03
1.13521	0.0483498	0.000510311	8.2108e-04
1.46488	0.0190957	0.00022205	2.91839e-04
1.82633	0.00390908	6.9449e-05	6.01887e-05
2.1789	0.00143396	2.65738e-05	2.8911e-05
2.73057	0.00012884	4.56443e-06	3.72998e-06

Table A.9: ϕ spectra in Au+Au collisions at $\sqrt{s_{\rm NN}}$ =14.5 GeV $(40-60\%)$

p_T (GeV/c)	$\frac{d^2N}{2\pi p_T dp_T dy}(GeV/c)^{-2}$	stat. err (GeV/c)$^{-2}$	sys. err (GeV/c)$^{-2}$
0.450907	0.0778903	0.00381796	5.0238e-03
0.55037	0.0708681	0.00225005	5.01219e-03
0.649942	0.0666546	0.00156588	3.5026e-03
0.749582	0.0521716	0.00107086	2.2133e-03
0.896517	0.0399226	0.000514483	1.30392e-03
1.13661	0.0203979	0.000223322	5.00123e-04
1.46519	0.00856184	0.00010688	2.21153e-04
1.82446	0.00223264	3.86889e-05	8.19213e-05
2.16644	0.000463287	1.03249e-05	1.90294e-05
2.66852	2.96253e-05	1.52136e-06	1.2912e-06
3.60365	2.13881e-06	2.87362e-07	1.01423e-07

Table A.10: ϕ spectra in Au+Au collisions at $\sqrt{s_{\rm NN}}$ =14.5 GeV $(60-80\%)$

p_T (GeV/c)	$\frac{d^2N}{2\pi p_T dp_T dy}(GeV/c)^{-2}$	stat. err (GeV/c)$^{-2}$	sys. err (GeV/c)$^{-2}$
0.45069	0.0166401	0.00133852	0.001532364
0.550115	0.0193178	0.000973366	0.00139285
0.649655	0.0168711	0.000631259	0.000928564
0.74927	0.0124086	0.000412218	0.000638747
0.895185	0.00836457	0.000181265	0.00017493
1.13365	0.00428563	8.08605e-05	7.3291e-05
1.46129	0.0014623	3.28678e-05	1.29312e-05
1.82373	0.000445347	1.50816e-05	9.129328e-06
2.17101	6.9919e-05	3.95663e-06	7.923e-07
2.70672	5.06991e-06	6.71445e-07	8.12933e-08

Table A.11: Ω^- Yield in Au+Au 14.5 GeV ($|y| < 0.5$)

Centrality	dN/dy	stat. err	sys. err
0%-10%	0.15489	0.0278029	0.018929
10%-60%	0.0230126	0.00262907	0.0014394

Table A.12: $\bar{\Omega}^+$ Yield in Au+Au 14.5 GeV ($|y| < 0.5$)

Centrality	dN/dy	stat. err	sys. err
0%-10%	0.0689246	0.00931242	0.0032432
10%-60%	0.0164474	0.0017532	0.0005323

Table A.13: ϕ Yield in Au+Au 14.5 GeV ($|y| < 0.5$)

Centrality	dN/dy	stat. err	sys. err
0%-10%	2.26461	0.0497894	0.30210
10%-20%	1.54579	0.0298971	0.2293
20%-30%	1.03115	0.023645	0.230203
30%-40%	0.650968	0.0141776	0.10029
40%-60%	0.277756	0.00625157	0.03823
60%-80%	0.0648477	0.00245158	0.0302939

REFERENCES

[A+03a] K. H. Ackermann et al. STAR detector overview. *Nucl. Instrum. Meth.*, A499:624–632, 2003.

[A+03b] J. Adams et al. Evidence from d + Au measurements for final state suppression of high p(T) hadrons in Au+Au collisions at RHIC. *Phys. Rev. Lett.*, 91:072304, 2003.

[A+03c] S. S. Adler et al. Absence of suppression in particle production at large transverse momentum in S(NN)**(1/2) = 200-GeV d + Au collisions. *Phys. Rev. Lett.*, 91:072303, 2003.

[A+03d] M. Anderson et al. *Nucl. Instrum. Meth.*, A499:659–678, 2003.

[A+05a] J. Adams et al. Azimuthal anisotropy in au+au collisions at $\sqrt{s_{NN}} = 200$ GeV. *Phys. Rev. C*, 72:014904, Jul 2005.

[A+05b] John Adams et al. Experimental and theoretical challenges in the search for the quark gluon plasma: The STAR Collaboration's critical assessment of the evidence from RHIC collisions. *Nucl. Phys.*, A757:102–183, 2005.

[A+07a] B. I. Abelev et al. Global polarization measurement in Au+Au collisions, 2007. [Erratum: Phys. Rev.C95,no.3,039906(2017)].

[A+07b] B. I. Abelev et al. Partonic flow and phi-meson production in Au + Au collisions at s(NN)**(1/2) = 200-GeV. *Phys. Rev. Lett.*, 99:112301, 2007.

[A+08] C. Alt et al. Energy dependence of phi meson production in central Pb+Pb collisions at s(NN)**(1/2) = 6 to 17 GeV. *Phys. Rev.*, C78:044907, 2008.

[A+09] B. I. Abelev et al. Measurements of phi meson production in relativistic heavy-ion collisions at RHIC. *Phys. Rev.*, C79:064903, 2009.

[A+14a] Betty Bezverkhny Abelev et al. Multi-strange baryon production at mid-rapidity in Pb-Pb collisions at $\sqrt{s_{NN}} = 2.76$ TeV. *Phys. Lett.*, B728:216–227, 2014. [Erratum: Phys. Lett.B734,409(2014)].

[A+14b] L. Adamczyk et al. *Phys. Rev. Lett.*, 113:052302, Jul 2014.

[A+15a] L. Adamczyk et al. Azimuthal anisotropy in U + U and Au + Au collisions at rhic. *Phys. Rev. Lett.*, 115:222301, Nov 2015.

[A+15b] Ani Aprahamian et al. Reaching for the horizon: The 2015 long range plan for nuclear science. 2015.

[A+16a] Jaroslav Adam et al. Event shape engineering for inclusive spectra and elliptic flow in Pb-Pb collisions at $\sqrt{s_{\rm NN}} = 2.76$ TeV. *Phys. Rev.*, C93(3):034916, 2016.

[A+16b] L. Adamczyk et al. Probing parton dynamics of QCD matter with Ω and ϕ production. *Phys. Rev.*, C93(2):021903, 2016.

[A+17a] L. Adamczyk et al. Bulk Properties of the Medium Produced in Relativistic Heavy-Ion Collisions from the Beam Energy Scan Program. *Phys. Rev.*, C96(4):044904, 2017.

[A+17b] L. Adamczyk et al. Bulk Properties of the Medium Produced in Relativistic Heavy-Ion Collisions from the Beam Energy Scan Program. *Phys. Rev.*, C96(4):044904, 2017.

[A+17c] L. Adamczyk et al. Global Λ hyperon polarization in nuclear collisions: evidence for the most vortical fluid. *Nature*, 548:62–65, 2017.

[A+18] Shreyasi Acharya et al. Constraining the magnitude of the Chiral Magnetic Effect with Event Shape Engineering in Pb-Pb collisions at $\sqrt{s_{\rm NN}} = 2.76$ TeV. *Phys. Lett.*, B777:151–162, 2018.

[ABMS06] A. Andronic, P. Braun-Munzinger, and J. Stachel. Hadron production in central nucleus-nucleus collisions at chemical freeze-out. *Nucl. Phys.*, A772:167–199, 2006.

[Ash16] Muhammad Usman Ashraf. Measurements of strange hadrons K(S)(0), and from Au+Au collisions at S(NN) = 14.5 GeV in STAR. *J. Phys. Conf. Ser.*, 668(1):012095, 2016.

[BCK+01] F. Becattini, J. Cleymans, A. Keranen, E Suhonen, and K. Redlich. Features of particle multiplicities and strangeness production in central heavy ion collisions between 1.7A-GeV/c and 158A-GeV/c. *Phys. Rev.*, C64:024901, 2001.

[BHZL13] John Bloczynski, Xu-Guang Huang, Xilin Zhang, and Jinfeng Liao. Azimuthally fluctuating magnetic field and its impacts on observables in heavy-ion collisions. *Phys. Lett.*, B718:1529–1535, 2013.

[BKL11] Adam Bzdak, Volker Koch, and Jinfeng Liao. Azimuthal correlations from transverse momentum conservation and possible local parity violation. *Phys. Rev. C*, 83:014905, Jan 2011.

[BKL13] A. Bzdak, V. Koch, and J. Liao. *Lecture Notes in Physics*, 871:529–532, 2013.

[BKL+17] F. Becattini, I. Karpenko, M. Lisa, I. Upsal, and S. Voloshin. Global hyperon polarization at local thermodynamic equilibrium with vorticity, magnetic field and feed-down. *Phys. Rev.*, C95(5):054902, 2017.

[BMG06] F. Becattini, J. Manninen, and M. Gazdzicki. Energy and system size dependence of chemical freeze-out in relativistic nuclear collisions. *Phys. Rev.*, C73:044905, 2006.

[BMR00] D. Bodeker, Guy D. Moore, and K. Rummukainen. Chern-Simons number diffusion and hard thermal loops on the lattice. *Phys. Rev.*, D61:056003, 2000.

[BSD+00] J. Brachmann, S. Soff, A. Dumitru, Horst Stoecker, J. A. Maruhn, W. Greiner, L. V. Bravina, and D. H. Rischke. Antiflow of nucleons at the softest point of the EoS. *Phys. Rev.*, C61:024909, 2000.

[C+09] M. Cheng et al. Baryon Number, Strangeness and Electric Charge Fluctuations in QCD at High Temperature. *Phys. Rev.*, D79:074505, 2009.

[CKM+18] Jinhui Chen, Declan Keane, Yu-Gang Ma, Aihong Tang, and Zhangbu Xu. Antinuclei in Heavy-Ion Collisions. *Phys. Rept.*, 760:1–39, 2018.

[Cle98] J. Cleymans. Strangeness: Theoretical status. In *Proceedings, 3rd International Conference on Physics and astrophysics of quark-gluon plasma (ICPA-QGP '97): Jaipur, India, March 17-21, 1997*, pages 55–64, 1998.

[CR99] L. P. Csernai and D. Rohrich. Third flow component as QGP signal. *Phys. Lett.*, B458:454, 1999.

[CT15] Sandeep Chatterjee and Prithwish Tribedy. Separation of flow from the chiral magnetic effect in u + u collisions using spectator asymmetry. *Phys. Rev. C*, 92:011902, Jul 2015.

[CZCH+96] E. Cerron Zeballos, I. Crotty, D. Hatzifotiadou, J. Lamas Valverde, S. Neupane, M. C. S. Williams, and A. Zichichi. A New type of resistive plate chamber: The Multigap RPC. *Nucl. Instrum. Meth.*, A374:132–136, 1996.

[DHMW16] Wei-Tian Deng, Xu-Guang Huang, Guo-Liang Ma, and Gang Wang. Test the chiral magnetic effect with isobaric collisions. *Phys. Rev.*, C94:041901, 2016.

[DHMW18] Wei-Tian Deng, Xu-Guang Huang, Guo-Liang Ma, and Gang Wang. Predictions for isobaric collisions at $\sqrt{s_{NN}} = 200$ GeV from a multiphase transport model. *Physical Review C*, 97(4), 4 2018.

[Dia03] Dmitri Diakonov. Instantons at work. *Prog. Part. Nucl. Phys.*, 51:173–222, 2003.

[FCL+01] L. E. Finch, A. Chikanian, R. S. Longacre, J. Sandweiss, and J. H. Thomas. Observing spontaneous strong parity violation in heavy-ion collisions. *Phys. Rev. C*, 65:014908, Dec 2001.

[FKW08] Kenji Fukushima, Dmitri E. Kharzeev, and Harmen J. Warringa. The Chiral Magnetic Effect. *Phys. Rev.*, D78:074033, 2008.

[HLO03] M. Harrison, T. Ludlam, and S. Ozaki. RHIC project overview. *Nucl. Instrum. Meth.*, A499:235–244, 2003.

[HS13] Ulrich Heinz and Raimond Snellings. Collective flow and viscosity in relativistic heavy-ion collisions. *Ann. Rev. Nucl. Part. Sci.*, 63:123–151, 2013.

[HY02] Rudolph C. Hwa and C. B. Yang. Inclusive distributions for hadronic collisions in the Valon recombination model. *Phys. Rev.*, C66:025205, 2002.

[HY07] Rudolph C. Hwa and C. B. Yang. Production of strange particles at intermediate pT in central Au+Au collisions at high energies. *Phys. Rev.*, C75:054904, 2007.

[Jia05] Hai Jiang. *Strange Hadron (KS, Lambda and Cascade) Production in d+Au Collisions at 200 GeV at RHIC*. PhD thesis, UCLA, 2005.

[K+17] Vardan Khachatryan et al. Observation of charge-dependent azimuthal correlations in p-Pb collisions and its implication for the search for the chiral magnetic effect. *Phys. Rev. Lett.*, 118(12):122301, 2017.

[Kha06] Dmitri Kharzeev. Parity violation in hot QCD: Why it can happen, and how to look for it. *Phys. Lett.*, B633:260–264, 2006.

[KLVW16] D. E. Kharzeev, J. Liao, S. A. Voloshin, and G. Wang. Chiral magnetic and vortical effects in high-energy nuclear collisionsA status report. *Prog. Part. Nucl. Phys.*, 88:1–28, 2016.

[KMW08] Dmitri E. Kharzeev, Larry D. McLerran, and Harmen J. Warringa. The Effects of topological charge change in heavy ion collisions: 'Event by event P and CP violation'. *Nucl. Phys.*, A803:227–253, 2008.

[KPT98] Dmitri Kharzeev, Robert D. Pisarski, and Michel H. G. Tytgat. Possibility of spontaneous parity violation in hot qcd. *Phys. Rev. Lett.*, 81:512–515, Jul 1998.

[LKL+05] Zi-Wei Lin, Che Ming Ko, Bao-An Li, Bin Zhang, and Subrata Pal. *Phys. Rev.*, C 72:064901, 2005.

[Llo12] W.J. Llope. Multigap rpcs in the star experiment at rhic. *Nuclear Instruments and Methods in Physics Research Section A: Accelerators, Spectrometers, Detectors and Associated Equipment*, 661:S110 – S113, 2012. X. Workshop on Resistive Plate Chambers and Related Detectors (RPC 2010).

[McL06] L McLerran. T.D. Lee: Relativistic Heavy Ion Collisions and the Riken Brookhaven Center. `https://www.bnl.gov/isd/documents/35336.pdf`, 2006.

[MHM98] Guy D. Moore, Chao-ran Hu, and Berndt Muller. Chern-Simons number diffusion with hard thermal loops. *Phys. Rev.*, D58:045001, 1998.

[MMX09] Hiroshi Masui, Bedangadas Mohanty, and Nu Xu. Predictions of elliptic flow and nuclear modification factor from 200 GeV U + U collisions at RHIC. *Phys. Lett.*, B679:440–444, 2009.

[MRSS07] Michael L. Miller, Klaus Reygers, Stephen J. Sanders, and Peter Steinberg. Glauber modeling in high energy nuclear collisions. *Ann. Rev. Nucl. Part. Sci.*, 57:205–243, 2007.

[MZ11] Guo-Liang Ma and Bin Zhang. Effects of final state interactions on charge separation in relativistic heavy ion collisions. *Physics Letters B*, 700(1):39 – 43, 2011.

[Nas13] Md. Nasim. *Azimuthal Anisotropy Measurements For Identified particles Produced In Au+Au Collisions At 7.7-200 GeV*. PhD thesis, National Institute of Science Education and Research, 2013.

[Oll92] Jean-Yves Ollitrault. Anisotropy as a signature of transverse collective flow. *Phys. Rev.*, D46:229–245, 1992.

[Pra10] Scott Pratt. Alternative Contributions to the Angular Correlations Observed at RHIC Associated with Parity Fluctuations. 2010.

[PSG11] Scott Pratt, Soeren Schlichting, and Sean Gavin. Effects of Momentum Conservation and Flow on Angular Correlations at RHIC. *Phys. Rev.*, C84:024909, 2011.

[PV98] A. M. Poskanzer and S. A. Voloshin. Methods for analyzing anisotropic flow in relativistic nuclear collisions. *Phys. Rev. C*, 58:1671–1678, Sep 1998.

[PY80] R. D. Pisarski and L. G. Yaffe. THE DENSITY OF INSTANTONS AT FINITE TEMPERATURE. *Phys. Lett.*, 97B:110–112, 1980.

[RR17] Paul Romatschke and Ulrike Romatschke. Relativistic Fluid Dynamics In and Out of Equilibrium – Ten Years of Progress in Theory and Numerical Simulations of Nuclear Collisions. 2017.

[RT02] K. Redlich and A. Tounsi. Strangeness enhancement and energy dependence in heavy ion collisions. *Eur. Phys. J.*, C24:589–594, 2002.

[Sho85] A. Shor. PHI MESON PRODUCTION AS A PROBE OF THE QUARK GLUON PLASMA. *Phys. Rev. Lett.*, 54:1122–1125, 1985.

[Sor99] H. Sorge. Highly sensitive centrality dependence of elliptic flow: A novel signature of the phase transition in QCD. *Phys. Rev. Lett.*, 82:2048–2051, 1999.

[SP11] Soren Schlichting and Scott Pratt. Charge conservation at energies available at the BNL Relativistic Heavy Ion Collider and contributions to local parity violation observables. *Phys. Rev.*, C83:014913, 2011.

[Sto05] Horst Stoecker. Collective flow signals the quark gluon plasma. *Nucl. Phys.*, A750:121–147, 2005.

[T+18] M. Tanabashi et al. Review of particle physics. *Phys. Rev. D*, 98:030001, Aug 2018.

[tH76a] Gerard 't Hooft. Computation of the Quantum Effects Due to a Four-Dimensional Pseudoparticle. *Phys. Rev.*, D14:3432–3450, 1976. [,70(1976)].

[tH76b] Gerard 't Hooft. Symmetry Breaking Through Bell-Jackiw Anomalies. *Phys. Rev. Lett.*, 37:8–11, 1976. [,226(1976)].

[Tuc13] Kirill Tuchin. Particle production in strong electromagnetic fields in relativistic heavy-ion collisions. *Adv. High Energy Phys.*, 2013:490495, 2013.

[vdS14] Wilke van der Schee. *Gravitational collisions and the quark-gluon plasma*. PhD thesis, Utrecht U., 2014.

[vHSX98] H. van Hecke, H. Sorge, and N. Xu. Evidence of early multistrange hadron freezeout in high-energy nuclear collisions. *Phys. Rev. Lett.*, 81:5764–5767, 1998.

[Vit85] Jeffrey S. Vitter. Random sampling with a reservoir. *ACM Trans. Math. Softw.*, 11(1):37–57, March 1985.

[Vol00] Sergei A. Voloshin. Discussing the possibility of observation of parity violation in heavy ion collisions. *Phys. Rev. C*, 62:044901, Aug 2000.

[Vol04a] Sergei A. Voloshin. *Phys. Rev. C*, 70:057901, Nov 2004.

[Vol04b] Sergei A. Voloshin. Parity violation in hot QCD: How to detect it. *Phys. Rev.*, C70:057901, 2004.

[Vol10] Sergei A. Voloshin. Testing the Chiral Magnetic Effect with Central U+U collisions. *Phys. Rev. Lett.*, 105:172301, 2010.

[WAH+57] C. S. Wu, E. Ambler, R. W. Hayward, D. D. Hoppes, and R. P. Hudson. Experimental Test of Parity Conservation in Beta Decay. *Phys. Rev.*, 105:1413–1414, 1957.

[Wan13] Gang Wang. Search for Chiral Magnetic Effects in High-Energy Nuclear Collisions. *Nucl. Phys.*, A904-905:248c–255c, 2013.

[WBWW18] Fufang Wen, Jacob Bryon, Liwen Wen, and Gang Wang. Event-shape-engineering study of charge separation in heavy-ion collisions. *Chin. Phys.*, C42(1):014001, 2018.

[YJLB] A.S. Yoon Y.-J. Lee and W. Busza. LHC Animation. `http://web.mit.edu/mithig/movies/LHCanmation.mov`.

[Zha14] Feng Zhao. *Strangeness Production and Strange V0 & Charged Hadron Correlation in Heavy-Ion Collisions*. PhD thesis, UCLA, 2014.